Potential Energy Curves and Associated Line Shape of Alkali-Metal and Noble-Gas Interactions

DISSERTATION

Larry Aaron Blank, Civ

AFIT-ENP-DS-14-D-51

DEPARTMENT OF THE AIR FORCE
AIR UNIVERSITY

AIR FORCE INSTITUTE OF TECHNOLOGY

Wright-Patterson Air Force Base, Ohio

AFIT-ENP-DS-14-D-51

POTENTIAL ENERGY CURVES AND ASSOCIATED LINE SHAPE OF ALKALI-METAL AND NOBLE-GAS INTERACTIONS

DISSERTATION

Presented to the Faculty

Graduate School of Engineering and Management

Air Force Institute of Technology

Air University

Air Education and Training Command

in Partial Fulfillment of the Requirements for the

Degree of Doctorate of Philosophy in Applied Physics

Larry Aaron Blank, B.S., M.S.

Civ

October 20, 2014

AFIT-ENP-DS-14-D-51

POTENTIAL ENERGY CURVES AND ASSOCIATED LINE SHAPE OF ALKALI-METAL AND NOBLE-GAS INTERACTIONS

Larry Aaron Blank, B.S., M.S.
Civ

Approved:

//signed//	September 12, 2014
Dr. David E. Weeks Chair	Date
//signed//	September 12, 2014
Dr. Glen P. Perram Member	Date
//signed//	September 12, 2014
Dr. Mark E. Oxley Member	Date
//signed//	September 12, 2014
Dr. Gary S. Kedziora Member	Date

Accepted:

//signed//	September 14, 2014
ADEDEJI B. BADIRU Dean, Graduate School of Engineering and Management	Date

AFIT-ENP-DS-14-D-51

Abstract

Recent interest in optically-pumped alkali laser systems has prompted this study into the binary interaction potentials between species of alkali-metal atoms and rare-gas atoms and the effects of the collision of these species on the alkali-metal atom absorption spectrum. Special attention is placed on the relationship of the interaction potentials and the resulting line shape. The $X^2\Sigma^+_{1/2}$, $A^2\Pi_{1/2}$, $A^2\Pi_{3/2}$, and $B^2\Sigma^+_{1/2}$ potential energy curves and associated dipole matrix elements are computed for $M+Ng$ at the spin-orbit multi-reference configuration interaction level, where M = K, Rb, Cs and Ng = He, Ne, Ar. Dissociation energies and equilibrium positions for all minima are identified and corresponding vibrational energy levels are computed. Difference potentials are used together with the quasistatic approximation to estimate the position of satellite peaks of collisionally broadened D_2 lines. The comparison of potential energy curves for different alkali-metal atom and noble-gas atom combinations is facilitated by using the same level of theory for all nine $M + Ng$ pairs. The Anderson-Talman theory of spectral line broadening is used together with potential energy curves calculated at the spin-orbit multi-reference configuration interaction level to compute broadening, shifting, and asymmetry coefficients of the D_1 and D_2 lines. The calculated coefficients are compared to experiment for a variety of temperatures. In all cases general agreement is observed for the broadening coefficients, while significant disagreement is observed for the shifting coefficients. I also compare my K + He broadening and shifting results with fully quantum mechanical calculations that employ the Baranger theory of collisional line broadening, and then compare the results with other semiclassical calculations. As with the comparison to experiment, closer agreement is observed for the broadening coefficients while the shifting

coefficients exhibit significant disagreement. I use the natural variation between the difference potentials of the nine $M + Ng$ pairs to explore the relationship between potential and line shape as determined by Anderson-Talman theory and develop a picture for the mechanism that underlies the general agreement between theoretical and experimental results on the broadening coefficient and the general disagreement on shifting coefficients.

Acknowledgements

I would like to thank, first and foremost, my mother and father, who have always provided unconditional love and endless support which made this work possible. I would also like to thank my adviser, David Weeks, who put up with me much longer than I ever though anyone possibly could. My thanks to Gary Kedzoria for his patience in guiding me through many quantum chemistry calculations, Glen Perram for always making sure my mind was on the big picture, and Mark Oxley for setting my sloppy physical mathematics straight. Lastly, I'd like to thank the entire Engineering Physics Department at AFIT for providing such a welcoming environment and many years of support.

Larry Aaron Blank

Table of Contents

Page

Abstract iv

Acknowledgements vi

List of Figures ix

List of Tables xii

I. Introduction 1

1.1 Motivation 1
1.2 Background 5

II. Potential Energy Surfaces 11

2.1 The Electronic Problem 13
2.1.1 The Born-Oppenheimer Approximation 14
2.1.2 The Symmetrization Postulate 17
2.1.3 Orbitals 18
2.1.4 Hartree Products 20
2.1.5 Slater Determinants 21
2.1.6 Operators and Matrix Elements 24
2.2 Hartree-Fock 28
2.2.1 The Hartree-Fock Equations 28
2.2.2 The Hartree-Fock Approximation 30
2.2.3 Basis Sets and the Roothaan Equations 33
2.2.4 The Self Consistent Field Procedure 38
2.3 Configuration Interaction 40
2.3.1 Excited Determinants 40
2.3.2 Multiconfigurational Wave Functions 42
2.3.3 Correlation Eneregy 43
2.3.4 Configuration Interaction 43
2.3.5 Singles and Doubles CI 46
2.4 Multi-configurational Self-Consistent Field 48
2.4.1 The MCSCF Procedure 49
2.4.2 Multireference Configuration Interaction Singles and Doubles 50

III. M+Ng Potential Energy Curves 54

3.1 MCSCF PECs 54
3.1.1 Description of the MCSCF calculations 54

Page

3.1.2 Comparison of MCSCF vs. SOCI curve for Li + He . . . 56
3.1.3 Results of PEC calculations . . . 58
3.1.4 The evolution of the line broadening picture as a result of the ab initio calculations . . . 64
3.2 Multireference Configuration Interaction Singles and Doubles Potential Energy Curves . . . 65
3.2.1 Computational Approach . . . 65
3.2.2 Results and Discussion . . . 68

IV. Collisional broadening . . . 89

4.1 The General Anderson-Talman Theory . . . 90
4.1.1 Impact Approximation . . . 96
4.1.2 Quasi-Static Approximation . . . 97
4.2 Computational model of AT theory . . . 98
4.2.1 Case I: $b \geq r_s$ . . . 101
4.2.2 Case II: $b < r_s$ . . . 106
4.2.3 Conclusions of the computational model . . . 118

V. Results of the Anderson-Talman Model Calculations . . . 120

5.1 Theory . . . 120
5.2 Difference Potentials . . . 125
5.3 Computational Details . . . 128
5.4 Results . . . 136
5.5 Comparison with other work . . . 147

VI. Conclusions . . . 153

Bibliography . . . 157

List of Figures

Figure		Page
1.	The reference states used in calculating the $M + Ng$ potential energy curves.	51
2.	A Lennard-Jones difference potential derived from broadening and shifting measurements of Rb + He.	55
3.	Li + He MCSCF vs MRSDCI	57
4.	MCSCF excited surfaces of Li + Ng	59
5.	MCSCF excited surfaces of Na + Ng	59
6.	MCSCF excited surfaces of K + Ng	60
7.	MCSCF excited surfaces of Rb + Ng	60
8.	MCSCF excited surfaces of Cs + Ng	61
9.	MCSCF ground surfaces of Li + Ng	61
10.	MCSCF ground surfaces of Na + Ng	62
11.	MCSCF ground surfaces of K + Ng	62
12.	MCSCF ground surfaces of Rb + Ng	63
13.	MCSCF ground surfaces of Cs + Ng	63
14.	Asymptotic limit of Li + He for its excited states	64
15.	Rb + Ne MRSDCI ground and excited curves	68
16.	Features of the Rb+Ne excited state curves	70
17.	All $M + Ng$ $X^2\Sigma^+_{1/2}$ curves	71
18.	All $M + Ng$ $B^2\Sigma^+_{1/2}$ curves	72
19.	All $M + Ng$ $A^2\Pi_{1/2}$ curves	73
20.	All $M + Ng$ $A^2\Pi_{3/2}$ curves	74
21.	Cs + Ar $B^2\Sigma^+_{1/2}$ Well	78

Figure Page

22. Rb + He ab initio vs Morse fit to exp 81

23. Cs + Ar Potential Energy Curves, Difference Potentials, and Dipoles 85

24. Rb + He experimentally derived Lenard Jones potential 100

25. Possible cases of perturber trajectories 101

26. The symmetric trajectory 103

27. Example of a long range to long range trajectory 110

28. Example of an outside to long range trajectory 113

29. Example of a long range to out trajectory 114

30. The $\Delta V_{\Pi_{1/2}}$ difference potentials for all $M + Ng$ combinations. 126

31. The $\Delta V_{\Pi_{3/2}}$ difference potentials for all $M + Ng$ combinations. 127

32. The $\Delta V_{\Sigma_{1/2}}$ difference potentials for all $M + Ng$ combinations. 127

33. The Cs + He $\Delta V_{\Sigma_{1/2}}$ difference potential, associated broadening and shifting integrands, and phase 130

34. Broadening and shifting integrands and effective hard sphere 131

35. Oscillation over the window of interruption as a function of temperature 134

36. The effect of averaging over the Maxwell speed distribution verses using mean speed 135

37. Predicted broadening (half-width) coefficients for the D1 line of all $M + Ng$ combinations. 136

38. Predicted broadening (half-width) coefficients for the D2 line of all $M + Ng$ combinations. 137

Figure Page

39. The Cs + He $\Delta V_{\Pi_{1/2}}$, $\Delta V_{\Pi_{3/2}}$, and $\Delta V_{\Sigma_{1/2}}$ broadening coefficients and the difference potentials which generated them 138

40. The drift inwards of b_0 as temperature increases 139

41. Predicted shifting coefficients for the D1 line of all $M + Ng$ combinations. 141

42. Predicted shifting coefficients for the D2 line of all $M + Ng$ combinations. 141

43. The Cs + He $\Delta V_{\Pi_{1/2}}$, $\Delta V_{\Pi_{3/2}}$, and $\Delta V_{\Sigma_{1/2}}$ shifting coefficients and the difference potentials which generated them 143

44. The sensitivity of the shift to the long range form of the difference potential 145

45. Predicted asymmetry coefficients for the D1 line of all $M + Ng$ combinations. 146

46. Predicted asymmetry coefficients for the D2 line of all $M + Ng$ combinations. 146

47. A comparison of broadening coefficients computed using the semiclassical AT theory with other theoretical calculations 151

48. A comparison of Shifting coefficients computed using the semiclassical AT theory with other theoretical calculations 152

List of Tables

Table		Page
1.	Notations for one- and two-electron integrals over spin orbitals (χ) and spatial orbitals (ψ)	25
2.	Matrix elements between determinants for one-electron operators	27
3.	Matrix elements between determinants for two-electron operators	28
4.	$A^2\Pi$ Well for Li + He	57
5.	Rb + He active space configurations	67
6.	Equilibrium and barrier positions for $M + Ng$ PECs	75
7.	Well depths and barrier heights for $M + Ng$ PECs	76
8.	Rb + He $A^2\Pi_{3/2}$ vibrational energy level differences	80
9.	K + Ar $X^2\Sigma^+$ and $A^2\Pi$ vibrational energy level differences	82
10.	Cs + He $A^2\Pi_{1/2}$ and $A^2\Pi_{3/2}$ vibrational energy levels	83
11.	D2 satellite positions	88
12.	Broadening and shifting coefficients fit to a power law in temperature	142
13.	Comparison of broadening and shifting coefficients computed using semiclassical AT theory to experiment and other theory	149
14.	A comparison of Cs + Ng asymmetry coefficients computed using semiclassical AT theory with experiment	150

POTENTIAL ENERGY CURVES AND ASSOCIATED LINE SHAPE OF ALKALI-METAL AND NOBLE-GAS INTERACTIONS

I. Introduction

1.1 Motivation

High energy laser (HEL) systems have been the subject of much research and development in past decades. After all this time, the idea of integrating HEL into weapons systems is quickly becoming a reality. As such, all branches of the United States military are involved in efforts to produce HEL weapons systems. Such systems face a variety of challenges. A brief summary of these challenges includes: defining the parameters which must be met for a particular engagement scenario, the HEL device itself (the device which will actually produce the high energy laser), a system to direct and control the beam, understanding and correcting for atmospheric effects on the beam during propagation, and determining the requirements for target lethality. Although each of these challenges involve a broad range of physical considerations and technological implementations, only the HEL devices themselves will be considered in this work.

There are several broad categories of HEL devices currently being researched by funding provided by the Department of Defense including chemical, free electron, and solid-state lasers. All lasers require some mechanism to create a population inversion. Chemical lasers produce this inversion through chemical interactions that yield products in an excited state. These products then release their energy through the process of stimulated and spontaneous emission, dropping them down into a lower

energy state. If the chemical reaction is quick enough compared to the stimulated emission, and the spontaneous emission slow enough compared to stimulated emission, then the population inversion is maintained and lasing results. Chemical laser devices are capable of generating very powerful lasers and have been integrated into several weapons systems in development by the Department of Defense. Thermal management issues are easily handled by exhausting the hot gases. On the down side chemical lasers are big and they require specialized fuels and have pollutants, etc.

Free electron lasers use a relativistic electron beam as their lasing medium. Electrons are accelerated through a vacuum to near the speed of light. Coherent laser radiation is converted from the kinetic energy of the electrons by sending them through a series of magnets. These magnets cause the electrons to wiggle during their motion, producing electromagnetic radiation. The wavelength of the coherent radiation is easily and rapidly adjusted over a wide range by tuning the magnets or adjusting the kinetic energy of the electron beam. The disadvantages of this approach involve size, weight, and cost. These disadvantages get more pronounced as one attempts to make a high energy laser of shorter and shorter wavelengths.

Solid-state lasers (SSL) include heat-capacity, fibers, and continuously-cooled lasers. In the past, flash-lamp lasers have provided kilo-Watt peak power with good beam quality. More recently, high efficiency, laser diode arrays have enabled the possibility of higher average power SSL weapons. These systems offer several advantages over the previously mentioned systems. They are smaller and less costly than chemical and free electron lasers. Also, they do not require specialized fuels for input energy like chemical lasers. The primary disadvantage of these systems is that they are solid. This means that thermal management cannot be handled by simply exhausting hot gas. Complex cooling mechanisms must be designed and implemented. Even with these considerations temperature gradients will exist throughout the solid.

This complicates optical processes among other things. As a consequence, thermal management is the great challenge in implementing a SSL weapon.

In 2003 Krupke et al. [2003] proposed an entirely new type of laser. This laser combines properties of both gas phase and solid state lasers. The idea is as follows: a sample of an alkali-metal atom is placed in an optically transparent container and heated to a point where an appreciable amount of the alkali-metal atoms are in the gas phase. A buffer gas composed of noble-gas atoms (and possibly methane) is then pumped into the container. An optical pump source is arranged so it shines on the alkali-metal atoms, pumping the D_2 transition ($^2S_{1/2} \rightarrow \ ^2P_{3/2}$). This is followed by rapid collisions with the buffer gas which induces a transition to the alkali-metal atom's $^2P_{1/2}$ state ($^2P_{3/2} \rightarrow \ ^2P_{1/2}$). Lasing occurs via stimulated emission on the D_1 line ($^2P_{1/2} \rightarrow \ ^2S_{1/2}$). The presence of the buffer gas also serves to broaden the absorption features of the alkali-metal atoms, which are relatively narrow compared to the emission spectrum of the diodes. This broadening will have the effect of making the device more efficient. In this text I will use the term OPAL for this type of device, standing for *Optically Pumped Alkali Laser*. In the decade since the OPAL was proposed there have been many studies of these systems. For example, see Beach et al. [2004], Zhdanov et al. [2006], Page et al. [2006], Zhdanov et al. [2008].

During operation of an OPAL an optical source will drive the $^2S_{1/2} \rightarrow ^2 P_{3/2}$ atomic transition. In the case of the K + Ng and Rb + Ng, the alkali-metal atoms have a small enough spin-orbit splitting of the ^2P alkali-metal state so that the noble-gas atoms in the buffer gas will be sufficient to drive the spin-orbit relaxation. In the case of Cs + Ng, CH_4 or a similar additive must be inserted into the buffer gas. This increases the rate of the collisional deexcitation due to the many internal degrees of freedom in the methane, providing more mechanisms by which the spin-orbit energy may be transferred from the alkali-metal atoms. The pump rate and the spin-orbit

relaxation rate must be fast compared to the spontaneous emission rates for both the $^2P_{1/2}$ and $^2P_{3/2}$ states in order to maintain a population inversion between the $^2P_{1/2}$ and $^2S_{1/2}$ states.

OPAL lasers offer much promise, potentially marrying the advantages of a SSL with the ease of thermal management the gas phase provides. Although these advantages are enticing, OPAL systems have their own challenges which need to be addressed. The advantage of using a solid as the lasing medium is that its absorption features are broad. This fits well with the diodes, which have a broad emission spectrum. On the other hand, the absorption profile of the alkali-metal atom's D_2 transition used in an OPAL is relatively narrow. This results in a lack of efficiency since much of the diode radiation is not absorbed. Currently a great deal of research effort is being made both to narrow the spectral emission of the diodes, while simultaneously broadening the absorption features of the alkali-metal atom. While most success thus far has been in the narrowing of the diodes, it is still ideal to meet in the middle of these two approaches to maximize the efficiency of the OPAL.

In this work the emphasis will be on the spectral broadening of the alkali-metal atom's absorption features. Although the width of a spectral absorption feature is dependent on many different physical processes (see Chapter IV), the primary contributor to the broadening is accomplished via collisions that the alkali-metal atom has with the buffer gas. This kind of broadening is appropriately named *collisional broadening*.

Several theoretical models for collisional broadening exist and are reviewed by Szudy and Baylis [1996] and Allard and Kielkopf [1982]. To become predictive these models require knowledge of the interaction potentials between collision partners. A complete description of the forces of interaction between atoms and molecules is contained in a *potential energy curve* (PEC) (see Chapter II), the generation of

which is a major goal of computational chemistry. PECs are often calculated from a variety of quantum mechanical methods which have been developed over the years. Of these methods, *ab initio* calculations have delivered good results. *Ab initio* literally means *from the beginning*. These methods calculate potential energy surfaces from first principles, while applying a variety of approximations in the process. While computational resources required for these calculations scales rapidly with system size, ab initio potential energy surfaces calculated for systems that are small enough to be amenable to these calculations can lead to very accurate physical predictions.

As a first step in developing a theoretical understanding of the collisional line broadening processes that occur in OPAL systems, I computed the $X^2\Sigma^+_{1/2}$, $A^2\Pi_{1/2}$, $A^2\Pi_{3/2}$, and $B^2\Sigma^+_{1/2}$ potential energy curves (PECs) and corresponding dipole transition moments for $M + Ng$ combinations, where M = K, Rb, Cs and Ng = He, Ne, Ar. The same level of theory is used to compute PECs for all nine $M + Ng$ pairs facilitating the identification of trends across the molecular systems. I then used these PECs with a semi-classical model of collisional broadening to predict the broadening and shifting coefficients for the different systems over a range of $T = 50 - 3000K$. The $M + Ng$ systems also exhibit blue satellites off of the D_2 line core. I used the collisional broadening model and the PECs to predict the position of the satellites.

1.2 Background

The first OPAL system was reported in Beach et al. [2004]. This work produced a host of experimental and model results which provided evidence that the physics involved in the OPAL concept was well understood. It also demonstrated that potassium, rubidium, and cesium make good candidates for a OPAL (rubidium was used by Krupke et al. [2003] in generating the concept of a OPAL). It is the magnitude of the fine structure splitting between the $^2P_{1/2}$ and $^2P_{3/2}$ levels which determines the

effectiveness of a particular alkali-metal atom for use in a OPAL. If the splitting is small then the fine structure transition rate will be fast. This means that population will quickly transfer from the pumped $^2P_{3/2}$ level to the lasing $^2P_{1/2}$ level, establishing a population inversion. However, a small fine structure transition rate also makes it difficult to specifically pump the $^2P_{3/2}$ level without simultaneously pumping the $^2P_{1/2}$ level as well due to the broad emission spectrum of the pumping diodes. The fast fine structure transition rate can also be a double edged sword as it can cause population to transfer from the $^2P_{1/2}$ to the $^2P_{3/2}$, which is opposite the preferred transition. When the fine structure splitting between the $^2P_{1/2}$ and $^2P_{3/2}$ levels is large then the broad emission spectrum of the diodes is not a complicating factor and pumping the $^2P_{3/2}$ level specifically is possible. The large fine structure splitting also reduces the chance of collisions depleting the population inversion by causing a $^2P_{1/2}$ to $^2P_{3/2}$ transition. However, the fine structure transition rate from the $^2P_{3/2}$ level to the $^2P_{1/2}$ level will also be slow. It is in this case which an additive such as CH_4 must be used to increase the fine structure transition rate to the point where lasing becomes possible.

Not only is an understanding of alkali-metal noble-gas systems of interest to people researching OPALs, but these systems provide an excellent example of van der Walls complexes. Although well depths in the ground state of an alkali-metal atom plus a noble-gas atom PEC rarely exceed tens of wave numbers (cm^{-1}), the wells in the first, spin-free, excited state $A^2\Pi$ are deep enough to provide van der Walls binding. A molecule which binds only in an excited state of the system is called an *exciplex*. Due to these properties, a host of experimental and theoretical studies have been made for alkali-metal noble-gas systems. A collection of the work done on this subject up to 1981 may be found in Rostas [1981]. Most of these studies focused on scattering, absorption spectroscopy of the three lowest states ($X^2\Sigma$, $A^2\Pi$ and $B^2\Sigma$), emission

spectroscopy using laser induced florescence or electric discharge. More recently, high resolution laser spectroscopy has provided a new approach to experimentally probing these systems. Pitz et al. [2009] and Pitz et al. [2010] recently used this method to probe the broadening and shift of cesium with a variety of collisional partners including all rare gases. This data was used to produce experimentally derived difference potentials for the transitions between the states involved. A similar study was conducted for rubidium by Rotondaro and Perram [1997]. The rotationally resolved absorption spectrum for the $A^2\Pi \rightarrow B^2\Sigma$ transition of Li + Ne has been measured by Lee and Havey [1991]. All rovibrational levels of the $X^2\Sigma$ states of Li + Ar and of Na + Kr have been observed by Bruhl and Zimmermann [2001] and Bruhl et al. [1991], who has provided values of the spectroscopic constants for their rotation and vibration. The recent observation of brown dwarfs has also revived interest in the spectral broadening of various alkali-metal atoms [Seager and Sasselov, 2000, Burgasser et al., 2003, Zhu et al., 2006, Allard et al., 2007, Santra and Kirby, 2005]. The line shape of light alkali-metal atoms in the brown dwarf photosphere provides a useful diagnostic of the opacity of the atmospheres of these substellar objects [Allard et al., 2007].

Theoretical developments of collisional broadening began as far back as 1895 with Michelson in Michelson [1885]. Since then a wealth of progress has been accumulated. Early but still often cited reviews of the subject include Ch'en and Takeo [1957] and Breene [1957]. Developments up until the early 1980's have been reviewed by Allard and Kielkopf [1982] and Hindmarsh and Farr [1972]. The fundamentals of a quantum treatment of pressure broadening have been reviewed by Szudy and Baylis [1975]. Here the authors lay out basic principles, which are the starting point for all modern developments of a quantum picture of pressure broadening, and show how this theory reduces to the classical theory under certain approximations. More

advanced treatments which capture the physical effects dominant in the wings of the spectrum as well as satellites has also been reviewed by Szudy and Baylis [1996].

Accurate *ab initio* calculations of excited state curves in alkali-metal atom interactions with noble-gas atoms have not been possible until relatively recently, within the last 20 years. Many of these calculations have focused on Li + He due to this being the simplest (in terms of number of electrons in the system) of the alkali-metal atom and noble-gas atom combinations. In Behmenburg et al. [1996] the authors evaluate Li + He using *CEPA-2 CI*, which consists of a series of different ab initio methods, including self-consistent field and couple-cluster methods, to arrive at a final result. Behmenburg et al. [1996] also apply this method to Li + Ne. *Ab initio* surfaces for Li + Ar and Li + Kr in the states $X^2\Sigma$, $A^2\Pi$ and $B^2\Sigma$ have been generated using couple cluster methods by Ioannis et al. [2002]. The authors use these surfaces to predict rovibrational spectroscopic constants and dissociation energies for any states which show appreciable wells.

Potential surfaces of the $X^2\Sigma$, $A^2\Pi$ and $B^2\Sigma$ states and spectroscopic constants for these excited states have been obtained by pseudopotential methods for the molecules Li + Ar, Na + Ar and K + Ar by Rhouma et al. [2002]. A potential surface for Na + He has been generated by Theodorakopoulos and Petsalakis [1993] using a multi-reference singles and doubles configuration interaction calculation. The K + He interaction potential has been explored by Santra and Kirby [2005] using a multi-reference configuration interaction calculation. A comprehensive collection of ground state surfaces for all pairs of alkali-metal atoms Li through Cs with noble-gas atoms Ne through Xe were computed by Goll et al. [2006]. Although the authors do not report these surfaces in the literature, they do report on dissociation energies, bond lengths and harmonic frequencies for the van der Walls interaction of all these alkali-metal atom and noble-gas atom combinations in the ground state. The authors

combine the use of the couple-cluster *ab initio* technique for the short-internuclear separation part of the potential surface with the use of density functional theory for the long-internuclear separation component. Recently, Allard et al. [2007] used *ab initio* potential energy curves, calculated with pseudopotential methods for M + He [Pascale, 1983] and M + H_2 [Rossi and Pascale, 1985], together with a dipole autocorrelation formulation of spectral broadening theory, to determine collisional broadening coefficients for M = Li, Na, and K over a temperature range of $500 - 3000K$. These calculations employ a classical path approximation and include a dipole transition moment that is functionally dependent on the internuclear separation of the emitter and perturber [Allard et al., 1999]. The dipole autocorrelation formulation has also been used to compute line profiles of Rb + He and Cs + He [Allard and Speigelman, 2006]. Mullamphy et al. [2007] have calculated potentials for Li + He, Na + He and K + He using a three body model in which the alkali-metal atom is treated as an ion with a polarizable core and an active electron. The third body is the perturbing He atom. Collisional broadening analysis of these surfaces is done using the quantum impact theory of Baranger [1958]. Zhu et al. [2006] and Zhu et al. [2005] describe carefully constructed surfaces for these same combinations, using different references for different internuclear separations in putting together these surfaces, and then use these surfaces to make quantum calculations of the emission spectrum and absorption spectrum for different transitions.

The remainder of this document is organized as follows. Chapter 2 explores background quantum chemistry theory relevant to the *ab intio* calculations presented later in this document. This chapter may be skipped if the reader is interested only in the results of my work. The *ab initio* calculations for M + Ng molecular combinations are reported and discussed in Chapter 3. Chapter 4 discusses both pedagogical background information on the Anderson-Talman theory of collisionally induced line

shapes, as well as a discussion of the algorithm used to computationally implement the model. The results and a detailed analysis of the calculations performed using the Anderson-Talman model is presented in Chapter 5. Finally, Chapter 6 is a discussion of the conclusions I have drawn from my work, as well as a section on how this work my be extended and improved.

II. Potential Energy Surfaces

In the subject of mechanics few ideas carry as much importance as that of potential energy. Under Newton's equations for a system of particles all particle trajectories can be deduced exactly, in principle, if one has a knowledge of the initial conditions and the details of the forces of interaction between said particles. For conservative systems the details of these forces may be expressed in terms of the potential energy one particle feels as a result of the other particles. Furthermore, in Quantum Mechanics all non-relativistic details of the state of the system can be calculated from the Schrödinger equation. This solution, as the solution to Newton's equations, requires a knowledge of initial conditions and the potential energy of the system. The purpose of this chapter is to outline the methods I used to calculate the interaction potential, i.e., forces of interaction, between nuclei during atomic and molecular collisions, specifically the interaction between an alkali-metal atom and a noble-gas atom. This provides us with the ability to predict the nuclear motion.

This chapter begins with a discussion of the mathematics required for the subject. An idea central to the subject, the *Born-Oppenheimer approximation* is discussed. Here also, many-electron wave functions and operators important to quantum chemistry and their matrix elements are described. The chapter continues with a discussion of another approximation which is central to quantum chemistry, the *Hartree-Fock approximation*. Not only is this approximation central to the ideas taught in basic chemistry about electrons occupying molecular orbitals, it is also a fundamental building block for more sophisticated theories. The theory and implementation of the Hartree-Fock approximation is discussed. The process of computationally implementing the Hartree-Fock approximation is called *the self-consistent field* (SCF) *method*.

Next comes the subject of *configuration interaction* (CI). Configuration interac-

tion is a somewhat brute force technique which attempts to solve the Schrödinger equation directly as a basic eigenvalue equation. It accomplishes this by making a basis out of the results of a self-consistent field calculation, expands the Hamiltonian and diagonalizes the resulting matrix to get the eigenvalues and wave functions of the system. Due to computational limitations the basis developed by configuration interaction in practice is far from complete. Therefore, this method can only be pushed so far for large systems. After configuration interaction the subject of *multi-configurational self-consistent field* (MCSCF) is discussed, mostly in the context of the state-averaged MCSCF procedure. This is a generalization of the self-consistent field method to consider more than just a single determinant. In addition, it is useful for improving the results of a configuration interaction calculation. Finally, I discuss the combination of the the MCSCF and CI methods.

The goal of this chapter is to familiarize the casual reader with enough of the core material of quantum chemistry so as to make clear the discussion of the potential energy surfaces which I present later in this work. To this end only the areas of the subject relevant to producing said surfaces are discussed. The fundamental ideas presented in the beginning are done so in considerable detail with the exception of some rather tedious derivations. As one progresses through the chapter the details become increasingly more complex. Since our purpose here is not to review all of quantum chemistry, the focus slowly shifts away from the details and to the conceptual ideas behind the various techniques. This is done in conjunction with pointing to relevant references for those interested in a more sophisticated discussion. The majority of the material presented in this chapter follows closely with the presentation of reference Szabo and Ostlund [1989]. Reference Helgaker et al. [2000] will be drawn upon often as well.

2.1 The Electronic Problem

The aim of this section is to set up the formalism through which one begins to develop approximate solutions to the time-independent Schrödinger equation

$$\hat{H} \mid \Phi\rangle \ = E \mid \Phi\rangle, \tag{1}$$

for a system of nuclei and electrons. A quantum mechanical operator will be indicated by the presence of a "hat" over the letter representing it, i.e., $\hat{H}$ is the Hamiltonian. The position vectors for the nuclei and electrons shall be denoted by $\boldsymbol{R}_A$ and $\boldsymbol{r}_i$, respectively. The distance between electrons i and j will be denoted $r_{ij} =\mid \boldsymbol{r}_{ij} \mid = \mid \boldsymbol{r}_i - \boldsymbol{r}_j \mid$. Likewise, the distance between nuclei A and B is $R_{AB} =\mid \boldsymbol{R}_A - \boldsymbol{R}_B \mid$, and the distance between electron i and nucleus A is $r_{iA} =\mid \boldsymbol{r}_i - \boldsymbol{R}_A \mid$. Let ∇_i^2 and ∇_A^2 be the Laplacian operators with respect to the i_{th} electron's and A_{th} nucleus' coordinates. M_A is equal to the ratio of the mass of nucleus A to the mass of an electron.

In Equation (1), E is the energy (or eigenvalue of $\hat{H}$) associated with the general wave function (or eigenfunction of $\hat{H}$) Φ, where Phi depends on

$$\Phi = \Phi(\{\boldsymbol{r}_i\}; \{\boldsymbol{R}_A\}).$$

The argument $(\{\boldsymbol{r}_i\}; \{\boldsymbol{R}_A\})$ in the wave function means that Φ is a function of the set of all the electronic coordinates $\{\boldsymbol{r}_i\}$ as well as the set of all of the nuclear coordinates $\{\boldsymbol{R}_A\}$. The reason for referring to this as the general wave function will become clear after the next subsection on the Born-Oppenheimer approximation.

The Hamiltonian $\hat{H}$ must involve terms for the kinetic energies of both electrons and nuclei, the repulsive potential energy due to electron-electron and nuclei-nuclei interactions and finally the attractive potential energy due to electron-nuclei interactions. Using atomic units and working in the position basis allows the Hamiltonian

$\hat{H}$ for a system of N electrons and M nuclei to be written as

$$\begin{aligned}\hat{H} &= -\sum_{i=1}^{N}\frac{1}{2}\nabla_i^2 - \sum_{A=1}^{M}\frac{1}{2M_A}\nabla_A^2 - \sum_{i=1}^{N}\sum_{A=1}^{M}\frac{Z_A}{r_{iA}} \\ &\quad + \sum_{i=1}^{N}\sum_{j>i}^{N}\frac{1}{r_{ij}} + \sum_{A=1}^{M}\sum_{B>A}^{M}\frac{Z_A Z_B}{R_{AB}}. \end{aligned} \tag{2}$$

Here Z_A refers to the atomic number of the Ath nuclei. Z_B is analogous. The index j is always greater than i in the fourth term (as the index B is always greater than A in the fifth term) to avoid double counting the same pair of electrons (nuclei).

2.1.1 The Born-Oppenheimer Approximation.

The Hamiltonian presented above leads to a Schrödinger equation Equation (1) whose exact solution is impractical to obtain for all but the most simple cases, the hydrogen atom being the simplest of these. If any progress is to be made beyond these few textbook examples, one must simplify the problem with appropriate approximations. To this end we shall invoke the Born-Oppenheimer Approximation (BOA).

The BOA relies on the following picture. The electrons move very fast compared to the much more massive nuclei. As a result, when solving for the electronic motion the nuclei are assumed to be stationary. This is known as the fixed nuclei approximation. A Hamiltonian for this kind of system is greatly simplified from Equation (2) since the nuclei's coordinates simply label the positions of stationary point charges. Examining Equation (2) under these conditions we see the kinetic energy term of the nuclei must be zero since they are stationary. The repulsive potential for the nuclei is constant. Adding this constant to the Hamiltonian will only add to its eigenvalues and do

nothing to its wave functions. After removing these two terms we are left with

$$\hat{H}_{\text{elec}} \;=\; -\sum_{i=1}^{N}\frac{1}{2}\nabla_i^2 - \sum_{i=1}^{N}\sum_{A=1}^{M}\frac{Z_A}{r_{iA}} + \sum_{i=1}^{N}\sum_{j>i}^{N}\frac{1}{r_{ij}}. \tag{3}$$

Solving a Schrödinger equation which only includes the terms in $\hat{H}_{\text{elec}}$

$$\hat{H}_{\text{elec}} \mid \Phi_{\text{elec}}\rangle \;= E_{\text{elec}} \mid \Phi_{\text{elec}}\rangle, \tag{4}$$

yields wave functions $\Phi_{\text{elec}}(\{\boldsymbol{r}_i\};\{\boldsymbol{R}_A\})$ which depend explicitly on the electrons coordinates $\boldsymbol{r}_i$ but only parametrically on the nuclear coordinates $\boldsymbol{R}_A$. In addition, the energy $E_{\text{elec}}(\{\boldsymbol{R}_A\})$ is a function of the nuclear coordinates.

Since the constant nuclear repulsion term was left out of $\hat{H}_{\text{elec}}$ that energy must be added back in if we are to get the correct potential energies. Therefore,

$$E_{\text{tot}}(\{\boldsymbol{R}_A\}) = E_{\text{elec}}(\{\boldsymbol{R}_A\}) + \sum_{A=1}^{M}\sum_{B>A}^{M}\frac{Z_A Z_B}{R_{AB}}, \tag{5}$$

which is also parametrically dependent on nuclear coordinates.

After solving the electronic problem Equation (4) one can use this solution to formulate the problem of the nuclear motion. To handle this, the BOA makes the following assumption: since the nuclei move so slow compared to the electrons, the average value of the electronic coordinates (calculated from the electronic wave functions $\Phi_{\text{elec}}(\{\boldsymbol{r}_i\};\{\boldsymbol{R}_A\})$) may be substituted into the Hamiltonian in Equation (2).

Thus, we arrive at the following form for the nuclear Hamiltonian $\hat{H}_{\text{nucl}}$

$$\begin{aligned}
\hat{H}_{\text{nucl}} &= -\sum_{A=1}^{M} \frac{1}{2M_A}\nabla_A^2 + \left\langle -\sum_{i=1}^{N} \frac{1}{2}\nabla_i^2 - \sum_{i=1}^{N}\sum_{A=1}^{M} \frac{Z_A}{r_{iA}} + \sum_{i=1}^{N}\sum_{j>i}^{N} \frac{1}{r_{ij}} \right\rangle \\
&\quad + \sum_{A=1}^{M}\sum_{B>A}^{M} \frac{Z_A Z_B}{R_{AB}} \\
&= -\sum_{A=1}^{M} \frac{1}{2M_A}\nabla_A^2 + E_{\text{elec}}(\{\boldsymbol{R}_A\}) + \sum_{A=1}^{M}\sum_{B>A}^{M} \frac{Z_A Z_B}{R_{AB}} \\
&= -\sum_{A=1}^{M} \frac{1}{2M_A}\nabla_A^2 + E_{\text{tot}}(\{\boldsymbol{R}_A\}). \qquad (6)
\end{aligned}$$

Here the $\langle ... \rangle$ notation refers to the average. It is seen from this equation that $E_{\text{tot}}(\{\boldsymbol{R}_A\})$provides a potential energy surface which can be used to describe the nuclear motion. Indeed, plugging $\hat{H}_{\text{nucl}}$ in the Schrödinger equation,

$$\hat{H}_{\text{nucl}} \mid \Phi_{\text{nucl}}\rangle \; = E_{\text{BOA}} \mid \Phi_{\text{nucl}}\rangle, \qquad (7)$$

gives a solution Φ_{nucl} for the nuclear motion, which includes translational, rotational and vibrational information. E_{BOA} is the BOA to the total energy and is a sum of electronic, translational, rotational and vibrational contributions to the energy. The BOA approximation to the general wave function from Equation (1) is

$$\Phi(\{\boldsymbol{r}_i\};\{\boldsymbol{R}_A\}) = \Phi_{\text{elec}}(\{\boldsymbol{r}_i\};\{\boldsymbol{R}_A\})\Phi_{\text{nucl}}(\{\boldsymbol{R}_A\}). \qquad (8)$$

A major goal of ab initio calculations is the accurate generation of potential energy surfaces for nuclear motion, i.e. solving the electronic problem Equation (4) for the energy eigenvalues $E_{\text{elec}}(\{\boldsymbol{R}_A\})$ as a function of nuclear coordinates. This can be thought of as a classical interaction potential for the interacting particles (the nuclei) which move on classical trajectories, or it may be substituted into Equation (7) for

a quantum treatment of the nuclear dynamics within the BOA. As such, the rest of this chapter is devoted to solving Equation (4) and all subscripts will be dropped. When referring to $\hat{H}$, Φ or E assume they refer to their electronic versions unless the text explicitly states otherwise.

2.1.2 The Symmetrization Postulate.

Thus far nothing has been said about the spin of the electron. Indeed, $\hat{H}_{\text{elec}}$ (and therefore Φ_{elec}) only depends on the electron's spatial coordinates, but a complete description of the electron must take spin into consideration. To handle this an arbitrary spin variable ω is introduced along with the spin functions $\alpha(\omega)$ and $\beta(\omega)$. The form of these functions is not explicit, but they are required to span the spin space and they must satisfy orthonormality conditions,

$$\begin{aligned} \angle\alpha \mid \beta\rangle &= \langle\beta \mid \alpha\rangle = 0 \\ \langle\alpha \mid \alpha\rangle &= \langle\beta \mid \beta\rangle = 1. \end{aligned} \tag{9}$$

Here the inner-product notation $< \alpha \mid \beta >= \int \mathrm{d}\omega \ \alpha^*(\omega)\beta(\omega)$ is introduced. Notice that in this notation the variable of integration for the inner product (here ω) correspond to the variable which are defined in the functions whose inner product is to be taken (here $\alpha(\omega)$ and $\beta(\omega)$).

The electron is now to be completely described by combining its spatial variables with its spin variable. This combination is denoted by $\boldsymbol{x}_i$,

$$\boldsymbol{x}_i = (\boldsymbol{r}_i, \omega_i), \tag{10}$$

for the i^{th} electron, and the wave function $\boldsymbol{\Phi}$ of an N electron system depends on

these variables:

$$\mathbf{\Phi} = \mathbf{\Phi}(\boldsymbol{x}_1, \boldsymbol{x}_2, \ldots, \boldsymbol{x}_N). \tag{11}$$

Although spin is now formally included in the wave function, the Hamiltonian for the system makes no reference to it. To make spin meaningful we must further constrain our wave functions beyond the Schrödinger equation by invoking the symmetrization postulate of quantum mechanics [Cohen-Tannoudji et al., 2005]: *a many-electron wave function must be antisymmetric with respect to the interchange of the coordinate* $\boldsymbol{x}$ *(both space and spin) of any two electrons (electrons are fermions).* That is,

$$\mathbf{\Phi}(\boldsymbol{x}_1, \ldots, \boldsymbol{x}_i, \ldots, \boldsymbol{x}_j, \ldots, \boldsymbol{x}_N) = -\mathbf{\Phi}(\boldsymbol{x}_1, \ldots, \boldsymbol{x}_j, \ldots, \boldsymbol{x}_i, \ldots, \boldsymbol{x}_N), \tag{12}$$

where the combined coordinates for the i^{th} electron is exchanged with the combined coordinates for the j^{th} electron.

2.1.3 Orbitals.

An orbital is a wave function for a single electron. A spatial orbital $\psi_i(\boldsymbol{r})$ is defined such that $\mid \psi_i(\boldsymbol{r}) \mid^2 \, \mathrm{d}\boldsymbol{r}$ is the probability of finding the electron inside an infinitesimal volume $\mathrm{d}\boldsymbol{r}$ centered at the point $\boldsymbol{r}$. Any collection of spatial orbitals are assumed to be orthonormal, that is,

$$\langle \psi_i \mid \psi_j \rangle = \int \mathrm{d}\boldsymbol{r} \, \psi_i^*(\boldsymbol{r}) \psi_j(\boldsymbol{r}) = \delta_{ij}. \tag{13}$$

If the set of spatial orbitals were complete in the sense that they spanned the space L^2, then any physically acceptable function of $\boldsymbol{r}$ would be expressible as a (possibly infinite) linear combination of them. However, computational limitations require finite sets of spatial orbitals $\{\psi_i \mid i = 1, \ldots, K\}$ where K is the total number

of spatial orbitals in the set. This finite set of spatial orbitals only spans a fraction of the complete space. Our results will be exact (up to computational limitations) in this subspace, but will not incorporate contributions which lie outside of the subspace.

This is the first hint of a very tricky part of this business. The art of choosing the subspace (i.e., choosing a set of spatial orbitals ψ_i to begin with) which capture the largest possible contribution to the answer for a given number of orbitals is not always straight forward. This topic will be explored in more detail when basis sets are covered in the Hartree-Fock section of this chapter.

To complete the introduction of the single electron wave function, all that is needed is to add the spin functions discussed in the previous subsection. Define the spin orbital χ by

$$\begin{aligned} \chi(\boldsymbol{x}) &= \psi(\boldsymbol{r})\alpha(\omega), \\ &\text{or} \\ \chi(\boldsymbol{x}) &= \psi(\boldsymbol{r})\beta(\omega). \end{aligned} \tag{14}$$

Our set of K spatial orbitals can now make a set of 2K spin orbitals

$$\begin{aligned} \chi_{2i-1}(\boldsymbol{x}) &= \psi_i(\boldsymbol{r})\alpha(\omega) \\ \chi_{2i}(\boldsymbol{x}) &= \psi_i(\boldsymbol{r})\beta(\omega), \end{aligned} \tag{15}$$

where $i = 1, 2, \ldots, K$. Since both the spatial orbitals and the spin functions are orthonormal, this set of spin orbitals is an orthonormal set as well, and $< \chi_i \mid \chi_j >= \delta_{ij}$.

2.1.4 Hartree Products.

Having introduced the single electron wave function the stage is set to begin building a multi-electronic wave function. To start, consider the following operator

$$\hat{h}(i) = -\frac{1}{2}\nabla_i^2 - \sum_{A=1}^{M} \frac{Z_A}{r_{iA}}. \tag{16}$$

Notice the argument of $\hat{h}(i)$ implies that this operator is dependent exclusively on the ith electron's coordinates. Since $\hat{h}(i)$ depends only upon the i^{th} electron's spatial coordinates, each of the eigenfunctions of the $\hat{h}(i)$ operators can be represented by a spin orbital, see Equation (14). For an N-electron system, denote the eigenfunctions of $\hat{h}(1)$ as the set $\{\chi_i\}$, the eigenfunctions $\hat{h}(2)$ as the set $\{\chi_j\}$, etc. For example,

$$\begin{aligned} \hat{h}(1)\chi_i(\boldsymbol{x}_1) &= e_i\chi_i(\boldsymbol{x}_1) \\ \hat{h}(2)\chi_j(\boldsymbol{x}_2) &= e_j\chi_j(\boldsymbol{x}_2) \\ \hat{h}(N)\chi_k(\boldsymbol{x}_N) &= e_k\chi_k(\boldsymbol{x}_N). \end{aligned} \tag{17}$$

Take note of the indices i, j and k in Equation (17). These indices run over the spectrum of the operators $\hat{h}(1)$, $\hat{h}(2)$ and $\hat{h}(N)$, respectively. Due to computational limitations, the operators we work with will always have a finite spectrum. So, the indices i, j and k will always be discrete and will run from one to the dimensionality of the space.

There corresponds a $\hat{h}(i)$ operator to each electron in the system. If all of these operators were summed the total would add up to electronic Hamiltonian from Equation

(3) minus the terms resulting from electron-electron repulsion, i.e.

$$\begin{aligned} \hat{H}_{\text{one}} &= \sum_{i=1}^{N} \hat{h}(i) \\ &= \hat{H} - \sum_{i=1}^{N} \sum_{j>i}^{N} \frac{1}{r_{ij}}. \end{aligned} \tag{18}$$

The subscript on $\hat{H}_{\text{one}}$ is chosen to reflect that all the terms in this operator depend on only a single electron's coordinates. A first attempt at a multi-electron wave function is obtained by using the eigenfunctions of $\hat{H}_{\text{one}}$.

The first term in $\hat{H}_{\text{one}}$ depends only on electron one's coordinates, $\boldsymbol{x}_1$, the second term in $\hat{H}_{\text{one}}$ depends only on electron two's coordinates, $\boldsymbol{x}_2$, etc. This continues for a total of N terms, which is the number of electrons in the system. The wave functions $\Psi^{\text{HP}}$of $\hat{H}_{\text{one}}$ are products of the eigenfunctions of the single electron operators $\hat{h}(i)$

$$\Psi^{\text{HP}}(\boldsymbol{x}_1, \ldots, \boldsymbol{x}_N) = \chi_i(\boldsymbol{x}_1)\chi_j(\boldsymbol{x}_2)\cdots\chi_k(\boldsymbol{x}_N). \tag{19}$$

A many-electron wave function of this type is known as a Hartree-Product, hence the superscript, HP.

2.1.5 Slater Determinants.

Although a Hartree-Product is a many electron wave function, it is not a candidate for solutions to Equation (1) because it does not satisfy the symmetrization postulate, Equation (12). In fact, the Hartree-Product specifically relates the electronic coordinates $\boldsymbol{x}_i$ to the i^{th} electron. Said differently, the Hartree-Product distinguishes between identical particles (here the electrons) in direct contradiction to the symmetrization postulate. However, if appropriate linear combinations of Hartree-Products are formed it is possible to build fully antisymmetric wave functions out of

them. Consider the two spin orbitals χ_i and χ_j and the two electronic coordinates $\boldsymbol{x}_1$ and $\boldsymbol{x}_2$. For a two electron system, let Ψ_{12}^{HP} and Ψ_{21}^{HP} be defined as follows,

$$\begin{aligned} \Psi_{12}^{\mathrm{HP}}(\boldsymbol{x}_1, \boldsymbol{x}_2) &= \chi_i(\boldsymbol{x}_1)\chi_j(\boldsymbol{x}_2) \\ \Psi_{21}^{\mathrm{HP}}(\boldsymbol{x}_1, \boldsymbol{x}_2) &= \chi_i(\boldsymbol{x}_2)\chi_j(\boldsymbol{x}_1). \end{aligned} \tag{20}$$

The following linear combination of these Hartree-Products is a fully antisymmetric wave function for a two-electron system

$$\begin{aligned} \Psi(\boldsymbol{x}_1, \boldsymbol{x}_2) &= \frac{1}{\sqrt{2}}(\Psi_{12}^{\mathrm{HP}} - \Psi_{21}^{\mathrm{HP}}) \\ \Psi(\boldsymbol{x}_1, \boldsymbol{x}_2) &= \frac{1}{\sqrt{2}}(\chi_i(\boldsymbol{x}_1)\chi_j(\boldsymbol{x}_2) - \chi_i(\boldsymbol{x}_2)\chi_j(\boldsymbol{x}_1)). \end{aligned} \tag{21}$$

This wave function can be rewritten as a normalization factor times the determinant of a two-by-two matrix.

$$\Psi(\boldsymbol{x}_1, \boldsymbol{x}_2) = \frac{1}{\sqrt{2}} \begin{vmatrix} \chi_i(\boldsymbol{x}_1) & \chi_j(\boldsymbol{x}_1) \\ \chi_i(\boldsymbol{x}_2) & \chi_j(\boldsymbol{x}_2) \end{vmatrix}.$$

The generalization of this wave function to an N-electron system is

$$\Psi(\boldsymbol{x}_1, \ldots, \boldsymbol{x}_N) = \frac{1}{\sqrt{N!}} \begin{vmatrix} \chi_i(\boldsymbol{x}_1) & \chi_j(\boldsymbol{x}_1) & \cdots & \chi_k(\boldsymbol{x}_1) \\ \chi_i(\boldsymbol{x}_2) & \chi_j(\boldsymbol{x}_2) & \cdots & \chi_k(\boldsymbol{x}_2) \\ \vdots & \vdots & & \vdots \\ \chi_i(\boldsymbol{x}_N) & \chi_j(\boldsymbol{x}_N) & \cdots & \chi_k(\boldsymbol{x}_N) \end{vmatrix}. \tag{22}$$

A wave function of this form is called a *Slater determinant.* Notice that the exchange of coordinates between two electrons corresponds to the exchange of two rows in the Slater determinant. This changes the sign of the determinant which fulfills the an-

tisymmetric requirement of the wave function. Also, if two electrons have the same coordinates (both space and spin) this corresponds to two equal rows in the determinant, making the determinant zero. So, the Slater determinant satisfies the Pauli exclusion principle which is another consequence of the symmetrization postulate of quantum mechanics.

Equation (22) can be cumbersome to write out when explicitly defining which Slater determinant one is talking about. As such, it is desirable to come up with a short hand notation for identifying Slater determinants. Equation (22) can be completely specified by the following symbol, which includes the normalization,

$$\Psi(\boldsymbol{x}_1, \ldots, \boldsymbol{x}_N) = |\chi_i(\boldsymbol{x}_1)\, \chi_j(\boldsymbol{x}_2)\, \ldots\, \chi_k(\boldsymbol{x}_N)\rangle\,.$$

Notice that only the diagonal elements of the determinant are included in the above ket, and these completely specify the Slater determinant. Further, if the convention is taken to write the orbital that corresponds to $\boldsymbol{x}_1$ first, the orbital which corresponds to $\boldsymbol{x}_2$ second, etc. then the shorthand notation can be further simplified to

$$\Psi(\boldsymbol{x}_1, \ldots, \boldsymbol{x}_N) = |\chi_i\, \chi_j\, \ldots\, \chi_k\rangle\,. \tag{23}$$

There is a subtle but important consequence of satisfying the symmetrization postulate which is worth mentioning at this point. The Hartree-Product was based on an independent electron model, i.e. the coulomb repulsion between electrons was ignored. Therefore, each electron's motion is uncorrelated in the Hatree-Product picture. In building the Slater determinants out of Hartree-Products, coulomb interaction between electrons was still ignored. However, since the probability of two electron's having the same coordinates (both spatial and spin) is now zero in the Slater determinant, the motion of two electrons with the same spin is now correlated

in this picture. In other words, two electrons with the same spin will avoid each other spatially. The motion of two electrons with opposite spins remains uncorrelated. The source of this correlation is purely a quantum mechanical effect which is a direct consequence of the symmetrization postulate and is called *exchange correlation.* See reference Szabo and Ostlund [1989] for a more detailed derivation of how exchange correlation arises mathematically.

For simplicity, from this point forward Slater determinants will simply be referred to as *determinants.*

2.1.6 Operators and Matrix Elements.

It has been shown that determinants satisfy the quantum mechanical requirements on a wave function. In the ab initio process the states of a physical system are represented by linear combinations of very specifically designed determinants (see the section of this chapter on Hartree-Fock). It is necessary to determine how to find the matrix elements for the various operators of quantum chemistry between different determinants. These matrix elements are expressed in terms of integrals over electronic coordinates. A notation for these integrals must first be established.

Very often in this subject one encounters integrals of the same form. These common integrals come in two flavors: integrals involving only one electronic coordinate (one-electron integrals) and integrals involving two electronic coordinates (two-electron integrals). These integrals are further categorized by whether we are integrating over spatial or spin orbitals. The notation for these special integrals is summarized in the Table 1. Be careful to note that, for the two electron integrals, the conventional notation for spatial integrals verses spin integrals differs in the arrangement of both coordinates and complex conjugates. Also, $\hat{\mathcal{P}}_{12}$ is the permutation operator for electronic coordinates $\boldsymbol{x}_1$ and $\boldsymbol{x}_2$. When acting on a function of one of

Table 1. Notations for one- and two-electron integrals over spin orbitals (χ) and spatial orbitals (ψ)

Spin Orbitals

$< i|\hat{h}|j >= \int \mathrm{d}\boldsymbol{x}_1 \; \chi_i^*(\boldsymbol{x}_1)\hat{h}(\boldsymbol{r}_1)\chi_j(\boldsymbol{x}_1)$

$< ij|kl >=< \chi_i\chi_j|\chi_k\chi_l >= \int \mathrm{d}\boldsymbol{x}_1\mathrm{d}\boldsymbol{x}_2 \; \chi_i^*(\boldsymbol{x}_1)\chi_j^*(\boldsymbol{x}_2)r_{12}^{-1}\chi_k(\boldsymbol{x}_1)\chi_l(\boldsymbol{x}_2)$

$< ij||kl >=< ij|kl > - < ij|lk >= \int \mathrm{d}\boldsymbol{x}_1\mathrm{d}\boldsymbol{x}_2 \; \chi_i^*(\boldsymbol{x}_1)\chi_j^*(\boldsymbol{x}_2)r_{12}^{-1}(1-\hat{\mathcal{P}}_{12})\chi_k(\boldsymbol{x}_1)\chi_l(\boldsymbol{x}_2)$

Spacial Orbitals

$(i|\hat{h}|j) = h_{ij} = (\psi_i|h|\psi_j) = \int \mathrm{d}\boldsymbol{r}_1 \; \psi_1^*(\boldsymbol{r}_1)\hat{h}(\boldsymbol{r}_1)\psi_j(\boldsymbol{r}_1)$

$(ij|kl) = (\psi_i\psi_j|\psi_k\psi_l) = \int \mathrm{d}\boldsymbol{r}_1\mathrm{d}\boldsymbol{r}_2 \; \psi_i^*(\boldsymbol{r}_1)\psi_j(\boldsymbol{r}_1)r_{12}^{-1}\psi_k^*(\boldsymbol{r}_2)\psi_j(\boldsymbol{r}_2)$

$J_{ij} = (ii|jj)$ Coulomb integrals

$K_{ij} = (ij|ji)$ Exchange integrals

these coordinates, this operator's effect is to interchange these two coordinates. i.e.,

$$\hat{\mathcal{P}}_{12}\left[\chi_i(\boldsymbol{x}_1)\chi_j(\boldsymbol{x}_2)\right] = \chi_i(\boldsymbol{x}_2)\chi_j(\boldsymbol{x}_1).$$

It is worth noting at this point that special care must be taken when comparing determinants. Due to the notation that is employed here, interchanging two orbitals in the expression for the determinant is equivalent to interchanging two columns in Equation (22). The effect of this is to simply negate the resulting determinant, i.e.,

$$|\chi_1 \cdots \chi_a\chi_b \cdots \chi_N\rangle = -\,|\chi_1 \cdots \chi_b\chi_a \cdots \chi_N\rangle\,.$$

As a result, when comparing two determinants one must pay special attention to the order of their orbitals. For a more detailed discussion of how this works, see reference Szabo and Ostlund [1989].

Having established a notation for electronic integrals it is now possible to state the rules for determining the matrix elements of an arbitrary quantum chemical operator. Consider two different determinants, denoted $|\mathrm{K}\rangle$ and $|\mathrm{L}\rangle$ respectively. For any generic linear operator, $\hat{O}$, the form of the equation for its matrix element between $|\mathrm{K}\rangle$ and $|\mathrm{L}\rangle$, denoted $\langle \mathrm{K}| \hat{O} |\mathrm{L}\rangle$, varies based on how the spin orbitals which comprise $|\mathrm{K}\rangle$ differ from the spin orbitals which comprise $|\mathrm{L}\rangle$.

Let

$$|\mathrm{K}\rangle = |\chi_1 \cdots \chi_m \chi_n \cdots \chi_N\rangle \,,$$

then we consider $|\mathrm{L}\rangle$ to have one of the following forms

$$|\mathrm{L}\rangle = |\mathrm{K}\rangle = |\chi_1 \cdots \chi_m \chi_n \cdots \chi_N\rangle \tag{24}$$

$$|\mathrm{L}\rangle = |\chi_1 \cdots \chi_p \chi_n \cdots \chi_N\rangle \tag{25}$$

$$|\mathrm{L}\rangle = |\chi_1 \cdots \chi_p \chi_q \cdots \chi_N\rangle \,. \tag{26}$$

The first of these is when $|\mathrm{L}\rangle$ is simply equal to $|\mathrm{K}\rangle$. The second form is when $|\mathrm{L}\rangle$ differs from $|\mathrm{K}\rangle$ by one spin orbital. Finally, the third form is when $|\mathrm{L}\rangle$ differs by $|\mathrm{K}\rangle$ by two spin orbitals. If $|\mathrm{L}\rangle$ differs from $|\mathrm{K}\rangle$ by more than two spin orbitals, the matrix element of *any* quantum chemical operator between these two determinants will be zero.

Just as for electronic integrals, quantum chemical operators come in either one-electron, $\hat{O}_1$, or two-electron, $\hat{O}_2$, form. One-electron operators appear in the form

$$\hat{O}_1 = \sum_{i=1}^{N} \hat{h}(i), \tag{27}$$

where $\hat{h}(i)$ depends on only the i^{th} electrons coordinants. Two-electron operators

Table 2. Matrix elements between determinants for one-electron operators

$\hat{O}_1 = \sum_{i=1}^{N} \hat{h}(i)$	
Case 1: $\|\mathrm{K}\rangle = \|\chi_1 \ldots \chi_m \chi_n \ldots \chi_N\rangle$	$\langle K\| \hat{O}_1 \|\mathrm{K}\rangle = \sum_{i=1}^{N} \langle i\| \hat{h} \|i\rangle$
Case 2: $\|\mathrm{K}\rangle = \|\chi_1 \ldots \chi_m \chi_n \ldots \chi_N\rangle$ $\|\mathrm{L}\rangle = \|\chi_1 \ldots \chi_p \chi_n \ldots \chi_N\rangle$	$\langle K\| \hat{O}_1 \|\mathrm{L}\rangle = \langle m\| \hat{h} \|p\rangle$
Case 3: $\|\mathrm{K}\rangle = \|\chi_1 \ldots \chi_m \chi_n \ldots \chi_N\rangle$ $\|\mathrm{L}\rangle = \|\chi_1 \ldots \chi_p \chi_q \ldots \chi_N\rangle$	$\langle K\| \hat{O}_1 \|\mathrm{L}\rangle = 0$

appear in the form

$$\hat{O}_2 = \sum_{i=1}^{N} \sum_{j>i}^{N} \hat{v}(i,j) \equiv \sum_{i<j} \hat{v}(i,j), \tag{28}$$

where $\hat{v}(i,j)$ is an operator involving the i^{th} and j^{th} electronic coordinates. In the follow table of matrix elements for two-electron operators, we will take $\hat{v}(i,j)$ to be the coulomb repulsion between electrons, i.e.

$$\hat{v}(i,j) = r_{ij}^{-1}.$$

Tables 2 and 3 summarize the evaluations of matrix elements for one- and two-electron operators

Table 3. Matrix elements between determinants for two-electron operators

$\hat{O}_2 = \sum_{i<j} r_{ij}^{-1}$	
Case 1: $\|\mathrm{K}\rangle = \|\chi_1 \ldots \chi_m \chi_n \ldots \chi_N\rangle$	$\langle K\| \hat{O}_2 \|\mathrm{K}\rangle = \frac{1}{2} \sum_{i=1}^{N} \sum_{j=1}^{N} \langle ij\| \|ij\rangle$
Case 2: $\|\mathrm{K}\rangle = \|\chi_1 \ldots \chi_m \chi_n \ldots \chi_N\rangle$ $\|\mathrm{L}\rangle = \|\chi_1 \ldots \chi_p \chi_n \ldots \chi_N\rangle$	$\langle K\| \hat{O}_2 \|\mathrm{L}\rangle = \sum_{i=1}^{N} \langle mi\| \|pi\rangle$
Case 3: $\|\mathrm{K}\rangle = \|\chi_1 \ldots \chi_m \chi_n \ldots \chi_N\rangle$ $\|\mathrm{L}\rangle = \|\chi_1 \ldots \chi_p \chi_q \ldots \chi_N\rangle$	$\langle K\| \hat{O}_2 \|\mathrm{L}\rangle = \langle mn\| \|pq\rangle$

2.2 Hartree-Fock

In beginning chemistry classes students are taught a simple picture in which the electrons belonging to molecules occupy molecular orbitals. This picture is, in fact, only an approximation, albeit a very important one, called the Hartree-Fock approximation. The utility of the Hartree-Fock approximation lies not just in the predictions one can make with the theory, but it also acts as a stepping stone to more involved and accurate pictures of molecules. Very few ab initio methods bypass this approximation. In this section the Hartree-Fock approximation will be discussed as well as its implementation in a computational environment.

2.2.1 The Hartree-Fock Equations.

The simplest multi-electronic wave function considered here is one which is represented by a single determinant. Consider an arbitrary determinant $|\Psi\rangle$. The energy

of a system described by this wave function is given by the expectation value of the wave function with the electronic Hamiltonian Equation (3) for an N electron system

$$E = \langle \Psi | \hat{H} | \Psi \rangle .$$

Variation of this wave function is obtained by varying the spin orbitals which comprise the determinant. The variational principle [Cohen-Tannoudji et al., 2005] says that the best possible determinant for the ground state of a system is the one with the smallest energy. Denote the determinant which minimizes the energy by $|\Psi_0\rangle$ and let this determinant have the following form

$$|\Psi_0\rangle = |\chi_1 \cdots \chi_a \chi_b \cdots \chi_N\rangle .$$

Then the minimum energy E_0 is

$$\begin{aligned} E_0 &= \langle \Psi_0 | \hat{H} | \Psi_0 \rangle \\ &= \sum_{i=1}^{N} \langle i | \hat{h} | i \rangle + \frac{1}{2} \sum_{i=1}^{N} \sum_{j=1}^{N} \langle ij | ij \rangle . \end{aligned} \tag{29}$$

Using functional variation (see Szabo and Ostlund [1989] for details) on the set of spin orbitals $\{\chi_i\}$ subject to the constraint that they remain orthonormal, one arrives at the following integro-differential equation

$$\begin{aligned} \hat{h}(1)\chi_a(1) \quad &+ \textstyle\sum_{i \neq a} \left[\int \mathrm{d}\boldsymbol{x}_2 \left| \chi_i(2) \right|^2 r_{12}^{-1} \right] \chi_a(1) \\ &- \textstyle\sum_{i \neq a} \left[\int \mathrm{d}\boldsymbol{x}_2 \chi_i^*(2) \chi_a(2) r_{12}^{-1} \right] \chi_i(1) \quad = \varepsilon_a \chi_a(1), \end{aligned} \tag{30}$$

where ε_a is the orbital energy of χ_a. If M is the total number of nuclei then

$$\hat{h}(1) = -\frac{1}{2}\nabla_1^2 - \sum_{A=1}^{M} \frac{Z_A}{r_{1A}}. \tag{31}$$

Introducing the following two operators (which are referred to as the Coulomb and exchange operators, respectively)

$$\begin{aligned} \mathcal{J}_i(1) &= \int \mathrm{d}\boldsymbol{x}_2 \left|\chi_i(2)\right|^2 r_{12}^{-1} \\ \mathcal{K}_i(1) &= \int \mathrm{d}\boldsymbol{x}_2 \chi_i^*(2) r_{12}^{-1} \hat{\mathcal{P}}_{12} \chi_i(2), \end{aligned} \tag{32}$$

simplifies Equation (30) greatly, which becomes

$$\left[\hat{h}(1) + \sum_{i \neq a} \hat{\mathcal{J}}_i(1) - \sum_{i \neq a} \hat{\mathcal{K}}_i(1)\right] \chi_a(1) = \varepsilon_a \chi_a(1). \tag{33}$$

The operator enclosed by brackets in the Equation (33) is called the Fock operator

$$\hat{f}(1) = \hat{h}(1) + \sum_{i \neq a} \hat{\mathcal{J}}_i(1) - \sum_{i \neq a} \hat{\mathcal{K}}_i(1). \tag{34}$$

The integro-differential equation Equation (30) has become an eigenvalue equation

$$\hat{f}(1)\chi_i(1) = \varepsilon_i \chi_i(1). \tag{35}$$

2.2.2 The Hartree-Fock Approximation.

At the heart of the chemist's view of molecular structure lies a picture which consists of electrons occupying spin orbitals. These spin orbitals are formed out of spatial orbitals, the location of which are centered on atoms and molecules. This is, in fact, an approximation called the Hartree-Fock (HF) Approximation. When the

electronic configuration distributes the electrons throughout the spin orbitals with the lowest possible energies ε_i, so that the energy of the electronic state of the system E_0 is minimized, then the determinant representing this state is the HF ground state $|\Psi_0\rangle$ and the orbitals $\{\chi_i : i = 1, \ldots, N\}$ satisfy Equation (35). This set of orbitals are said to be the exact HF orbitals.

The Fock operator is functionally dependent on its own eigenfunctions. Therefore, it is not a linear operator and Equation (35) is not a linear eigenvalue problem. To see this more concretely, it is convenient to rewrite the Fock operator in a more illuminating form and discuss some of its properties. Observe that

$$\hat{f}(1) = \hat{h}(1) + \hat{v}^{\mathrm{HF}}(1), \tag{36}$$

where, assuming that Fock operator is acting upon orbital χ_a,

$$\hat{v}^{\mathrm{HF}}(1) = \sum_{i \neq a} \mathcal{J}_i(1) - \sum_{i \neq a} \mathcal{K}_i(1). \tag{37}$$

If the second term in Equation (36) were absent, then this operator would simply be the Hamiltonian for the a^{th} electron in a field of fixed point nuclei, and the Fock operator would be linear. All interaction between electrons is contained in $\hat{v}^{\mathrm{HF}}(1)$. Now, if this was the true potential for this situation, then $\hat{v}^{\mathrm{HF}}(1)$ would just be the coulomb interaction between electrons. However, in the HF approximation this potential has been simplified. Looking at the first part of $\hat{v}^{\mathrm{HF}}(1)$, the sum over Coulomb operators

$$\mathcal{J}_i(1)\chi_a(1) = \left[\int \mathrm{d}\boldsymbol{x}_2 \; |\chi_i(2)|^2 \, r_{12}^{-1} \right] \chi_a(1).$$

The quantity $\mathrm{d}\boldsymbol{x}_2 \, |\chi_i(2)|^2$ represents the probability of finding the electron in orbital χ_i

inside an infinitesimal volume centered on $\boldsymbol{x}_2$. Multiplying this term by the Coulomb interaction an electron in orbital χ_a would feel if the i^{th} electron were in this spot, and then integrating over the entire volume results in an averaging of the effects on the a^{th} electron due to the Coulomb interaction with the i^{th} electron. This is summed over i so that the average Coulomb interaction of all other electrons is what the a^{th} electron sees.

Looking at the second part of $\hat{v}^{\mathrm{HF}}(1)$, the sum over exchange operators is given by

$$\begin{aligned} \mathcal{K}_i(1)\chi_a(1) &= \left[\int \mathrm{d}\boldsymbol{x}_2 \chi_i^*(2) r_{12}^{-1} \hat{\mathcal{P}}_{12} \chi_i(2)\right] \chi_a(1) \\ &= \left[\int \mathrm{d}\boldsymbol{x}_2 \chi_i^*(2) r_{12}^{-1} \chi_a(2)\right] \chi_i(1). \end{aligned}$$

If the i^{th} orbital and the a^{th} orbital have opposite spins, then this term is zero. If the spins are the same, this term gives rise to what is called *exchange correlation*. This is a consequence of the symmetrization postulate of quantum mechanics. Its presence is completely unaccounted for in classical theories. The sum of all the exchange effects on the a^{th} electron is included in $\hat{v}^{\mathrm{HF}}(1)$.

Both the Coulomb and exchange operators require a knowledge of the eigenfunctions of the Fock operator. Equation (35) is therefore non-linear, and its solution must be obtained in and iterative manner. In practice, one begins with a guess at the eigenfunctions. Forming the Fock operator and then solving Equation (35) generates new eigenfunctions. This process is repeated until self-consistency is reached. This is the essence of *the Self-Consistent Field* (SCF) method, which is the name of the process by which one solves the Fock eigenvalue equation.

2.2.3 Basis Sets and the Roothaan Equations.

Up to this point spin orbitals have been referred to in only a general way. No effort has been made to describe how one actually generates a spin orbital. To begin this process only *restricted spin orbitals* will be considered here. A restricted spin orbital is of the following form

$$\chi_i(\boldsymbol{x}) = \begin{cases} \psi_{i/2}(\boldsymbol{r})\alpha(\omega) & : \text{ i is even} \\ \psi_{(i+1)/2}(\boldsymbol{r})\beta(\omega) & : \text{ i is odd.} \end{cases} \tag{38}$$

Given a set of K spatial functions, $\{\psi_i : i = 1, \ldots, K\}$, one can form $2K$ restricted spin orbitals. In addition, the Hartree-Fock ground state determinant $|\Psi_0\rangle$ will be assumed to be in *closed shell* form. This means that there are an even number of electrons in the N electron system, and for each spatial orbital which is used to make one of the ground state spin orbitals, both spin up and spin down versions of that spatial orbital are included in the ground state

$$|\Psi_0\rangle = |\chi_1\chi_2 \cdots \chi_{2i-1}\chi_{2i} \cdots \chi_{N-1}\chi_N\rangle \,. \tag{39}$$

Special note should be taken here. In the restricted spin orbital formalism there are a pair of electrons, one spin up and the other down, that share the same spatial orbital. Due to the nature of spin correlation, the spatial motion of electrons with the same spin is correlated via the symmetrization postulate of quantum mechanics. It is entirely conceivable that two electrons which share the same spatial orbital in the restricted spin orbital formalism would feel different exchange correlation effects due to their different spins. As such, it is arguable that all electrons should have their own spatial functions. There is a formalism for spin orbitals which does this very thing, the orbitals of this formalism being called *unrestricted spin orbitals*. Further

information on unrestricted spin orbitals can be found in Szabo and Ostlund [1989]. Such orbitals are not used in any of the ab initio techniques employed in this work, and will not be considered further in this report.

In order to build spin orbitals one must find an appropriate set of spatial orbitals. Toward this goal it is beneficial to simplify the Fock eigenvalue equation, Equation (35), by integrating out the arbitrary spin variable ω. First, suppose $\chi_{2i}(\boldsymbol{x}) = \psi_i(\boldsymbol{r})\alpha(\omega)$. The results are similar for the case where χ_{2i+1} is dependent on $\beta(\omega)$. The simplification of the Fock eigenvalue equation is accomplished by multiplying Equation (35) by $\alpha^*(\omega)$ and integrating over ω

$$\begin{aligned}\left[\int \mathrm{d}\omega\, \alpha^*(\omega)\hat{f}(\boldsymbol{x})\alpha(\omega)\right]\psi_i(\boldsymbol{r}) &= \varepsilon_i\psi_i(\boldsymbol{r})\int \mathrm{d}\omega\, \alpha^*(\omega)\alpha(\omega) \\ &= \varepsilon_i\psi_i(\boldsymbol{r}), \end{aligned} \tag{40}$$

where the second line follows due to the orthonormality of the spin functions.

Evaluating the integral on the left hand side of Equation (40) is tedious and its derivation can be found in Szabo and Ostlund [1989]. The result is a spatial Fock eigenvalue equation

$$\hat{f}(\boldsymbol{r})\psi_i(\boldsymbol{r}) = \varepsilon_i\psi_i(\boldsymbol{r}), \tag{41}$$

where

$$\hat{f}(\boldsymbol{r}) = \hat{h}(\boldsymbol{r}) + \sum_i^{N/2} 2\hat{J}_i(\boldsymbol{r}) - \hat{K}_i(\boldsymbol{r}). \tag{42}$$

The operators $\hat{J}_i$ and $\hat{K}_i$ are the spatial versions of the Coulomb and exchange operators

$$\begin{aligned}\hat{J}_i(\boldsymbol{r_1}) &= \int \mathrm{d}\boldsymbol{r}_2\, \psi_i^*(\boldsymbol{r}_2) r_{12}^{-1}\psi_i(\boldsymbol{r}_2) \\ \hat{K}_i(\boldsymbol{r_1}) &= \int \mathrm{d}\boldsymbol{r}_2\, \psi_i^*(\boldsymbol{r}_2) r_{12}^{-1}\mathcal{P}_{12}\psi_i(\boldsymbol{r}_2). \end{aligned} \tag{43}$$

The expression for the ground state energy E_0 has become

$$\begin{aligned} E_0 &= \langle \Psi_0 | \hat{H} | \Psi_0 \rangle \\ &= 2 \sum_{i=1}^{N} \langle i | \hat{h} | i \rangle + \sum_{i=1}^{N} \sum_{j=1}^{N} \left[2J_{ij} - K_{ij} \right]. \end{aligned} \tag{44}$$

See Table 1 for the meaning of J_{ij} and K_{ij}.

It is Equation (41) which must be solved to find the Hatree-Fock ground state wave function and energy. Numerical approaches to solving this equation do exist for atoms, however no numerical approaches exist for molecules. Instead of dealing with this equation it is possible to reduce Equation (41) to a purely algebraic equation, which can be solved with standard matrix methods. To do this requires the idea of a basis set.

A basis set is a set of known spatial functions that are linearly independent and span the D-dimensional subspace of spacial function (typically atomic like orbitals) $\{\phi_j(\boldsymbol{r}) : j = 1, \ldots, D\}$ where D is the number of functions in the set. This set is partitioned up into distinct subests where all the spatial functions of a particular subset are centered on one of the nuclei. There will be as many of these subsets as there are nuclei. If the total set is linearly independent then D is the dimensionality of the space which the set spans. Ideally its possible to have an infinite basis set. Due to computational limitations this will never happen. The Hartree-Fock ground state spatial orbitals are then expanded in terms of this basis set

$$\psi_i(\boldsymbol{r}) = \sum_{j=1}^{D} C_{ji} \phi_j(\boldsymbol{r}). \tag{45}$$

When working with a specific basis set each spatial orbital ψ_i will be determined uniquely by its coordinates C_{ji} for all $j = 1, \ldots, D$.

Inserting the above expansion (Equation (45)) of the spatial orbitals into Equation

(41) yields

$$\hat{f}(\boldsymbol{r})\sum_{j=1}^{D} C_{ji}\phi_j(\boldsymbol{r}) = \varepsilon_i \sum_{j=1}^{D} C_{ji}\phi_j(\boldsymbol{r}). \tag{46}$$

Multiplying from the left by $\phi_k^*(\boldsymbol{r})$ and integrating over $\mathrm{d}\boldsymbol{r}$ gives

$$\sum_{j=1}^{D} C_{ji} \int \mathrm{d}\boldsymbol{r}\, \phi_k^*(\boldsymbol{r})\hat{f}(\boldsymbol{r})\phi_j(\boldsymbol{r}) = \varepsilon_i \sum_{j=1}^{D} \int \mathrm{d}\boldsymbol{r}\, \phi_k^*(\boldsymbol{r})\phi_j(\boldsymbol{r}). \tag{47}$$

At this point it is required that several matrices be introduced. All of the following matrices are square and have dimension D. The first is the *overlap matrix* $\boldsymbol{S}$ whose elements are

$$S_{kj} = \int \mathrm{d}\boldsymbol{r}\, \phi_k^*(\boldsymbol{r})\phi_j(\boldsymbol{r}). \tag{48}$$

This is a Hermitian matrix and would be the unit matrix of dimension D if the known functions $\phi_i(\boldsymbol{r})$ were orthonormal. The second matrix that needs introduction is the *Fock matrix* $\boldsymbol{F}$ whose elements are

$$F_{kj} = \int \mathrm{d}\boldsymbol{r}\, \phi_k^*(\boldsymbol{r})\hat{f}(\boldsymbol{r})\phi_j(\boldsymbol{r}). \tag{49}$$

This, too, is a Hermitian matrix. The third matrix, denoted $\boldsymbol{C}$, is simply made up of the coefficients of the spatial orbitals in the basis set as defined in Equation (45)

$$\boldsymbol{C} = \begin{pmatrix} C_{11} & C_{12} & \cdots & C_{1D} \\ C_{21} & C_{22} & \cdots & C_{2D} \\ \vdots & \vdots & & \vdots \\ C_{D1} & C_{D2} & \cdots & C_{DD} \end{pmatrix}. \tag{50}$$

Finally, the last matrix that needs introduced is denoted by $\boldsymbol{\varepsilon}$ and has the form

$$\boldsymbol{\varepsilon} = \begin{pmatrix} \varepsilon_1 & 0 & \cdots & 0 \\ 0 & \varepsilon_2 & \cdots & 0 \\ \vdots & \vdots & & \vdots \\ 0 & 0 & \cdots & \varepsilon_D \end{pmatrix}. \tag{51}$$

This matrix has the spatial orbital energies along its diagonal and zeros everywhere else.

In introducing the previous matrices a little hand waving occurred which warrants attention. When the spatial orbitals where expanded in terms of the basis set Equation (45) the focus was on generating the spin orbitals which comprise the Hartree-Fock ground state. In an N electron system (here N is assumed even due to the closed shell formulation of the Hartree-Fock ground state) one would need N spin orbitals to do this. Since two spin orbitals can be made out of every spatial orbital, and each spatial orbital which is included must come with both and alpha and beta spin pair, only $N/2$ spatial orbitals are required. Looking at Equation (45) the index j runs from one to D, the number of spatial functions in the basis set. However, the index i runs from one to $N/2$. In the recently introduced matrices $\boldsymbol{C}$ is square with dimensionality D. Although there must be D rows since this index runs over the basis set, there should only be $N/2$ columns since only this many spatial orbitals are needed. In addition, the matrix of orbital energies should be square, but it should only contain $N/2$ rows and columns, unlike the D rows and columns it has.

What is happening here is that more molecular orbitals have been made out of the atomic basis sets than are needed to form the Hartree-Fock ground state. These extra orbitals are still present in the above matrices. Only the orbitals which make up the ground state will be optimized by the SCF procedure, while the extra

orbitals will remain unoptimized. All we will be guaranteed of is all spatial orbitals made will be orthonormal. Beyond this, the extra orbitals don't contribute to the calculation and don't even need to be present for the SCF to work. However, they are calculated because they will be useful when it comes time to consider the *configuration interaction* method.

Having these matrices firmly in hand, it is time to write down Roothaan's equations. This is a rewrite of Equation (41) in matrix form.

$$\boldsymbol{FC} = \boldsymbol{SC}\boldsymbol{\varepsilon}. \tag{52}$$

Roothaan's equations present an example of a *generalized eigenvalue problem*. This is very similar to a standard eigenvalue problem, except the basis that is being employed is not necessarily orthonormal. This is a consequence of the set of known spatial functions $\{\phi_j(\boldsymbol{r})\}$ which we choose to form the basis set. The solution of the Roothaan's equations simply adds the extra steps of changing to an orthonormal basis before solving the eigenvalue problem, and then changing back to the original basis afterwards. The details of this process can be found in Szabo and Ostlund [1989].

2.2.4 The Self Consistent Field Procedure.

Armed with the content of this chapter up to this point, it is now possible to discuss the self consistent field (SCF) procedure, at least at a cursory level. As was mentioned before, an SCF calculation is a numerical routine which arrives at an approximation of the Hartree-Fock ground state wave function $|\Psi_0\rangle$ for a particular molecular arrangement, i.e. a particular set of nuclear coordinates for some physical system consisting of nuclei and electrons. An outline of the SCF procedure follows.

1. Identify the charge Z_A and location $\boldsymbol{R}_A$ of all nuclei in the system. Choose a set of spatial functions $\{\phi_j(\boldsymbol{r})\}$ to form the basis set.

2. Formulate a guess at the starting electronic wave function for the system.

3. Form the Fock matrix $\boldsymbol{F}$ from the guess for the electronic wave function.

4. Solve Roothaan's equations for a new guess at the electronic wave function.

5. If the new wave function has changed more than a set tolerance then go back to step 3 using the new wave function. If the wave function has converged then use the current wave function to calculate the electronic energy of the system.

Under the Born-Oppenheimer Approximation, the solution to the electronic Hamiltonian depends parametrically on the coordinates of all the nuclei in the system. To begin the SCF procedure step one sets up the nuclear arrangement. It is also necessary to identify the set of spatial functions in which we shall expand the spatial orbitals which form the Hartree-Fock ground state. If one were to have a *complete* set of spatial functions at one's disposal, then the SCF procedure would produce the exact Hartree-Fock ground state orbitals and wave function. Since such a complete set would need to be infinite, there is no such complete set of spatial functions available. Therefore, the result of the SCF procedure can only be considered exact (within computational limitations) in a subspace of the total space for the problem. Due to this the choice of basis set is not altogether straight forward, although there exists insight which makes this process easier than stumbling around blindly in the dark. For more information on this subject see Szabo and Ostlund [1989].

Step two of the SCF procedure calls for an initial guess at the ground state wave function of the N electron system. While many different approaches for this exist, two of the more common approaches are called $\hat{H}^{\text{core}}$ and Huckle. The $\hat{H}^{\text{core}}$ approach starts with the electronic Hamiltonian and removes all terms involving electron-electron interaction. It then solves this Hamiltonian, which is the equivalent of a system of N electrons traveling in the field of the nuclei without interacting

at all with each other, as the initial guess for the SCF. The Huckle approach involves making an empirical guess for ground state wave function. The last three steps of the SCF procedure are self explanatory, although there is a considerable amount of detail involved in their implementation.

The ground state wave function supplies a knowledge of the ground state energy, along with numerous other physical quantities of interest, for the particular nuclear arrangement which is considered. Multiple SCF's at different nuclear coordinates can produce a potential energy surface which defines the nuclear motion of a system in the ground state.

2.3 Configuration Interaction

Configuration Interaction (CI) is an ab initio method which approaches solving the electronic Hamiltonian for the system in a direct fashion by expanding it in a basis of determinants and diagonalizing to find the eigenvalues and wave functions for the different states. The basis used to expand the Hamiltonian is generated from the results of a SCF calculation, so SCF (or MCSCF, which will be discussed later in this chapter) is a prerequisite for CI. If one were not limited by computational constraints CI would produce *exact* results within the confines of the Born-Oppenheimer approximation. This section discusses extensions to our description of the wave function for a state of the system which is required for the CI formalism. In addition, it discusses the various approaches to CI, i.e. different ways to form the determinantal basis.

2.3.1 Excited Determinants.

With the introduction of the basis set $\{\phi_j : j = 1, \ldots, D\}$ in the SCF procedure $2D$ spin orbitals were generated, although only N of these were needed to form the Hatree-Fock ground state determinant $|\Psi_0\rangle$. Indeed, it was only these N spin orbitals,

the Hatree-Fock orbitals, which were optimized during the SCF procedure. The other $2D - N$ orbitals did not take part in the optimization, although we are assured that all $2D$ spin orbitals are orthonormal. Denote the extra $2D - N$ orbitals as *virtual orbitals*. With all of these orbitals available, many more determinants can be made than just $|\Psi_0\rangle$. In fact, the total number of determinants which may be formed is just the number of ways N electrons may be arranged in $2D$ spin orbitals. This is given by the binomial coefficient

$$\text{Number of Determinants} = \left(\begin{array}{c} 2D \\ N \end{array} \right) = \frac{(2D)!}{N!(2D-N)!}. \tag{53}$$

Since $|\Psi_0\rangle$ is considered the ground state determinant, all other determinants are called *excited determinants*. A convenient way of labeling these determinants is to use the Hartree-Fock ground state as a base line and keep track of how much each determinant differs from $|\Psi_0\rangle$, i.e. how many spin orbitals does the excited determinant possess which are not present in the Hatree-Fock ground state determinant? Remember, $|\Psi_0\rangle$ is defined as

$$|\Psi_0\rangle = |\chi_1 \dots \chi_a \chi_b \dots \chi_N\rangle \,.$$

In this notation the indices $a, b, \dots$ run over the Hatree-Fock spin orbitals. When refering to virtual orbitals the indices $r, s, \dots$ will be used. The first category of excited determinants will be defined as any determinant which differs from $|\Psi_0\rangle$ by only one spin orbital. A determinant of this type will be called a *singly excited determinant* and will be represented by

$$|\Psi_a^r\rangle = |\chi_1 \dots \chi_r \chi_b \dots \chi_N\rangle \,. \tag{54}$$

The next category of excited determinants will be those which differ from $|\Psi_0\rangle$ by two orbitals. These determinants will be called *doubly excited determinants* and have the form

$$|\Psi_{ab}^{rs}\rangle = |\chi_1 \cdots \chi_r \chi_s \cdots \chi_N\rangle \,. \tag{55}$$

Continuing in this way one can define triply $|\Psi_{abc}^{rst}\rangle$, quadruply $|\Psi_{abcd}^{rstu}\rangle$, ..., N-tuply $|\Psi_{ab\ldots}^{rs\cdots}\rangle$ excited determinants.

2.3.2 Multiconfigurational Wave Functions.

In a Hartree-Fock calculation one attempts to find the best representation of the ground state of the system using an N-electron wave function of single determinant form. This representation is constrained by both the Born-Oppenheimer and Hartree-Fock approximations. This begs the question: Is it possible to get a better approximation of the ground state of the system by using more than one determinant to represent the wave function?

Suppose the SCF procedure was carried out using a complete basis set $\{\phi_j(\boldsymbol{r})\}$. If one were to form all possible determinants from the spin orbitals generated by the SCF this set $\{|\Psi_0\rangle, |\Psi_a^r\rangle, |\Psi_{ab}^{rs}\rangle, \ldots\}$ would form a complete basis for the N-electron space. As such, any state of the system $|\Phi\rangle$ could be expressed as a linear combination of these determinants

$$|\Phi\rangle = C_0 |\Psi_0\rangle + \sum_{a=1}^{N} \sum_{r=N+1}^{2D} C_a^r |\Psi_a^r\rangle + \sum_{a<b} \sum_{r<s} C_{ab}^{rs} |\Psi_{ab}^{rs}\rangle + \ldots \tag{56}$$

The meaning of $a < b$ and $r < s$ in the last term of the previous equation is that a and r will run over their normal values, 1 to N and $N+1$ to $2D$ respectively, while b and s will run from $a+1$ to N and $r+1$ to $2D$ respectively. This avoids double counting the contribution of any determinant.

A wave function expanded in such a basis of determinants is called a *multiconfigurational wave function.*

2.3.3 Correlation Eneregy.

The only form of electron correlation that the Hartree-Fock approximation handles explicitly is the exchange correlation which arrises by imposing the symmetriztion postulate on the form of the wave function. The Coulomb interaction inbetween electrons is handled only in an average way. Even if one were working with complete basis sets the energy obtained, the so called the *Hartree-Fock limit* E_0, would not be the exact ground state energy $\mathcal{E}_0$. In fact $E_0 > \mathcal{E}_0$ because of the variational principle. The difference E_{corr} where

$$E_{\text{corr}} = \mathcal{E}_0 - E_0, \tag{57}$$

is always negative and is called the *correlation energy*, since the source of this energy is interacting electrons. It is the goal of the *configuration interation*, as well as other post Hartree-Fock methods, to recover as much of this correlation energy as possible.

2.3.4 Configuration Interaction.

The previous section asserts that if we start with a complete basis set then the Hartree-Fock procedure generates a complete N-electron basis within which *any* state of the system, not just the ground state, may be *exactly* represented. Armed with such an N-electron basis it is possible to approach solving Equation (4) directly by expanding the electronic Hamiltonian within the basis and diagnolizing the resulting matrix. Unfortunately a complete basis set must be infinite and computational limitations require finite dimensional basis sets. One can still form a basis of determinants from the Hartree-Fock procedure, but this basis will only span a subspace of the N-electron space. Nevertheless such an effort can still produce approximations to not

only the ground state wave function, but excited state wave functions as well. This process is called *full CI* (FCI). The *FCI matrix* is the matrix formed by expanding the electronic Hamiltonian in the discrete basis of determinants.

The Hartree-Fock procedure always produces a discrete number of determinants in which to expand the electronic Hamiltonian, but just how many determinants of some n excitations does it produce? Given $2D$ spin orbitals the Hartree-Fock ground state $|\Psi_0\rangle$ will contain N of these orbitals. This leaves $2D - N$ orbitals unoccupied in the ground state, denote these *virtual orbitals*. For some specific number of excitations n, this number represents how many orbitals must be chosen out of the ground state and replaced with virtual orbitals. This can occur in $\binom{N}{n}$ possible ways. Likewise, the n orbitals chosen from the set of virtual orbitals results in $\binom{2D}{n}$ combinations. The product of these two is the number of determinants of n excitations made out of the basis set and generated during the Hartree-Fock procedure.

$$\text{Number of determinants of n excitation} = \binom{N}{n}\binom{2D}{n}. \tag{58}$$

Consider the exact ground state of the electronic Hamiltonian, denote it $|\Phi_0\rangle$. Rewriting the expansion of $|\Phi_0\rangle$ the following way

$$|\Phi_0\rangle = c_0 |\Psi_0\rangle + c_S |S\rangle + c_D |D\rangle + c_T |T\rangle + \ldots, \tag{59}$$

will allow for a much simpler expression for the FCI matrix. Here we have simply lumped all coefficients and determinants of n excitations into a single term. For example, all determinants of single excitations have been lumped into $|S\rangle$ and their coefficients lumped into c_S. This is done because determinants of the same excitation share many properties in common, as is explained in the next paragraph.

Before writing down the expression for the FCI matrix a few points should be considered. First, due to Brillouin's theorem [Szabo and Ostlund, 1989] all matrix elements between the Hartree-Fock ground state $|\Psi_0\rangle$ and any singly excited states $|S\rangle$ are zero. Second, from the rules derived for matrix elements earlier in the chapter, any element of the FCI matrix which is formed between two determinants that differ by more than two excitations is automatically zero. Lastly, a value of zero for a matrix element between two states means that the states do not mix directly. By *mix* it is meant that the states are correlated. However, the first state may mix with other states which mix directly with the second state. For example, $|\Psi_0\rangle$ does not mix with states of single excitation. It does mix with states of double excitations, and states of double excitations mix with states of single excitation. In this way states which do not mix directly still can have an effect on each other, although usually this effect is much smaller than that of determinants which mix directly. In addition to what has been discussed in this paragraph the spin of determinants and molecular symmetry can be used to simplify the FCI matrix by determining that certain matrix elements must be zero.

Since the FCI matrix is Hermitian only the upper triangular portion will be needed.

$$\begin{bmatrix} \langle\Psi_0|\hat{H}|\Psi_0\rangle & 0 & \langle\Psi_0|\hat{H}|D\rangle & 0 & 0 & \cdots \\ & \langle S|\hat{H}|S\rangle & \langle S|\hat{H}|D\rangle & \langle S|\hat{H}|T\rangle & 0 & \cdots \\ & & \langle D|\hat{H}|D\rangle & \langle D|\hat{H}|T\rangle & \langle D|\hat{H}|Q\rangle & \cdots \\ & & & \langle T|\hat{H}|T\rangle & \langle T|\hat{H}|Q\rangle & \cdots \\ & & & & \langle Q|\hat{H}|Q\rangle & \cdots \\ & & & & & \vdots \end{bmatrix}. \tag{60}$$

The the diagonalization of this matrix provides a series of eigenvalues. The lowest

of these is an upper bound to the ground state energy. The next lowest is an upper bound to the first excited state, and so on. The wave functions associated with these eigenvalues are approximations to the N-electron wave function for the associated state.

2.3.5 Singles and Doubles CI.

By the nature of the binomial coefficient the number of determinants which can be produced from the Hartree-Fock procedure quickly grows very large, even with a modest amount of basis functions and electrons. This leads to a FCI matrix which becomes too large to be diagonalized by modern computers. As a result, the prospect of implementing FCI quickly becomes computationally impractical. Therefore, in order to salvage the method some approach to truncating the FCI basis of determinants must be developed.

A quick and easy way to truncate the determinantal basis is to exclude all determinants of a certain excitation or higher. A common form of this truncation is called *configuration interaction singles and doubles*(CISD). In this method only determinants of at most two excitations are kept in the basis. This is especially useful for approximating the correlation energy to obtain the exact ground state since doubly excited determinants are the only ones which mix directly with the Hartree-Fock ground state. Single excitations are not as important for this purpose because they contribute very little to the correlation energy. However, they are useful in calculating other physical properties of the ground state and there are so few of them that including them does not complicate the calculation in a significant way.

The truncated FCI matrix takes on the following form for CISD

$$\begin{bmatrix} \langle \Psi_0 | \hat{H} | \Psi_0 \rangle & 0 & \langle \Psi_0 | \hat{H} | D \rangle \\ & \langle S | \hat{H} | S \rangle & \langle S | \hat{H} | D \rangle \\ & & \langle D | \hat{H} | D \rangle \end{bmatrix}. \tag{61}$$

Although this approach can do quite well with the ground state, excited state information is not expected to be very accurate. This is because the excited states mix directly with determinants of higher than double excitation. Additionally, the molecular orbitals which are used to form the excited determinants have not been optimized by the SCF like the orbitals in the Hartree-Fock ground state. In order to handle excited states one must include higher excitations in the determinantal basis. However, including all the triple excitations makes the determinantal basis much too large for even systems with moderately sized basis sets and number of electrons. In the truncated CI approach, the determinants with an even number of excitations recover a vast majority of the correlation energy, while determinants with an odd number of excitations have very little impact. Thus after CISD one would go to CISDTQ and skip the triple step entirely. This combined with the computational inability to perform even triple excitations makes many problems untenable with this approach. However, if we employ a truncation scheme which will cherry pick among the determinants of higher than double excitation, choosing some subset of them to be included in the truncated FCI matrix, we can make significantly more progress. Thus far we have been considering systems dominated by one electronic configuration, namely the Hartree-Fock ground state $|\Psi_0\rangle$. The path toward a smarter choice for the truncation for the FCI matrix is to consider systems dominated by more than one electronic configuration.

2.4 Multi-configurational Self-Consistent Field

As its name implies, Multi-configurational Self-Consistent Field (MCSCF) is an extension to the SCF method (and the Hartree-Fock approximation). Like SCF, MCSCF is an iterative procedure where one begins with a guess, feeds it into the non-linear differential equations and then uses the results to form the next guess. During this process the spatial orbitals used in the calculation are optimized. Unlike SCF, MCSCF allows for multiple electronic configurations through the use of multiple reference wave functions (as opposed to Hartree-Fock's use of just one reference Slater determinant). As a result it optimizes more of the spacial orbitals than a SCF calculation. Every spacial orbital used in the MCSCF expansion of the wave function gets optimized during the MCSCF procedure. MCSCF can also handle excited states in addition to the ground state. The spatial orbitals can be optimized for any particular state, or they can be optimized to give the best results for some combination of states. One can even apply different weights for different states in the optimization process. Due to the computational demands of the MCSCF procedure relatively few determinants can be handled. This severely limits the quality of energies calculated by MCSCF, specifically the method's ability to capture the correlation energy due to the Coulomb interaction between electrons. However, the mulitreference character of the MCSCF wave function allows it to incorporate well the correlation between states when their energies become nearly degenerate. This type of electron correlation is called *static correlation* and is something single reference systems like Hartree-Fock and CISD fail to capture well. MCSCF works well in conjunction with an multireference extension to CISD in cases where both static and Coulomb correlation energies are important. The multireference extension to CISD will be discussed next.

2.4.1 The MCSCF Procedure.

Given a basis set consisting of D linearly independent spatial functions an SCF calculation will produce $2D$ spin orbitals. Out of all these orbitals only N orbitals are optimized by the SCF calculation, leaving $2D - N$ orbitals unoptimized. A MCSCF calculation builds upon the ideas of the SCF. Instead of solving for the best (in a variational sense) wave function of single determinant form, a MCSCF wave function allows for a multireference wave function of the following form

$$|\Psi_{\text{MCSCF}}\rangle = \sum_I c_I |\Psi_I\rangle , \tag{62}$$

where the $|\Psi_I\rangle$'s are some subset of determinants which form the full expansion in Equation (56). Each of the spin orbitals which form the various $|\Psi_I\rangle$'s includes a spatial orbital $\psi_i(\boldsymbol{r})$ which has its own expansion coefficients in terms of the basis set, see Equation (45).

An MCSCF calculation, similarly to a standard SCF calculation, is an iterative procedure which optimizes, according to the variational principle, not only the expansion coefficients c_I of a state of the system but also the expansion coefficients of the orbitals which comprise the different determinants $|\Psi_I\rangle$. Through choosing which determinants to include in the MCSCF expansion one is able to optimize more of the spin orbitals than just the ones required to form the Hartree-Fock ground state $|\Psi_0\rangle$. In addition, an MCSCF calculation is not limited to only the ground state as is a SCF calculation, but it can provide excited state information as well. It can optimize the expansions in terms of the determinants chosen for any single state, ground or excited, or even multiple states simultaneously. Optimizing for multiple states simultaneously will lead to different orbital optimizations than if one were to consider just a single state. So, the orbitals are optimized in a way to give the best

overall results for a multitude of states or the best orbitals for any particular state considered in isolation. The general equations which must be solved for an MCSCF calculation are considerably more involved than those of the Hartree-Fock procedure (Roothaan's equations in the closed shell restricted Hartree-Fock case). A detailed discussion of the implementation of MCSCF may be found in Helgaker et al. [2000].

2.4.2 Multireference Configuration Interaction Singles and Doubles.

For small systems quite accurate results may be obtained with the use of the MCSCF technique. Due to computational limitations, as the size of the system increases the number of determinants used in the MCSCF expansion Equation (62) of the wave functions of interest must be limited to a number usually much smaller than even a basis of determinants constructed for a singles and doubles CI calculation. As such, MCSCF by itself is not a very useful technique for most realistic problems where the Coulomb correlation between electrons is significant. That being said MCSCF maintains its utility through its ability to improve the results of other ab initio calculations.

MCSCF's ability to optimize more spatial orbitals than what are required for the Hartree-Fock ground state provides a means to improve a singles and doubles CI calculation. This is accomplished by using these optimized orbitals in the construction of the basis of determinants for the CI expansion. However, as was mentioned above, due to the computational limitations of the MCSCF procedure the number of determinants it can handle is usually much less than the number in even a singles and doubles CI basis set. As such there's no way it can optimize all the orbitals used in all determinants in the set generated by the CI truncation scheme. Some subset of the molecular orbitals generated from the atomic basis sets must be selected for use in the MCSCF calculation. The way I do this is by using a complete active space

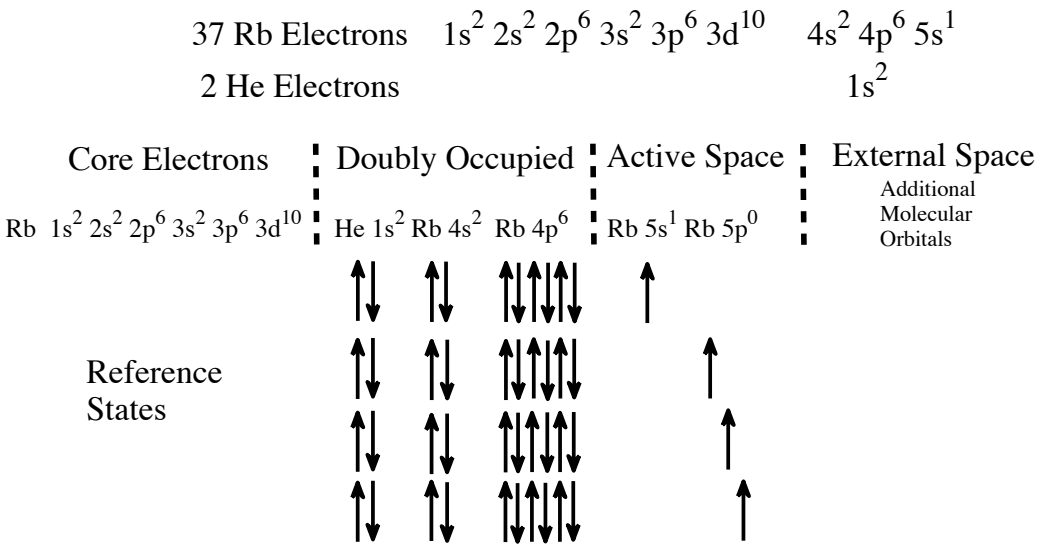

Figure 1. The reference states used in calculating the $M + Ng$ potential energy curves. Reference states are written in terms of the atomic states to which they dissociate in the separated atom limit. My choice of active space results in four reference determinates corresponding to the ground and first three excited states of the alkali metal atom.

(CAS).

In the CAS method determinants for the multireference wave function are constructed as follows. All doubly occupied molecular orbitals of the Hartree-Fock ground state are present and doubly occupied in all of the determinants for the wave function expansion. All singly occupied molecular orbitals of the Hartree-Fock ground state in addition to some subset of orbitals formed from the atomic bases sets but not included in the Hartree-Fock ground state form the active space. Any electrons which occupied the orbitals which came from the Hartree-Fock ground state are also placed into the active space. One can then imagine the set of all permutations of the electrons within the various orbitals of the active space. We form the reference determinates for the multireference wave function expansion by appending one of the permutations from the active space to the doubly occupied orbitals in the Hartree-Fock ground state.

Figure 1 shows an example of a set of reference determinants generated from the

CAS approach for the Rb + He calculations examined in this work. All other M + Ng combinations differ only in the doubly occupied orbitals and have the same structure for the active space. We write the molecular orbitals in terms of the dissociated atom limit, and these reference states dissociate to the $^2S_{1/2}$, $^2P_{1/2}$, and $^2P_{3/2}$ alkali metal states with the noble gas in the ground state. This active space has four molecular orbitals and one electron, thus there are four ways to permute the electron among these orbitals. This results in four reference state determinants for the multirefernce wave function expansion. It is the molecular orbitals which are used to form the reference determinants which are optimized by the MCSCF, and in such a way that one can weight whichever states one's interested in. For the calculations in this work I weight all four states obtained from the four reference determinants equally.

Once the MCSCF is completed, the reference states and their orbitals are optimized and a multirefernce configuration interaction singles and doubles (MRCISD) is performed. This works very similarly to a CISD, except that each reference determinant is used as a base from which to make single and double excitations. These excitations are made by placing electrons into molecular orbitals which lie in the external space, so no active space orbital may be excited into. Since we are performing double excitations on reference determinants which are already singly occupied, we are effectively mixing in some but not all triple excitations. The electronic Hamiltonian is then expanded in terms of the N electron basis set formed from all of the determinants generated by these excitations, as well as the reference determinants themselves. One then just has to diagonalize to find the electronic wave functions and energy levels.

The advantage of using MCSCF over SCF as a precursor to the CI calculation is that the MCSCF will optimize all orbitals of the active space, where as the SCF optimizes only the molecular orbitals comprising the Hartree-Fock ground state de-

terminant. As the reference determinants formed from the CAS method are the most physically relevant determinants it is beneficial to optimize all the orbitals which comprise these determinants. In addition, in MCSCF the orbitals may be optimized for whatever state (or states) are of interest, where as the SCF optimizes only for the ground state. Following a MCSCF with a MRCISD calculation recovers much of the Coulomb correlation energy missed by the MCSCF.

III. M+Ng Potential Energy Curves

It is shown in Sanders [1973] that one can use measured broadening and shifting coefficients to calculate a difference potential (DP) of the Lenard-Jones form which, when used in the Anderson Talman line shape theory, will yield back the measured broadening and shifting coefficients. These DPs were calculated from measured coefficients of rubidium with a variety of collisional partners in Rotondaro and Perram [1997], and from measured coefficients of cesium with a variety of collisional partners in Pitz et al. [2009], and Pitz et al. [2010]. Such a DP is shown in Figure 2. Note that the Lenard-Jones DP has a repulsive wall around $\approx 10\mathring{A}$ and a minimum of about $\approx 0.8cm^{-1}$ at $\approx 12.5\mathring{A}$. It is natural to assume that the Lenard-Jones DP contains information about what the real DP must look like. In this chapter we will explore how the ab initio potential energy curves (PECs) dramatically change the picture of what the real DPs look like. Later is this work we will learn what features the real DPs share with the Lennard-Jones DPs so as to yield the same broadening and shifting coefficients.

3.1 MCSCF PECs

3.1.1 Description of the MCSCF calculations.

In this section several types of calculations have been employed to compute $M + Ng$ PECs, including restricted open-shell Hartree-Fock (ROHF), MCSCF, MRCISD [Knowles et al., 2000] and first order relativistic corrections, including spin-orbit [Fedorov et al., 2003]. Here a MRCISD calculation with first order relativistic corrections will be refered to as a *spin orbit configuration interaction* (SOCI) calculation. A series of $X^2\Sigma$, $A^2\Pi$ and $B^2\Sigma$ curves have been computed at the MCSCF level for alkali-metal atoms M = Li, Na, K, Rb and Cs and noble-gas atoms Ng = He, Ne and Ar

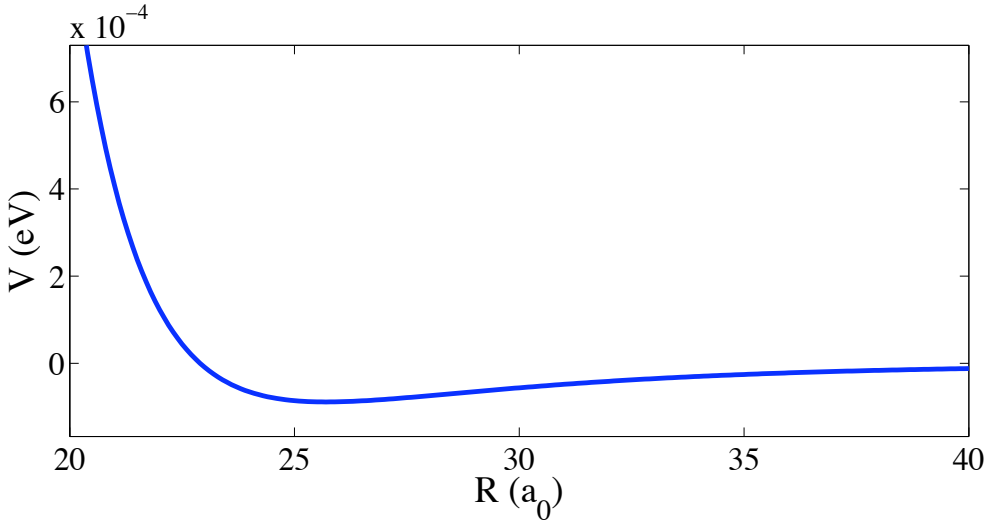

Figure 2. A Lennard-Jones difference potential derived from broadening and shifting measurements of Rb + He.

and provide a semi-quantitative picture of the interaction. This allows the comparison of various features for the different combinations. In addition, $X^2\Sigma^+_{1/2}$, $A^2\Pi_{1/2}$, $A^2\Pi_{3/2}$ and $B^2\Sigma^+_{1/2}$ curves have been generated for Li + He using SOCI. All calculations performed in this section were made using the *General Atomic and Molecular Electronic Structure System* (GAMESS) program [Schmidt et al., 1993].

The basis sets used for the MCSCF calculations are the split-valance Def2SVP [Weigend and Ahlrichs, 2005]. The basis set used for the Li + He SOCI calculation is the quadruple zeta Def2QZVPP [Weigend and Ahlrichs, 2005]. These basis sets have been obtained from the EMLS Basis Set Exchange [Feller, 1996, Schuchardt et al., 2007]. For alkali-metal atoms Li through K and for all noble-gas atoms considered, the basis sets include all the electrons. However, twenty-eight core electrons of the rubidium atom and forty-six core electrons of the cesium atom have been replaced with Stuttgart effective core potentials (ECP) [Leininger et al., 1996]. The reference space for the MCSCF calculation consists of four determinants obtained from an active space with one electron in the ^2S and ^2P orbitals on the alkali-metal atom, as shown in Figure 1. All other electrons remain doubly occupied including those on

the noble-gas atom, which eliminates electron correlation contributions to the inter-atomic interaction. These molecular states dissociate to the appropriate atomic states of the alkali-metal atom with the noble-gas atom in the ground state.

The active space for the Li + He SOCI curves consists of all doubly occupied orbitals and the singly occupied orbital in the Hartree-Fock ground state determinant, as well as the three lowest-energy orbitals unoccupied in the Hartree-Fock ground state determinant. After the MRSDCI is complete spin-orbit corrections are computed using the full Pauli-Breit operator [Fedorov et al., 2003].

3.1.2 Comparison of MCSCF vs. SOCI curve for Li + He.

The MCSCF $M + Ng$ curves provide a picture of the interaction between M and Ng as well as a systematic way to see similarities and differences for different combinations of alkali-metal atoms and noble-gas atoms. Before proceeding to discuss the MCSCF curves it is informative to check the accuracy these surfaces provide by comparing them with the SOCI calculation of the Li + He curve. These two curves are plotted in Figure (3).

The main features (the shoulder in the $B^2\Sigma$ state, the well in the $A^2\Pi$ state, etc.) for both plots are similar. However, the shoulder in the $B^2\Sigma$ curve near $R = 4a_0$ is significantly smaller in the SOCI curve. The $X^2\Sigma$ curve changes very little with a slight lowering of the repulsive wall which causes it to grow more slowly with decreasing internuclear separation (R). This is seen to much greater degree in the $B^2\Sigma$ curve. In addition, the $B^2\Sigma$ curves decrease more slowly for R greater than five Bohr radii (a_0). The main quantitative change in the $A^2\Pi$ curve can be seen in the well region, for which experimental data is available and listed in Table (4). While the MCSCF and SOCI curves exhibit differences, their over all similarity suggests that the basic picture of the $M + Ng$ interaction is captured by the MCSCF curves.

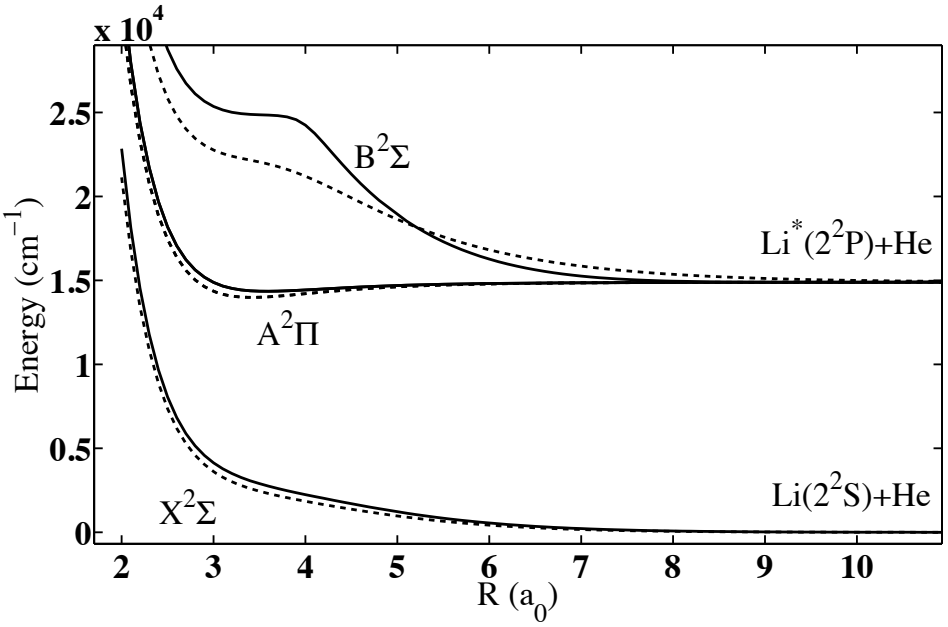

Figure 3. Comparison of Li + He MCSCF (solid) vs. MRSDCI (dashed)

Table 4. $A^2\Pi$ **Well for Li + He**

Method	r_{min}	Depth
MCSCF	3.60	546
SOCI	3.43	907
exp[1]	3.37(3)	1020(20)

[1]Lee and Havey [1991]

3.1.3 Results of PEC calculations.

The results of the MCSCF calculations of the excited $A^2\Pi$ and $B^2\Sigma$ states are presented in Figures 4-8. In these figures the asymptotic limit of the ^2P state of the alkali-metal atom has been set to zero. As expected, all of the repulsive walls move to larger values of R as the size of the atoms involved increases. Each of the $A^2\Pi$ curves demonstrate a shallow well which tends to get deeper as the noble-gas atoms and the alkali-metal atoms become heavier. Lithium is an exception to this rule, exhibiting a deeper well for helium than for neon. Each $B^2\Sigma$ state, with the exception of Na + Ne and Na + Ar, reveals a shoulder in the rise of the repulsive barrier. This shoulder is most pronounced for lithium and tends to drop off in abruptness as the alkali-metal atom under consideration gets heavier. The ground $X^2\Sigma$ curves are shown in Figures 9-13. These curves are mostly repulsive, exhibiting very shallow wells at $R > 10a_0$, ranging in depth from $1cm^{-1}$ to $40cm^{-1}$. This is consistent with the work of Goll et al. [2006]. Note that in these Figures 9-13 the energy scale is too large to see the wells.

A close up of the asymptotic limit for the $^2P_{1/2}$ and $^2P_{3/2}$ for the SOCI with spin-orbit corrections calculation of Li + He is shown in Figure 14 between $10a_0$ and $50a_0$. The $^2P_{1/2}$ state of lithium has been chosen as the zero for the plot. In the asymptotic limit the degenerate $^2P_{3/2}$ levels with $m_j = \pm\frac{3}{2}$ correspond to the $A^2\Pi_{3/2}$ curve while the $m_j = \pm\frac{1}{2}$ levels correspond to the $B^2\Sigma$ curve. The area of the plot around $R = 17a_0$ where the $B^2\Sigma$ curve exhibits a well is an avoided crossing. Non-adiabaticity in this region is one of the two mechanisms responsible for collisionally induced fine structure transitions in the lithium during the interaction with the helium. The second mechanism is a Coriolis coupling between the $^2\Pi_{3/2}$ and $^2\Pi_{1/2}$ curves that becomes important at smaller values of R [Elward-Berry and Berry, 1980].

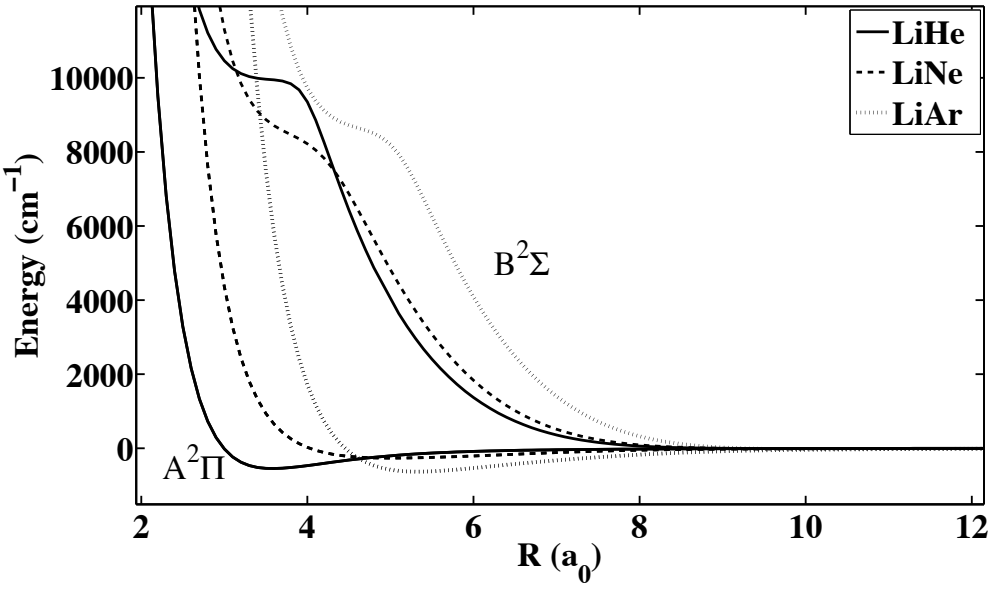

Figure 4. MCSCF excited surfaces of Li + Ng

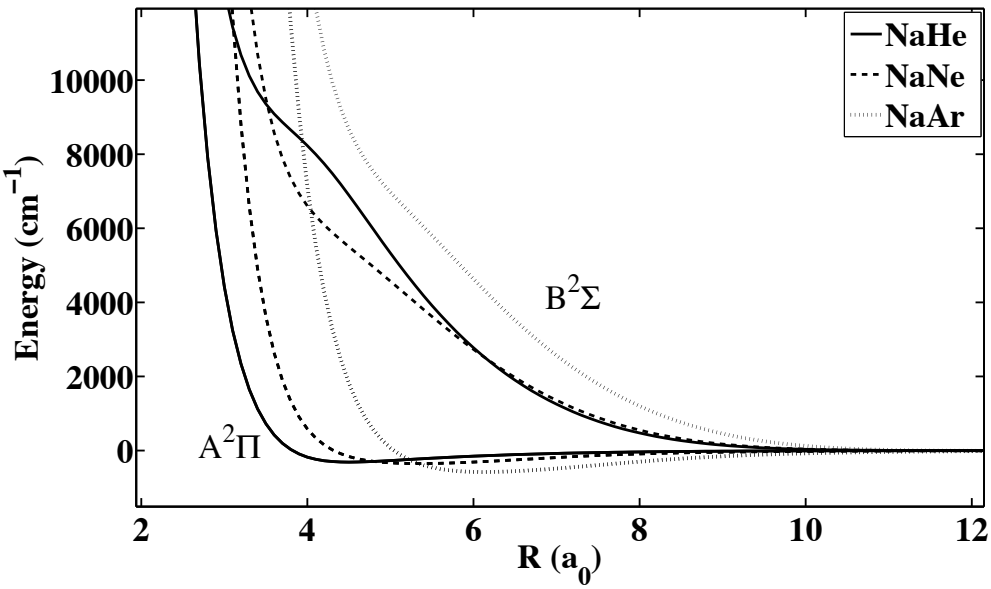

Figure 5. MCSCF excited surfaces of Na + Ng

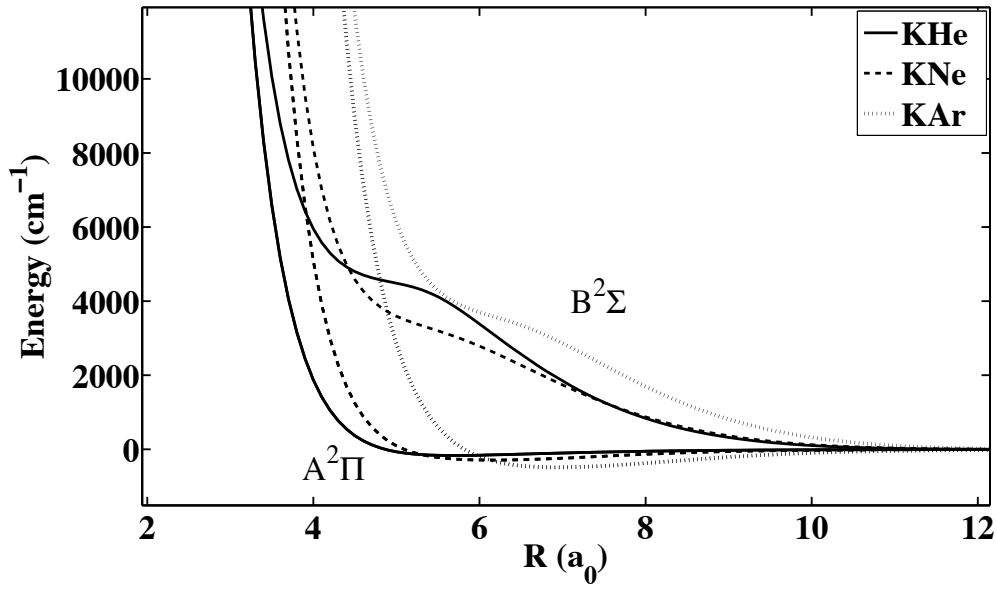

Figure 6. MCSCF excited surfaces of K + Ng

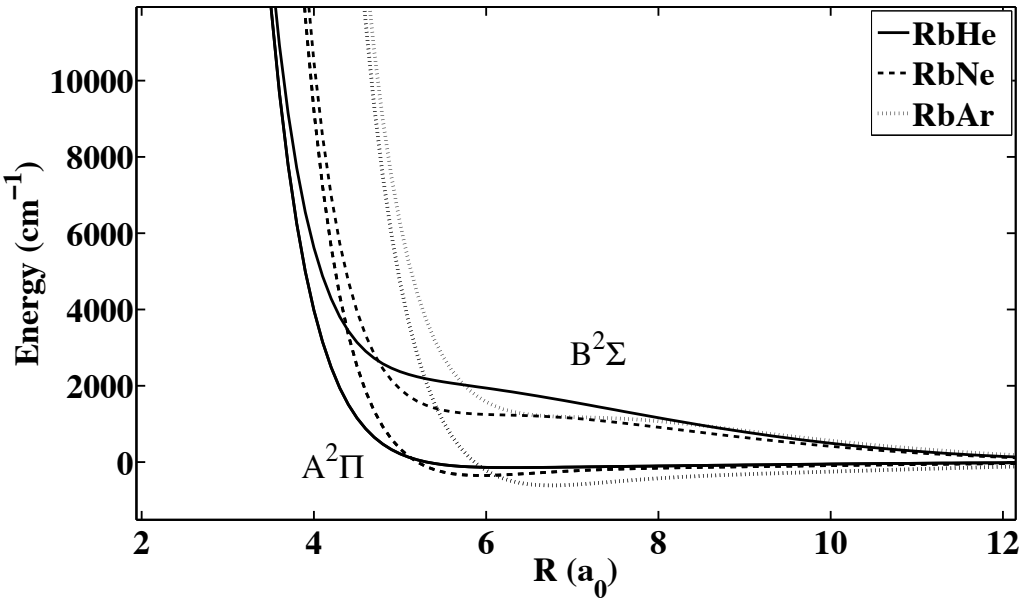

Figure 7. MCSCF excited surfaces of Rb + Ng

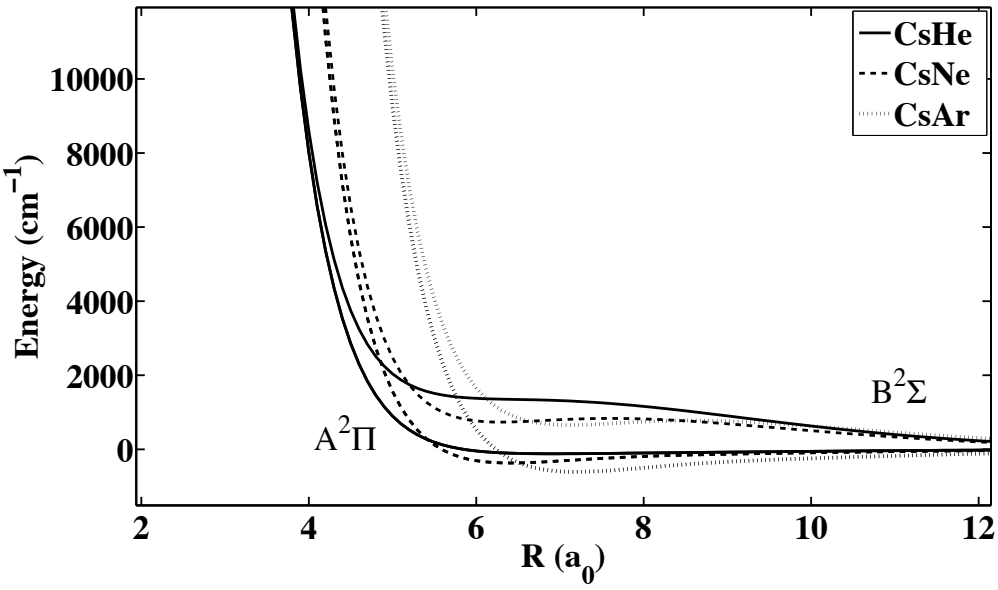

Figure 8. MCSCF excited surfaces of Cs + Ng

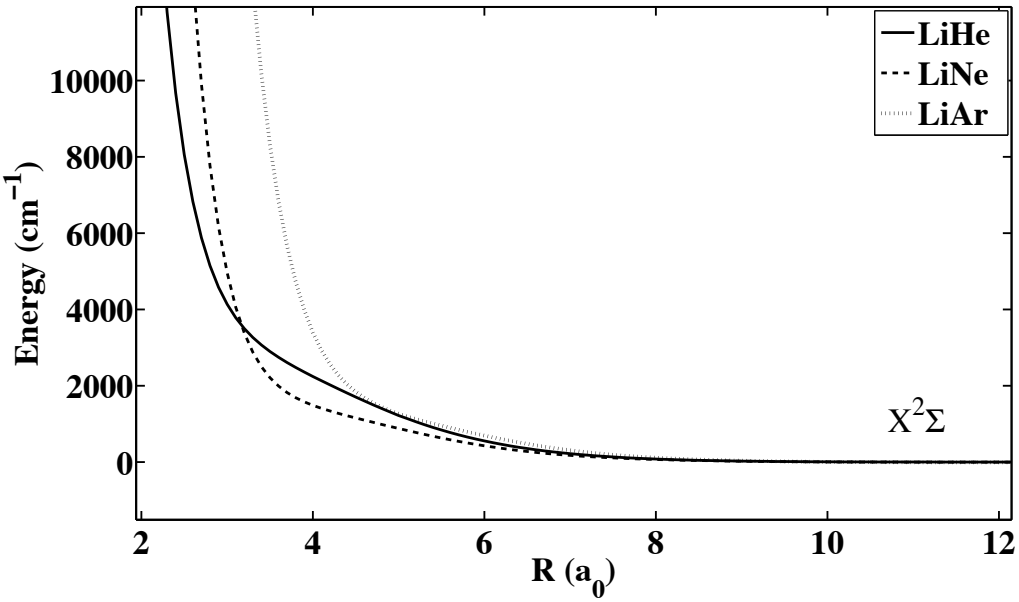

Figure 9. MCSCF ground surfaces of Li + Ng

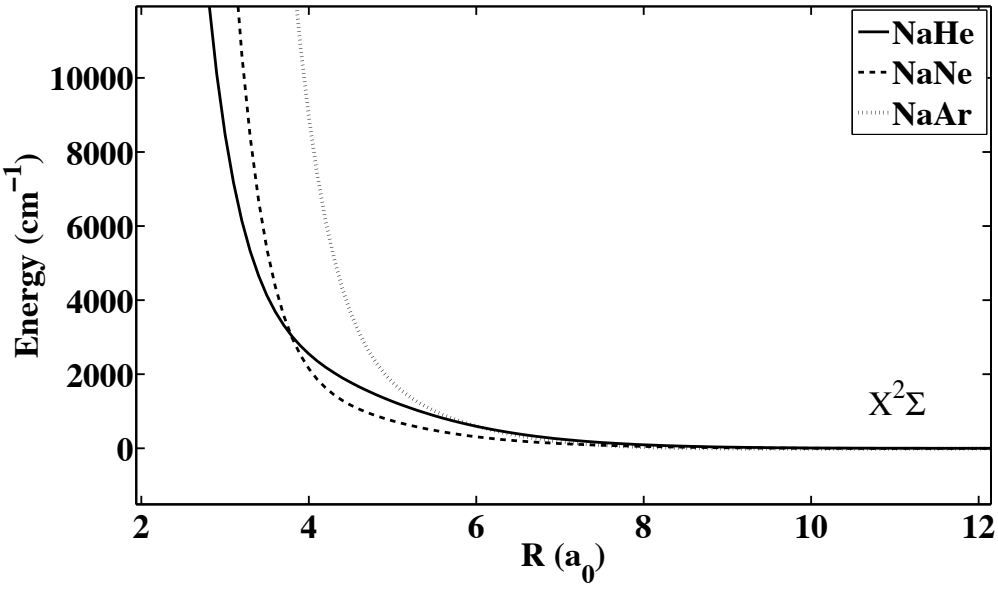

Figure 10. MCSCF ground surfaces of Na + Ng

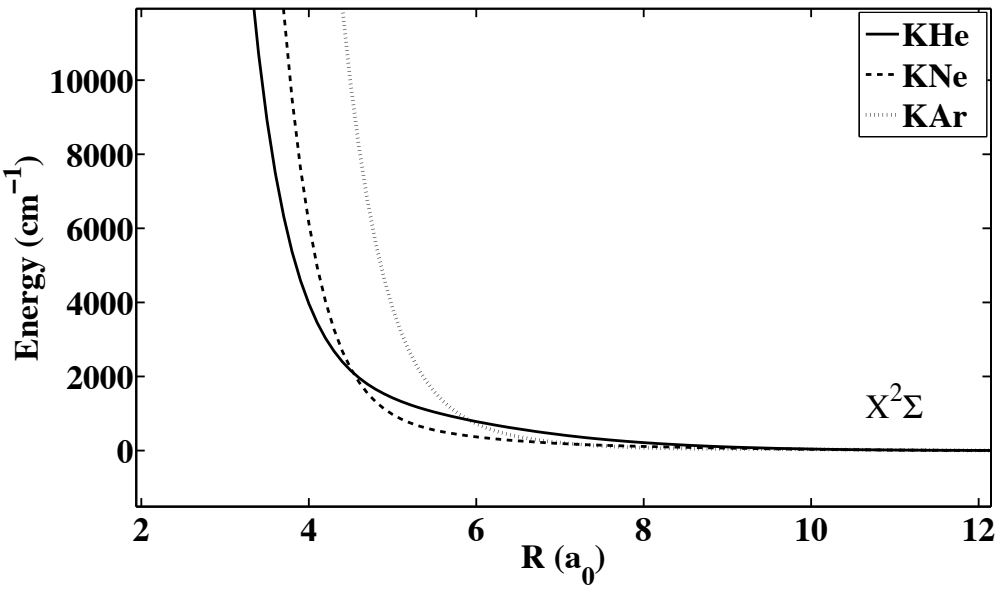

Figure 11. MCSCF ground surfaces of K + Ng

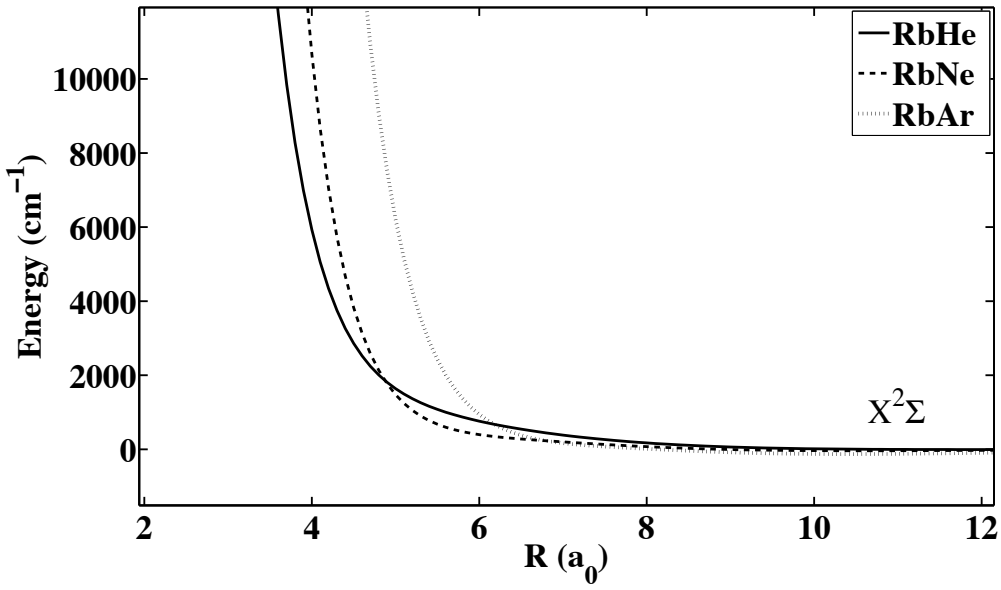

Figure 12. MCSCF ground surfaces of Rb + Ng

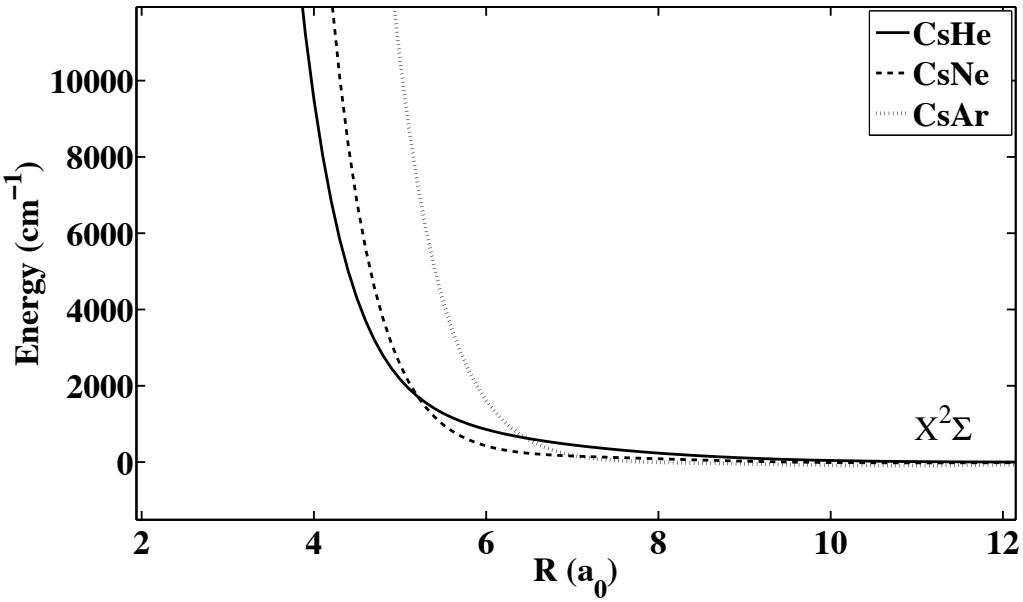

Figure 13. MCSCF ground surfaces of Cs + Ng

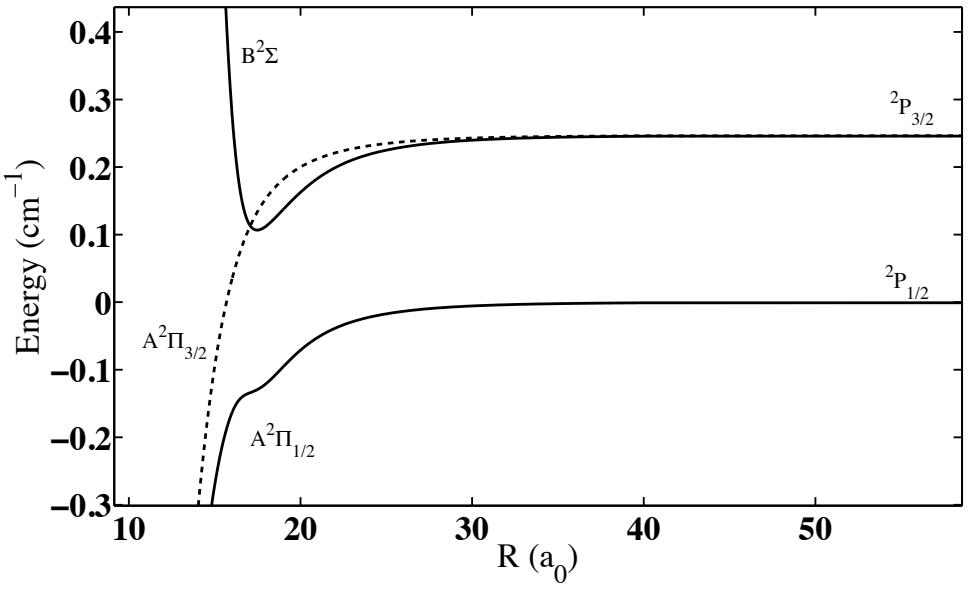

Figure 14. Asymptotic limit of Li + He for its excited states

3.1.4 The evolution of the line broadening picture as a result of the ab initio calculations.

Up to this point PECs have been computed for the interaction between the alkali-metal atoms M = Li, Na, K, Rb and Cs with the noble-gas atoms Ng = He, Ne and Ar at the MCSCF level. A comparison between the MCSCF Li + He curves and the SOCI Li + He curves indicate that the MCSCF curves provide a semi-quantitative picture of the $M + Ng$ interactions. The SOCI Li + He curves also show that when spin orbit effects are included the $A^2\Pi$ curve spits into $A^2\Pi_{1/2}$ and $A^2\Pi_{3/2}$ curves. DPs given by $\Delta V_{\Pi_{1/2}}(R) = A^2\Pi_{1/2}(R) - X^2\Sigma(R)$, $\Delta V_{\Pi_{3/2}}(R) = A^2\Pi_{3/2}(R) - X^2\Sigma(R)$, and $\Delta V_{\Sigma}(R) = B^2\Sigma(R) - X^2\Sigma(R)$ can be used to investigate line broadening mechanisms in OPAL systems. These DPs, calculated using our more advanced PECs discussed next, are shown in Figures 30, 31, and 32. The DPs generated from the ab initio PECs dramatically differ from the Lennard-Jones DPs.

The classical impact theory of pressure broadening takes as input these DPs and

returns a Lorentzian line shape with a width and shift. For the broadened D_1 line this DP is simply $\Delta V_{\Pi_{1/2}}(R)$. However, as seen in Figure (14), if the M atom starts in the $^2P_{3/2}$ state then, depending on its m_j value, the molecular molecular dynamics will be governed by either the $A^2\Pi_{3/2}$ curve or the $B^2\Sigma$ curve. This implies that the line shape for the D_2 state will have two DPs, $\Delta V_{\Pi_{3/2}}(R)$ and $\Delta V_{\Sigma}(R)$, which determine its form.

The remainder of this chapter will be dedicated to quantitatively improving the $M + Ng$ PECs and discussing the trends there in. In Chapter V we will explore how two very clearly different sets of DPs can yield the same broadening and shifting coefficients, as well as how different molecular states which are degenerate in the asymptotic limit combine to form one line shape.

3.2 Multireference Configuration Interaction Singles and Doubles Potential Energy Curves

3.2.1 Computational Approach.

The $X^2\Sigma^+_{1/2}$, $A^2\Pi_{1/2}$, $A^2\Pi_{3/2}$, and $B^2\Sigma^+_{1/2}$ PECs and dipole transition moments of $M + Ng$ are computed at the spin-orbit multi-reference singles and doubles configuration interaction (SOCI) level for M = K,Rb,Cs and Ng =He,Ne,Ar using the *COLUMBUS* suite of programs [Lischka et al., 1981, Shepard et al., 1988, Lischka et al., 2001, 2006, Yabushita et al., 1999]. The small core Stuttgart relativistic pseudopotentials (PPs) and corresponding basis sets [Lim et al., 2005] are used for the alkali-metal atoms in these calculations. These PPs consist of all but nine valance electrons for each alkali-metal atom. For an ns^1 alkali-metal atom, the nine valance electrons are the $(n-1)s^2$, $(n-1)p^6$, and ns^1 electrons. The Def2-TZVPP all electron segmented contracted Gaussian basis sets [Weigend and Ahlrichs, 2005] are used for the noble-gas atoms.

The SOCI calculation employs state-averaged multi-configuration self-consistent field (MCSCF) reference orbitals [Blank et al., 2010]. In terms of the dissociated atom limit, the $ns^1\ ^2S$ ground and all three $np^1\ ^2P$ excited states of the alkali-metal atom are included in the state averaging procedure with equal weights. The complete active space consists of one electron in the ns and three np orbitals, and the resulting four configuration state functions (CSFs) comprise the reference space for the SOCI calculation. For these calculations all single and double excitations of the nine alkali-metal electrons and the two, ten, and eighteen noble-gas atom electrons, for He, Ne, and Ar respectively, are used to generate the spin adapted CSFs that comprise the SOCI n-electron basis. The maximum multiplicity of any of the CFSs is six, and the number of CSFs included in the SOCI calculations range from $\approx 10^6$ for K + He to $\approx 10^8$ for Cs + Ar. While significant computational savings occur when the core orbitals of Ne and Ar are frozen, slightly lower variational energies are obtained for our calculations by leaving all noble-gas atom electrons active.

Several other active spaces were considered for various $M + Ng$ combinations to explore possible improvements to the SOCI calculation. Each additional active space considered includes only the ns alkali-metal electron and is extended beyond the nsnp active space by including additional alkali-metal atom orbitals. For Rb + He the additional active spaces are 5s5p6s6p4d and 5s5p6s6p4d7s7p5d, and the corresponding SOCI results in the asymptotic limit of large R are summarized in Table 5. In this limit, the SOCI energies approach the experimental D_1 and D_2 values [nis] as the size of the active space increases. For smaller values of R the PECs computed using different active space configurations differ by nearly the same overall energy offset as observed in the asymptotic limit. As a result, all calculations are performed using an nsnp orbital active space and offset in the asymptotic limit of $R = 100\,\mathring{A}$ to the NIST D_1 and D_2 energies [nis]. Specifically the $X^2\Sigma^+_{1/2}$ PECs are

Table 5. Various active space configurations labeled by the rubidium atomic orbitals for Rb + He at $R = 100\,\mathring{A}$. The first two configurations include a Davidson-Silver correction, and the largest configuration includes a renormalized Davidson correctionDavidson and Silver [1977]. Energies are in cm^{-1}. The empirical NIST values for the $^2P_{1/2}$ and $^2P_{3/2}$ atomic excitation energies of Rb are $12\,579\,cm^{-1}$ and $12\,815\,cm^{-1}$, respectivelynis. The Rb spin-orbit splitting, $\Delta = 236\,cm^{-1}$.

Configuration	$^2P_{1/2}$	$^2P_{3/2}$	Δ
5s5p	12 555	12 754	199
5s5p6s6p4d	12 555	12 764	209
5s5p6s6p4d7s7p5d	12 591	12 804	213

offset to zero, the $A^2\Pi_{1/2}$ PECs are offset to the $^2P_{1/2}$ energy, and the $A^2\Pi_{3/2}$ and $B^2\Sigma^+_{1/2}$ PECs are offset to the $^2P_{3/2}$ energy.

Upon completion of the SOCI calculation an *a posteriori* Davidson-Silver correction is performed to ameliorate size consistency error [Davidson and Silver, 1977]. For these calculations we did not correct for basis set superposition error (BSSE). As a result we expect our calculations to somewhat over estimate well depths. The counterpoise (CP) correction [Boys and Bernardi, 1970] is often used to address BSSE. However, the CP technique tends to over correct for BSSE and yield an under estimate of the well depth [Iwata, 2011]. It would appear that the best way to control for BSSE is to explore a hierarchy of basis sets to calculate energies with and without the CP correction [Helgaker et al., 2000]. For a suitably chosen hierarchy, the CP corrected and uncorrected energies will converge. In this case an extrapolation to the complete basis set limit is reasonable and will also eliminate basis set incompleteness error (BSIE). For many systems BSIE is significantly larger than BSSE [Balabin, 2010] and is likely to be the largest source of error in our calculations. Both BSSE and BSIE occur in the ground and excited curves, and the degree to which they are present can be estimated by comparison with experiment and other theoretical calculations.

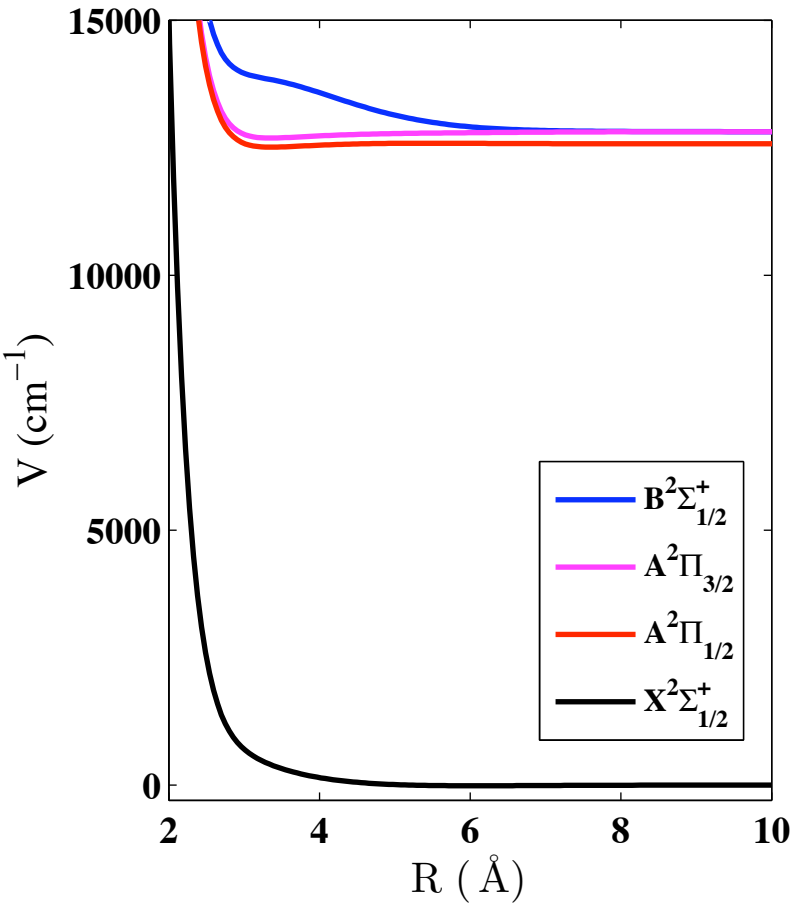

Figure 15. The $X^2\Sigma^+_{1/2}$, $A^2\Pi_{1/2}$, $A^2\Pi_{3/2}$, and $B^2\Sigma^+_{1/2}$ curves of Rb + Ne. The asymptotic limit of the $X^2\Sigma^+_{1/2}$ curve is at $0\,cm^{-1}$. The excited curves are offset in the asymptotic limit to the NIST D1 (for $A^2\Pi_{1/2}$) and D2 (for $A^2\Pi_{3/2}$ and $B^2\Sigma^+_{1/2}$) values of Rbnis.

3.2.2 Results and Discussion.

The $X^2\Sigma^+_{1/2}$, $A^2\Pi_{1/2}$, $A^2\Pi_{3/2}$, and $B^2\Sigma^+_{1/2}$ PECs for Rb + Ne are shown in Figure 15. In the separated atom limit the $X^2\Sigma^+_{1/2}$ curve corresponds to the Rb $^2S_{1/2}$ ground state energy level, the $A^2\Pi_{1/2}$ curve corresponds to the Rb $^2P_{1/2}$ energy level, and the $A^2\Pi_{3/2}$ and $B^2\Sigma^+_{1/2}$ curves correspond to the Rb $^2P_{3/2}$ energy level. The $X^2\Sigma^+_{1/2}$ curve is mostly repulsive, with a shallow $14.4\,cm^{-1}$ well in the region of $R \approx 6\,\mathring{A}$. The $B^2\Sigma^+_{1/2}$ curve also exhibits a shallow $0.7\,cm^{-1}$ well further out toward the asymptotic limit in the range of $R \approx 9\,\mathring{A}$, as well as a shoulder on the repulsive wall at smaller values of R.

An expanded view of the excited state curves of Rb + Ne is shown in Figure 16 to exemplify details common to all $M + Ng$ pairs. Moving in the direction of decreasing R from the asymptotic limit, the $A^2\Pi_{3/2}$ and the $B^2\Sigma^+_{1/2}$ curves diverge at approximately $R \approx 8.5\,\mathring{A}$. The $A^2\Pi_{3/2}$ curve decreases in energy below the asymptotic $^2P_{3/2}$ value and roughly follows the $A^2\Pi_{1/2}$ curve. These two $A^2\Pi$ curves exhibit relatively large well depths compared to the shallower ground state $X^2\Sigma^+_{1/2}$ well. Moreover, the minima of the two $A^2\Pi$ wells occur at approximately the same value of $R = r_{min} = r_{min1}$. In addition to exhibiting a minimum at $R = r_{min1}$ the $A^2\Pi_{1/2}$ curve also exhibits a local minimum of depth D_{min2} at $R = r_{min2}$ which is separated from the deep well by a barrier of height V_b at $R = r_b$.

The equilibrium positions of all wells and barriers for the PECs are tabulated in Table 6 and the well depths and barrier heights are tabulated in Table 7. Where possible these are compared to experiment and other theoretical calculations. The equilibrium and barrier positions in Table 6 are all in agreement to within a few percent, and most values are in agreement to within $1 - 2\,\%$. The well depths listed in Table 7 are in greatest disagreement with the DFT based calculations [Zbiri and Daul, 2004, Goll et al., 2006]. Excluding the DFT results, the well depths are in agreement to within about $20 - 30\,\%$ for the $X^2\Sigma^+_{1/2}$ curve and to within $5 - 10\,\%$ for the $A^2\Pi_{1/2}$ and $A^2\Pi_{3/2}$ curves. The larger relative error in the ground state well depths is primarily due to their smaller values.

The PECs for all $M + Ng$ combinations are presented in Figures 17 through 20 and grouped by molecular term symbol. Figure 17 displays all $X^2\Sigma^+_{1/2}$ PECs, Figure 18 all $B^2\Sigma^+_{1/2}$ PECs, Figure 19 all $A^2\Pi_{1/2}$ PECs, and Figure 20 all $A^2\Pi_{3/2}$ PECs. In Figsures 17 through 20 the PECs associated with one alkali-metal are artificially offset from those of another for clarity. Potassium curves are asymptotically set to $0\,cm^{-1}$, rubidium to $250\,cm^{-1}$, and cesium to $500\,cm^{-1}$.

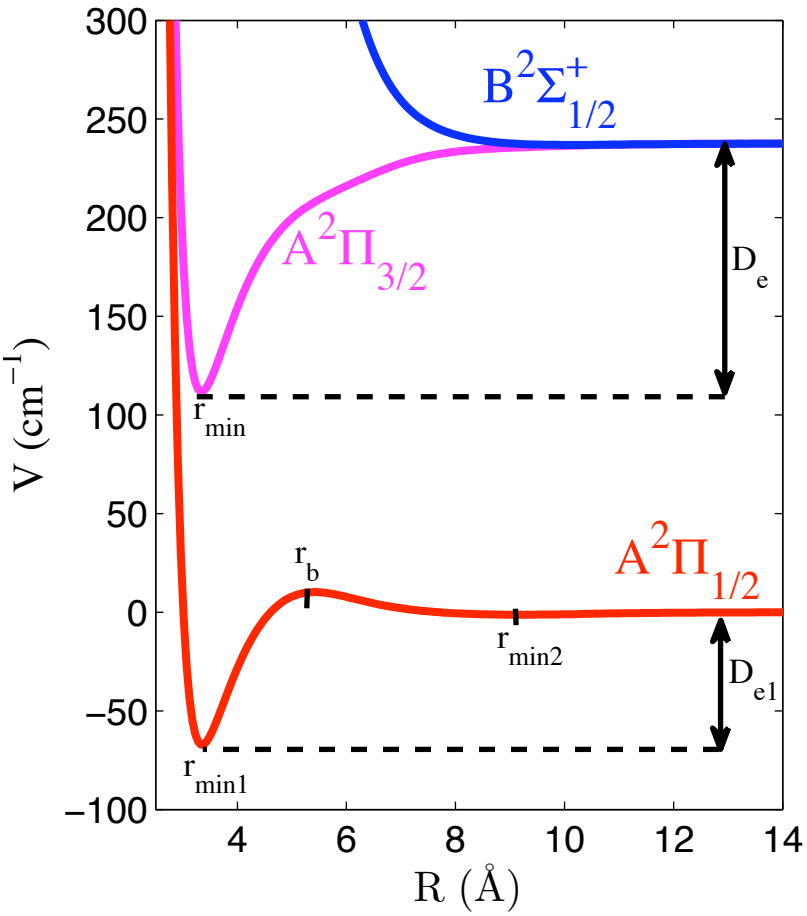

Figure 16. The $A^2\Pi_{1/2}$, $A^2\Pi_{3/2}$, and $B^2\Sigma^+_{1/2}$ curves of Rb + Ne. The asymptotic limit of the $A^2\Pi_{1/2}$ curve is offset to $0\,cm^{-1}$, and the asymptotic limit of the $A^2\Pi_{3/2}$ and $B^2\Sigma^+_{1/2}$ curves are offset to the NIST Rb spin-orbit splitting energynis. The $A^2\Pi_{3/2}$ curves for all $M+Ng$ combinations have a single well at r_{min}, while most $A^2\Pi_{1/2}$ have two minima, one at r_{min1}, and the other at r_{min2}, separated by a barrier at r_b. The $B^2\Sigma^+_{1/2}$ curve also exhibits a shallow well not visible on the scale of this plot.

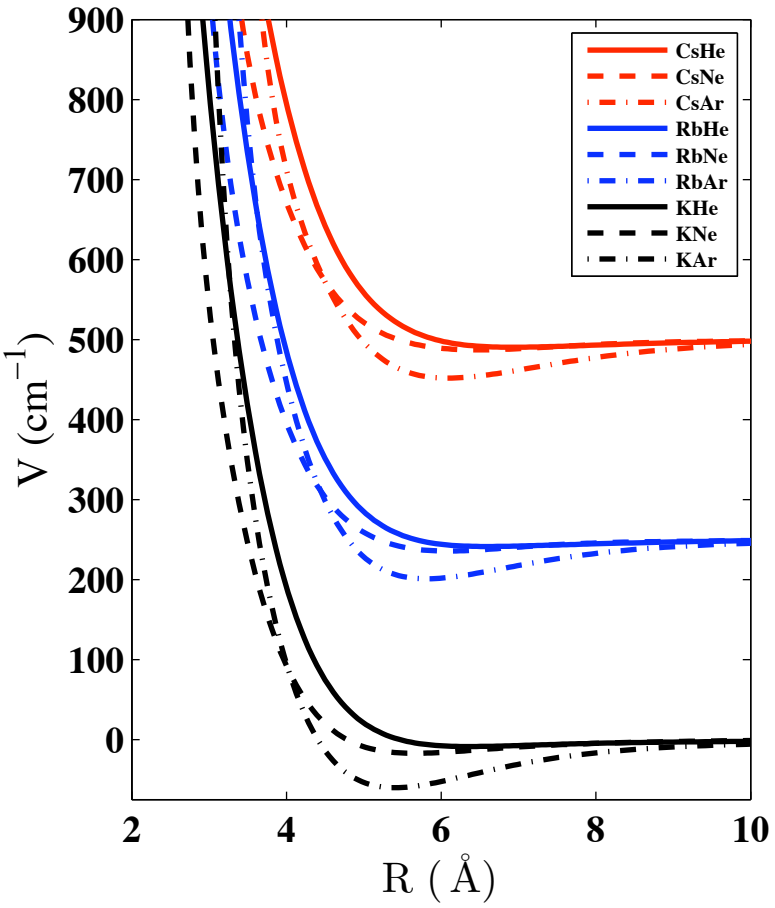

Figure 17. The $X^2\Sigma^+_{1/2}$ curves for all $M + Ng$ pairs. For clarity, the curves associated with one alkali atom are asymptotically offset from those of the other alkali atoms. The three K+Ng pairs are asymptotically set to zero, while the Rb+Ng are offset to $250\,cm^{-1}$ and Cs+Ng are offset to $500\,cm^{-1}$.

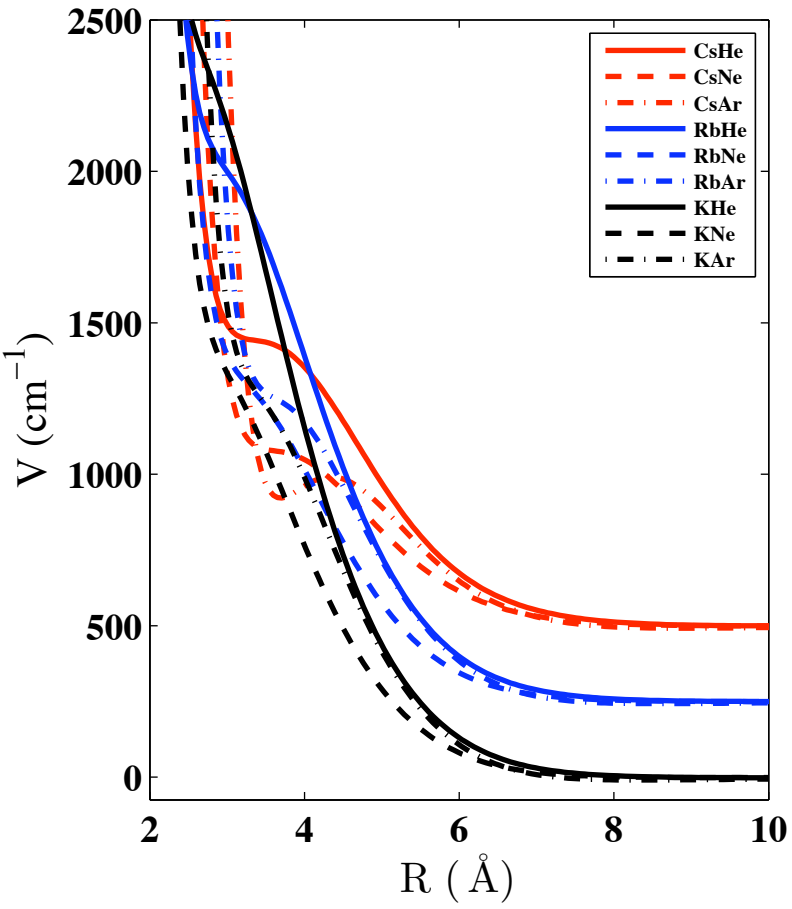

Figure 18. The $B^2\Sigma^+_{1/2}$ curves for all $M + Ng$ pairs. Offsets are the same as in Figure 17.

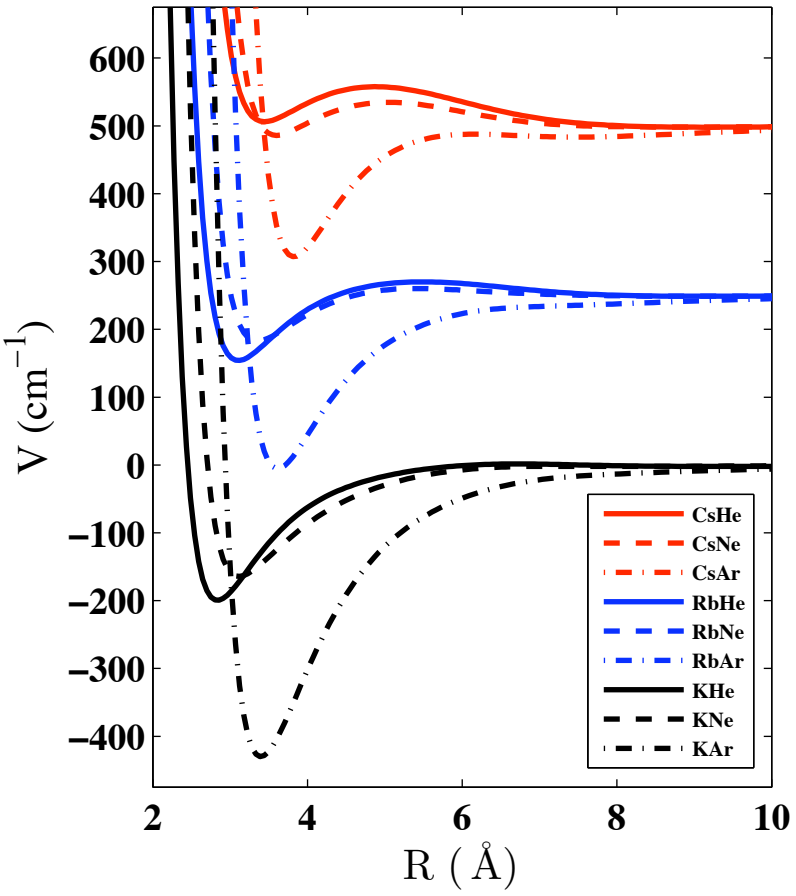

Figure 19. The $A^2\Pi_{1/2}$ curves for all $M + Ng$ pairs. Offsets are the same as in Figure 17.

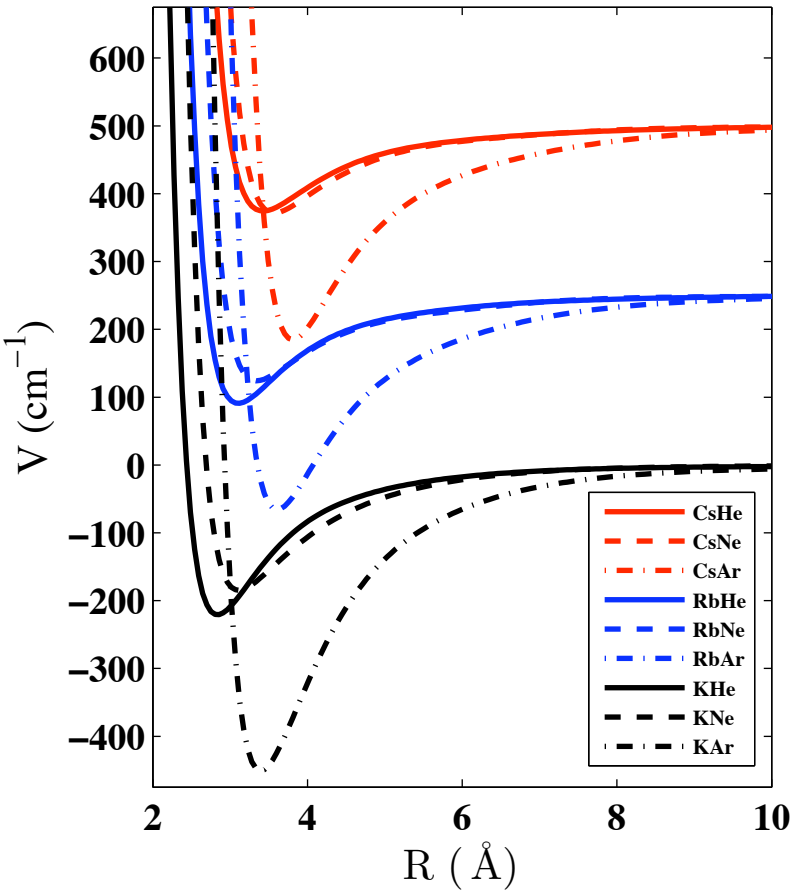

Figure 20. The $A^2\Pi_{3/2}$ curves for all $M + Ng$ pairs. Offsets are the same as in Figure 17.

Table 6. Equilibrium and barrier positions (Å), as defined in Figure 16, for all $M + Ng$ curves. The pseudopotential calculations by Pascale [1983] and the DFT calculations by Zbiri and Daul [2004] report energies for the $A^2\Pi$ curve and are listed under both the $A^2\Pi_{1/2}$ and $A^2\Pi_{3/2}$ columns for ease of comparison.

M+Ng	$X^2\Sigma^+_{1/2}$	$A^2\Pi_{1/2}$			$A^2\Pi_{3/2}$	$B^2\Sigma^+_{1/2}$
	r_{min}	r_{min1}	r_b	r_{min2}	r_{min}	r_{min}
KHe	6.35	2.86	6.72	9.42	2.86	10.27
theo[1]	-	2.8	-	-	2.8	-
theo[2]	-	2.8	-	-	2.8	-
KNe	5.66	3.12	7.20	8.15	3.12	9.42
theo[3]	5.97	-	-	-	-	-
KAr	5.40	3.39	-	-	3.39	8.36
exp[4]	5.3	-	-	-	-	-
exp[5]	5.404(5)	3.37(3)	-	-	3.34(3)	7.10
theo[6]	5.13	3.41	-	-	3.41	-
theo[3]	5.322	-	-	-	-	-
RbHe	6.61	3.12	5.50	9.10	3.12	10.48
theo[7]	-	3.21	5.3	-	3.21	-
theo[1]	-	3.22	-	-	3.22	-
theo[2]	-	3.3	-	-	3.3	-
RbNe	6.09	3.33	5.40	9.21	3.33	10.16
theo[3]	6.19	-	-	-	-	-
RbAr	5.82	3.60	-	-	3.60	8.57
theo[3]	5.45	-	-	-	-	-
CsHe	6.93	3.44	4.87	9.21	3.44	10.58
theo[1]	-	3.38	-	-	3.38	-
theo[2]	-	3.49	-	-	3.49	-
CsNe	6.46	3.60	5.03	8.78	3.55	10.37
theo[3]	6.46	-	-	-	-	-
CsAr	6.09	3.81	6.14	7.46	3.81	8.89
exp[8]	5.50	-	-	-	-	-
theo[9]	5.59	-	-	-	-	-
theo[3]	5.59	-	-	-	-	-

[1]Zbiri and Daul [2004]
[2]Pascale [1983]
[3]Goll et al. [2006]
[4]Figl et al. [2004]
[5]Bokelmann and Zimmermann [1996]
[6]Rhouma et al. [2002]
[7]Hirano et al. [2003]
[8]Buck and Pauly [1968]
[9]Merritt et al. [2009]

Table 7. Well depths and barrier heights (cm^{-1}), as defined in Figure 16, for all $M+Ng$ curves. Note that a negative value for V_b corresponds to a local maximum that is less than the asymptotic $^2P_{1/2}$ atomic energy. The pseudopotential calculations by Pascale [1983] and the DFT calculations by Zbiri and Daul [2004] report energies for the $A^2\Pi$ curve and are listed under both the $A^2\Pi_{1/2}$ and $A^2\Pi_{3/2}$ columns for ease of comparison.

M+Ng	$X^2\Sigma^+_{1/2}$	$A^2\Pi_{1/2}$			$A^2\Pi_{3/2}$	$B^2\Sigma^+_{1/2}$
	D_e	D_{e1}	V_b	D_{e2}	D_e	D_e
KHe	-8.7	-199.3	1.6	-2.1	-220.6	-1.8
theo[1]	-	-480	-	-	-480	-
theo[2]	-	-245	-	-	-245	-
KNe	-17.1	-164.3	-1.9	-2.2	-184.8	-1.2
theo[3]	-5.6	-	-	-	-	-
KAr	-60.2	-429.9	-	-	-450.8	-9.5
exp[4]	-40.65	-	-	-	-	-
exp[5]	-40.1(6)	-405(15)	-	-	-427(15)	-23
theo[6]	-59	-421	-	-	-440	-
theo[3]	-41.7	-	-	-	-	-
RbHe	-8.7	-95.9	20.0	-1.2	-159.1	-0.3
theo[7]	-	-102.1	26.5	-	-176.8	-
theo[1]	-	-276	-	-	-276	-
theo[2]	-	-134	-	-	-134	-
RbNe	-14.4	-67.1	10.2	-1.2	-125.8	-0.7
theo[3]	-5.0	-	-	-	-	-
RbAr	-49.0	-255.2	-	-	-315.7	-7.3
theo[3]	-38.6	-	-	-	-	-
CsHe	-9.6	6.3	57.7	-1.9	-125.5	-0.6
theo[1]	-	-230	-	-	-230	-
theo[2]	-	-112	-	-	-112	-
CsNe	-12.9	-14.1	34.7	-1.7	-128.4	-0.7
theo[3]	-4.7	-	-	-	-	-
CsAr	-48.3	-192.8	-12.3	-16.6	-315.3	-8.1
exp[8]	-45	-	-	-	-	-
theo[9]	-39.6	-	-	-	-	-
theo[3]	-39.6	-	-	-	-	-

[1]Zbiri and Daul [2004]
[2]Pascale [1983]
[3]Goll et al. [2006]
[4]Figl et al. [2004]
[5]Bokelmann and Zimmermann [1996]
[6]Rhouma et al. [2002]
[7]Hirano et al. [2003]
[8]Buck and Pauly [1968]
[9]Merritt et al. [2009]

The $X^2\Sigma^+_{1/2}$ ground curves shown in Figure 17 all exhibit shallow wells with minima in the range of $R \approx 5 - 7\,\mathring{A}$. The depths of these wells increase as the mass of the noble-gas atom in the $M + Ng$ pair increases. Also, for a given noble-gas atom, the well depths are similar regardless of the alkali-metal atom with which it is paired. An exception to this trend occurs for K + Ar where the $X^2\Sigma^+_{1/2}$ well is deeper by a factor of one and a half when compared to the Rb + Ar and Cs + Ar $X^2\Sigma^+_{1/2}$ wells. The equilibrium position for these wells increases as the mass of the alkali-metal atom increases. However for a given alkali-metal atom, the equilibrium position of these wells decreases as the mass of the noble-gas atom increases. This decrease in equilibrium position may be attributed to the increase in attractive dispersion force as the number of noble-gas atom electrons increases [Stone, 1996]. A similar trend in the equilibrium position of the $X^2\Sigma^+_{1/2}$ ground curves was also observed by Goll et al. [2006].

The excited $B^2\Sigma^+_{1/2}$ curves are shown in Figure 18. They each exhibit a shoulder at values of $R = 3 - 5\,\mathring{A}$ and a very shallow well at values of $R = 7 - 9\,\mathring{A}$. These shallow $B^2\Sigma^+_{1/2}$ wells do not appear on the scale of the plot in Figure 18. An expanded view of this $B^2\Sigma^+_{1/2}$ well for Cs + Ar is shown in Figure 21, where the well appears at approximately the same value of R for which the $B^2\Sigma^+_{1/2}$ and $A^2\Pi_{3/2}$ curves diverge. The $B^2\Sigma^+_{1/2}$ shoulders occur highest up on the repulsive wall for potassium, followed by rubidium and then cesium. For a given alkali-metal atom, the shoulders are most pronounced for argon and lowest in energy, and least pronounced for helium and highest in energy. The neon shoulders are very similar to argon and occur at roughly the same energies. For Cs + Ar this feature is so pronounced that the repulsive wall actually stops rising and decreases, forming a local minimum, before becoming repulsive again. These shoulders have been attributed by Pascale and Vandeplanque [1974] to mixing with higher excited states that correlate in the dissociated atom limit

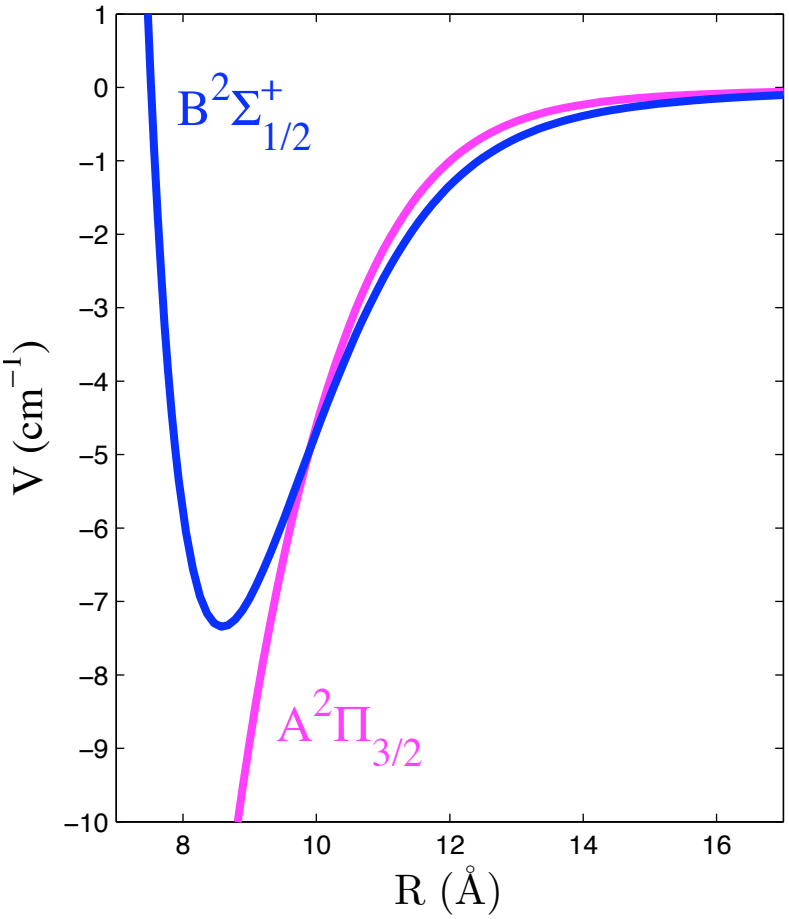

Figure 21. An expanded view of the $B^2\Sigma^+_{1/2}$ well for Cs + Ar. The well occurs where the $B^2\Sigma^+_{1/2}$ and $A^2\Pi_{3/2}$ PECs diverge. Similar behavior is observed for all $M+Ng$ pairs.

to the $(n-1)^2D_{3/2}$ and $(n-1)^2D_{5/2}$ alkali-metal manifolds [Ehara and Nakatsuji, 1995].

In Figure 19 each of the $A^2\Pi_{1/2}$ curves are qualitatively similar but demonstrate considerable quantitative variation. For a given alkali-metal atom, the well depths D_{e1} are the deepest for Ar, shallowest for Ne, with He being somewhat deeper than Ne. An exception to this ordering is Cs where the He well is shallower than the Ne well. The equilibrium position $R = r_{min1}$ of the $A^2\Pi_{1/2}$ wells increases as either the alkali-metal atom or noble-gas atom mass increases. Since the $A^2\Pi_{1/2}$ minima lie closer to the repulsive wall than the $X^2\Sigma^+_{1/2}$ wells, Coulomb and exchange repulsion

dominate, and polarization is less important. As a result the equilibrium positions increase with the atomic number of the noble-gas atom rather than decrease as they do for the $X^2\Sigma^+_{1/2}$ curves. It is interesting to note that the $A^2\Pi_{1/2}$ well depths are linearly correlated to the difference of the average ionization energies of M and Ng from their first excited state manifolds. This suggests that there is a simple model for the $A^2\Pi$ well depth similar to charge-resonance models used to describe excimer luminescence [Shirai et al., 2011, Nowakowska et al., 1997, Chow and Johansson, 1995].

The barrier heights, V_b, of the $A^2\Pi_{1/2}$ curves can be used together with the well depths D_{e2} to compute a relative barrier height $V_b - D_{e2}$. This relative barrier height increases as the mass of the alkali-metal atom increases. For a given alkali-metal the relative barrier height also increases as the mass of the noble-gas atom decreases. These barriers at $R = r_b$ are accompanied by shallow wells at $R = r_{min2}$ and, together with the shallow wells exhibited by the $B^2\Sigma^+_{1/2}$ curves, are associated with radial derivative coupling between the $A^2\Pi_{1/2}$ and $B^2\Sigma^+_{1/2}$ states [Mies, 1973]. Note that a negative value for V_b corresponds to a local maximum that is less than the asymptotic $^2P_{1/2}$ atomic energy. Also, note that K + Ar and Rb+Ar are the only $M + Ng$ combinations whose $A^2\Pi_{1/2}$ curves do not exhibit a barrier.

The $A^2\Pi_{3/2}$ curves shown in Figure 20 are similar to the $A^2\Pi_{1/2}$ curves. The $A^2\Pi_{3/2}$ well depths, D_e, follow the same trend as the $A^2\Pi_{1/2}$ well depths, D_{e1}, with regard to the mass of the alkali-metal and noble-gas atoms. The $A^2\Pi_{3/2}$ curves differ from the $A^2\Pi_{1/2}$ curves in that D_e is greater than D_{e1} for all nine $M + Ng$ pairs, and the $A^2\Pi_{3/2}$ curves exhibit no secondary minima. The absence of secondary minima occurs because there is no radial derivative coupling between the $A^2\Pi_{3/2}$ states and other states nearby in energy. It is interesting to note that the equilibrium positions of the wells in both the $A^2\Pi_{1/2}$ and $A^2\Pi_{3/2}$ curves are nearly equal to each other and

Table 8. Rb + He $A^2\Pi_{3/2}$ vibrational energy level differences (in cm^{-1}) for $\Delta\nu = 1$.

ΔE	This Work	Exp[1]	Theory[2]
$E_1 - E_0$	55.47	65.8(3)	60.5
$E_2 - E_1$	33.10	43.7(2)	39.2
$E_3 - E_2$	17.72	23.2(7)	18.2
$E_4 - E_3$	9.57	8.8(6)	11.9
$E_5 - E_4$	4.47	-	7.9

[1]Mudrich et al. [2008]
[2]Hirano et al. [2003]

to the minimum of the $A^2\Pi$ curve obtained when spin-orbit coupling is neglected.

An analysis of the vibrational energy levels (VELs) for the $M + Ng$ systems show that all $X^2\Sigma^+_{1/2}$, $A^2\Pi_{1/2}$, and $A^2\Pi_{3/2}$ curves exhibit weakly bound vibrational states. The VELs are computed with a finite basis representation of the vibrational Hamiltonian, where the rotational degree of freedom is ignored ($J = 0$). Vibrational spectra have been observed for the $A^2\Pi_{3/2}$ electronic state of Rb + He [Mudrich et al., 2008], the ground $X^2\Sigma^+_{1/2}$ and excited $A^2\Pi$ electronic states for K + Ar [Bokelmann and Zimmermann, 1996], and the $A^2\Pi_{1/2}$ and $A^2\Pi_{3/2}$ curves of Cs + He [Enomoto et al., 2002]. Hirano et al. [2003] have computed VELs for the $A^2\Pi_{3/2}$ curve of Rb + He. The difference between VELs for $\Delta\nu = 1$ are tabulated in Table 8 for Rb + He and Table 9 for K + Ar, while the absolute VELs measured from dissociation are tabulated in Table 10 for Cs + He.

As listed in Table 8, the computational results predict the presence of six VELs for the Rb + He $A^2\Pi_{3/2}$ curve, however only five levels are observed. The experimental differences listed in this table were fit by Mudrich et al. [2008] to a Morse potential. The Morse fit is compared with the $A^2\Pi_{3/2}$ curve in Figure 22. The Morse potential exhibits a deeper well, while our $A^2\Pi_{3/2}$ curve approaches equilibrium more slowly. The VELs are included in Figure 22 for comparison purposes.

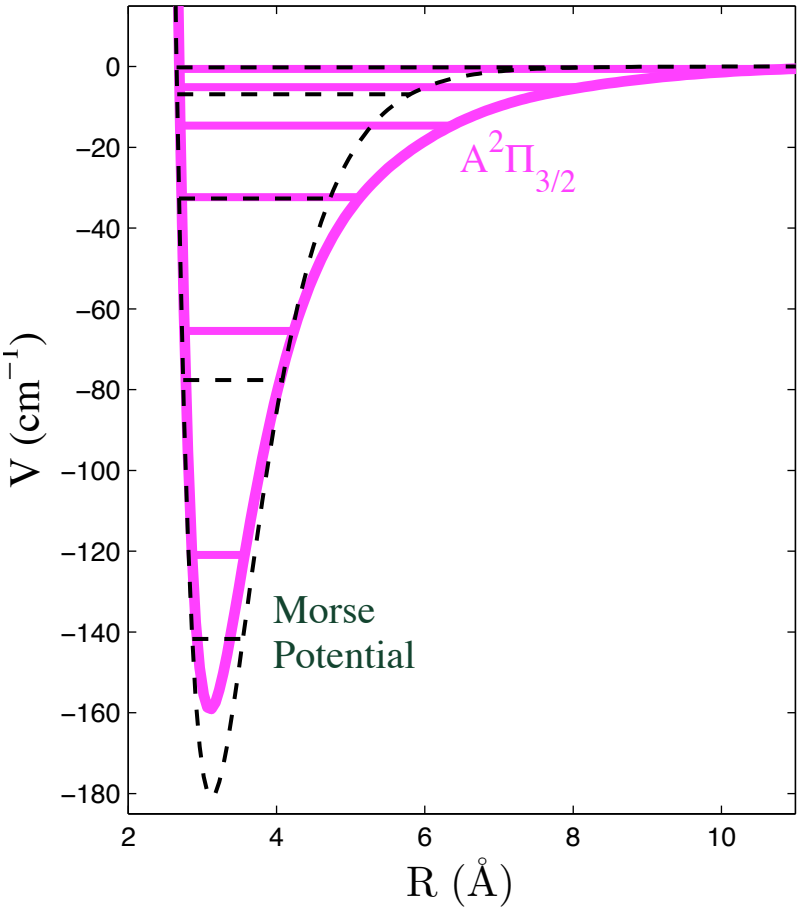

Figure 22. The Rb + He $A^2\Pi_{3/2}$ curve (solid) and a Morse potential fit (dashed) to the experimental vibrational energy differences listed in Table 8Mudrich et al. [2008]. The curves are offset to share a common asymptotic limit, and vibrational energy levels are included for comparison.

Table 9. K + Ar $X^2\Sigma^+$ and $A^2\Pi$ vibrational energy level differences in cm^{-1} for $\Delta\nu = 1$.

ΔE	This Work $X^2\Sigma^+_{1/2}$	Exp[1] $X^2\Sigma$	This Work $A^2\Pi_{3/2}$	This Work $A^2\Pi_{1/2}$	Exp[1] $A^2\Pi$
$E_1 - E_0$	9.55	8.77			
$E_2 - E_1$	8.69	7.53			
$E_3 - E_2$	7.77	6.25			
$E_7 - E_6$			27.24	27.41	26.45
$E_8 - E_7$			24.07	24.27	22.86
$E_9 - E_8$			21.11	21.35	19.57
$E_{10} - E_9$			18.38	18.69	16.55
$E_{11} - E_{10}$			15.91	16.31	13.63

[1]Bokelmann and Zimmermann [1996]

Our calculations of the K + Ar $X^2\Sigma^+_{1/2}$ VELs indicate that there are twelve bound vibrational states. The first three VEL differences for $\Delta\nu = 1$ are listed in table 9. These calculations also indicate that the K + Ar $A^2\Pi_{1/2}$ curve has twenty-two bound vibrational states, and the $A^2\Pi_{3/2}$ curve has twenty-four. Several $\Delta\nu = 1$ VEL differences for the $A^2\Pi_{1/2}$ and $A^2\Pi_{3/2}$ curves are also listed in table 9 where ν ranges from six to ten. Theoretical $\Delta\nu = 1$ values are listed in table 9 only if there is a corresponding experimental value for comparison. The VELs predicted for the $A^2\Pi_{1/2}$ and $A^2\Pi_{3/2}$ curves are nearly the same, being most similar for the lower VELs. This reflects the similarity between the $A^2\Pi_{1/2}$ and $A^2\Pi_{3/2}$ curves that occurs because the $A^2\Pi_{1/2}$ curve for K + Ar has only one local minimum for all R. The experimental results tabulate $\Delta\nu = 1$ VEL differences for the $A^2\Pi$ level.

Experimental and calculated VELs are listed in table 10 for the $A^2\Pi_{1/2}$ and $A^2\Pi_{3/2}$ curves of Cs + He. As seen in Fig. 19, the bottom of the Cs + He $A^2\Pi_{1/2}$ well lies above its asymptotic energy. However calculations predict that this well does support one quasi-bound VEL which has also been experimentally observedEnomoto et al. [2002]. The $A^2\Pi_{3/2}$ curve is predicted to support six bound VELs as compared to five

Table 10. Cs + He $A^2\Pi_{1/2}$ and $A^2\Pi_{3/2}$ vibrational energy levels in cm^{-1} relative to the Cs $^2P_{1/2}$ and $^2P_{3/2}$ levels, respectively. The $A^2\Pi_{1/2}$ curve exhibits a single quasi bound state with a positive VEL.

Electronic State	Vibrational State	This Work	Exp[1]
$A^2\Pi_{1/2}$	$\nu = 0$	50.0	48.35
$A^2\Pi_{3/2}$	$\nu = 0$	-95.0	-84.89
	$\nu = 1$	-51.1	-45.09
	$\nu = 2$	-25.1	-19.79
	$\nu = 3$	-11.6	-5.90
	$\nu = 4$	-4.0	-0.51
	$\nu = 5$	-0.3	-

[1]Enomoto et al. [2002]

experimentally observed VELs. Note that predictions for the VELs of $A^2\Pi_{1/2}$ and $A^2\Pi_{3/2}$ curves of K + Ar are very similar, while predictions for the same two curves of Cs + He are significantly different. This reflects the trend for the relative barrier height $V_b - D_{e2}$ to increase as the mass of the alkali-metal atom increases and the mass of the noble-gas decreases. As the relative barrier height increases, the $A^2\Pi_{1/2}$ and $A^2\Pi_{3/2}$ curves become more dissimilar causing a greater disparity between the corresponding VELs.

The PECs of $M + Ng$ pairs can be used to predict alkali-metal atom line shapes that are broadened by collisions with noble-gas atomsAllard and Kielkopf [1982], Szudy and Baylis [1996]. In the semi-classical Anderson-Talman model of line broadening, the alkali-metal atom D_1 and D_2 line shapes are governed in part by DPs, ΔV, given by the difference between PECs. In the case of the D_1 line, the $A^2\Pi_{1/2}$ curve correlates with the $^2P_{1/2}$ atomic energy level, and the line shape is determined by the single DP, $\Delta V = A^2\Pi_{1/2} - X^2\Sigma^+_{1/2}$, when non-adiabatic effects are ignored. For the D_2 line, both the $A^2\Pi_{3/2}$ and the $B^2\Sigma^+_{1/2}$ curves correlate with the $^2P_{3/2}$ atomic energy level, and the line shape is therefore determined by two DP, $\Delta V = A^2\Pi_{3/2} - X^2\Sigma^+_{1/2}$

and $\Delta V = B^2\Sigma^+_{1/2} - X^2\Sigma^+_{1/2}$. When non-adiabatic effects are included, all four PECs are expected to contribute to both the D_1 and D_2 line broadening.

To better understand the general shape of the DPs, four plots for Cs + Ar are shown in Fig. 23 using a common R axis. The first plot at the top of the figure shows the excited $A^2\Pi_{1/2}$, $A^2\Pi_{3/2}$, and $B^2\Sigma^+_{1/2}$ curves, while the second plot from the top of the figure shows the ground $X^2\Sigma^+_{1/2}$ curve. The PECs in the first plot use the same zero as the second plot and, as mentioned before, are offset in the asymptotic limit $R = 100\,\mathring{A}$ to the alkali-metal atom D_1 and D_2 NIST valuesnis. The third plot from the top shows the $\Delta V = A^2\Pi_{1/2} - X^2\Sigma^+_{1/2}$, $\Delta V = A^2\Pi_{3/2} - X^2\Sigma^+_{1/2}$, and $\Delta V = B^2\Sigma^+_{1/2} - X^2\Sigma^+_{1/2}$ DPs in units of nm. Finally, the transition dipole moments $| < X^2\Sigma^+_{1/2}|\mathrm{D}|A^2\Pi_{1/2} > |$, $| < X^2\Sigma^+_{1/2}|\mathrm{D}|A^2\Pi_{3/2} > |$, and $| < X^2\Sigma^+_{1/2}|\mathrm{D}|B^2\Sigma^+_{1/2} > |$ are shown in the fourth plot at the bottom of the figure. Similar to the PECs, the dipole matrix elements are offset using the NIST Einstein A coefficientsnis.

DPs ΔV can be used to compute collisionally broadened line shapes, $I(\omega)$, in the quasistatic limitSzudy and Baylis [1975], Allard and Kielkopf [1982], Szudy and Baylis [1996] where,

$$\begin{aligned} I(\omega) \;\propto\; & \sum_c R_c^2 |\mathrm{D}(R_c)|^2 \left| \frac{\mathrm{d}(\Delta V)}{\mathrm{d}R} \right|^{-1}_{R_c} \\ & \times n_{Ng} \exp\left(-\frac{X^2\Sigma^+_{1/2}(R_c)}{k_B T} \right). \end{aligned} \tag{63}$$

In Equation 63, $\mathrm{D}(R_c)$ is the transition dipole matrix element, n_{Ng} is the concentration of the noble-gas, k_B is Boltzmann's constant, T is the absolute temperature, $X^2\Sigma^+_{1/2}(R_c)$ is the ground state PEC, and $R_c(\omega)$ are Condon points given by the solutions to the equation $\Delta V(R_c) = \hbar\omega$Szudy and Baylis [1996]. Here it is assumed that the concentration of the alkali-metal gas is low relative to n_{Ng}, and the line broadening occurs only as a result of $M + Ng$ collisions.

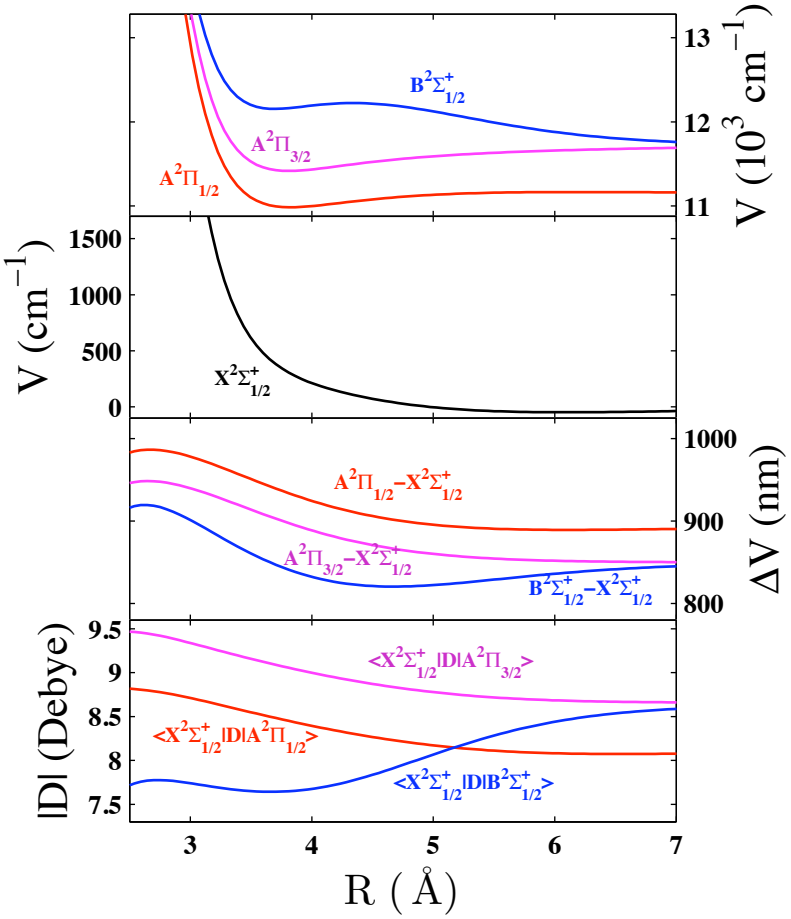

Figure 23. The Cs + Ar $B^2\Sigma^+_{1/2}$, $A^2\Pi_{1/2}$, and $A^2\Pi_{3/2}$ curves are shown in the first plot, and the second plot shows the $X^2\Sigma^+_{1/2}$ curve. The PECs use the same zero as the second plot and are offset in the asymptotic limit to the alkali D1 and D2 valuesnis. The third plot shows potential differences and the fourth plot shows transition dipole matrix elements.

For a given value of ω, the Boltzmann factor in Equation (63) governs the probability for which a given $M + Ng$ pair will be at a separation distance $R_c(\omega)$. The product of the Boltzmann factor and n_{Ng} defines an effective concentration, $n_{eff}(R_c)$, and for Cs + Ar at $T = 400K$ this corresponds to $n_{eff}(3.5\,\mathring{A}) \approx 0.1 n_0$. Because the Boltzmann factor drops off rapidly at lower values of R_c, this term dominates the expression for $I(\omega)$ for values of $R_c < 3.5$. For a given value of ω for which $R_c(\omega) > 3.5$ the intensity will depend on the value of the dipole matrix element and the derivative of the DP. In Fig. 23 the Cs + Ar dipole matrix elements vary on the order of $5 - 10\%$ for R ranging from $R = 3.5\mathring{A}$ to the asymptotic limit. The DPs for Cs + Ar in Fig. 23 exhibit extrema that correspond to singularities in $I(\omega)$ given by Equation (63). The $B^2\Sigma^+_{1/2} - X^2\Sigma^+_{1/2}$ DP exhibits three extrema, one in the asymptotic limit, one at $R \approx 4.5$, and one at $R \approx 2.6$. The extremum in the asymptotic limit corresponds to the D_2 atomic line core, and the extremum at $R \approx 4.5$ corresponds to a satellite blue shifted from line core. The extremum at $R \approx 2.6$ corresponds to a red shifted satellite. However it is allowed by the Boltzmann distribution only at sufficiently high temperatures. The $A^2\Pi_{1/2} - X^2\Sigma^+_{1/2}$ and $A^2\Pi_{3/2} - X^2\Sigma^+_{1/2}$ DPs also exhibit extrema in the asymptotic limit corresponding to the D_1 and D_2 line cores, respectively, and extrema at small values of R corresponding to red shifted satellites that are suppressed by the Boltzmann distribution.

Predictions for the positions of blue shifted satellites of the alkali-metal atom D_2 transitions are reported in table 11 along with comparisons to experiment. The predicted satellite peaks are all shifted in the blue direction from the observed satellite peaks by approximately $12 - 20\,nm$. The predicted satellite peaks occur as a result of the shoulder exhibited by the $B^2\Sigma^+_{1/2}$ curves. For the Stuttgart basis set used in these calculations, it is likely that this shoulder is not accurately computed, which gives rise to the discrepancy between predicted and observed blue satellites. However, our

calculations do capture the trends observed in the experimental data. As seen in table 11, the experimentally observed satellite peak for Cs + He at $827\,nm$ is significantly more blue shifted than the peaks for Cs + Ne and Cs + Ar at $837\,nm$ and $838\,nm$, respectively. Our theoretical predictions mirror this pattern where, for a given alkali-metal atom, the blue peaks for neon and argon are relatively close in wavelength and the helium peak is significantly more blue shifted. These peaks correspond to the $B^2\Sigma^+_{1/2}$ shoulder that, as seen in Fig. 18, occurs highest in energy for M + He and at lower but similar energies for M + Ne and M + Ar. For rubidium the experimental data identifies neon and argon satellites at $752\,nm$ and $754\,nm$, respectively, while no experimental data could be found for helium. It is possible to make a prediction for the Rb + He satellite by computing the difference between the calculated Rb + Ne and Rb + He satellites in table 11 and subtracting it from the experimental Rb + Ne satellite. This procedure yields $733\,nm$ for the Rb + He satellite peak. The same procedure applied to cesium yields $825\,nm$ for the Cs + He satellite compared to the experimental value of $827\,nm$. For potassium no experimental data could be found. However, the surfaces suggest that the K + He satellite will be significantly more blue shifted than the K + Ne and K + Ar satellites. A second trend in table 11 is observed where, for a given noble-gas atom, the satellite is more blue shifted as the mass of the alkali-metal atom decreases. This corresponds to $B^2\Sigma^+_{1/2}$ shoulders in Fig. 18 which occur highest in energy for K + Ng, followed by Rb + Ng, and lowest in energy for Cs + Ng.

Table 11. Positions (nm) of blue shifted satellites associated with the difference potentials $B^2\Sigma^+_{1/2} - X^2\Sigma^+_{1/2}$ extrema. The D2 column lists the atomic alkali transition.

$M + Ng$	D2nis	This Work	exp[1]	exp[2]	exp[3]	exp[4]
K + He		692.7				
K + Ne	764.7	718.0				
K + Ar		713.7				
Rb + He		720.5				
Rb + Ne	778.2	739.9	754	752		
Rb + Ar		736.2	755.5	754		
Cs + He		810.9				827
Cs + Ne	850.1	822.8			837	837
Cs + Ar		820.6				838

[1]Carrington and Gallagher [1974]
[2]Drummond and Gallagher [1974]
[3]Readle et al. [2009]
[4]Hedges et al. [1972]

IV. Collisional broadening

All matter interacts with electromagnetic radiation by absorbing and emitting photons. Not all photons will interact with a particular atomic or molecular species, only those whose energies correspond to allowed transitions between the electronic states of said species. Therefore, the emission spectrum of such a species would consist of several narrow *spectral lines* at the energies of these transitions.

There are many effects which alter the resulting spectral lines from the above picture. The uncertainty principle of quantum mechanics relates the uncertainty in an excited state's energy to it lifetime. This effect results in an unshifted Lorentzian line profile centered on the corresponding electronic (fundamental) transition for the species. This type of broadening is referred to as *natural broadening*. The motion of the emitters results in Doppler shifts in their emitted frequency. Averaging these effects over all motions of the emitters results in a Gaussian spectral line. This is called Doppler broadening. Finally, interactions with neighboring atoms and molecules perturbs a particular species' energy levels during the interaction. The combined effects of these perturbations over many collisions results in a Lorentzian line shape which is broadened from the natural line shape and shifted from the fundamental transition frequency. This effect on the spectral lines is called *pressure broadening* since increasing the pressure increases the frequency of the collisions. When one measures the spectrum of a particular species the preceding effects combine, along with effects of the medium through which the radiation travels to the point of observation, to form the overall spectrum which is observed.

In this chapter a general theory of pressure broadening will be presented.

4.1 The General Anderson-Talman Theory

The general Anderson-Talman theory assumes the atom is a classically oscillating dipole. Such an oscillation can be imagined as the oscillation of a spring and its associated fundamental frequency. If this atom were isolated it would simply radiate at the fundamental angular frequency of its oscillation, ω_0. If this single atom made up the entire physical system, the differential equation describing the oscillation would be

$$\frac{\mathrm{d}^2x(t)}{\mathrm{d}t^2} + \omega_0^2 x(t) = 0.$$

The situation is complicated by collisions with other atoms, here referred to as perturbers, which influence the angular frequency of the oscillation during the collision. As such, the angular frequency of oscillation will be time dependent, $\phi(t)$, and the differential equation governing the oscillation becomes

$$\frac{\mathrm{d}^2x(t)}{\mathrm{d}t^2} + \phi^2(t)x(t) = 0. \tag{64}$$

To model this time-dependent angular frequency one must know the binary interaction potentials between the emitter and each perturber. If $E_j(R(t))$ and $E_i(R(t))$ are the upper and lower surfaces of such an interaction potential, where $R(t)$ is the internuclear separation of the emitter and perturber, and if the system is made up of just the emitter and one perturber, then the time dependent angular frequency can be written

$$\phi(t) = \hbar^{-1}[E_j(R(t)) - E_i(R(t))]$$

If the asymptotic energies are denoted E_{j0} and E_{i0} so that $E_j(R(t)) = E_{j0} + V_j(R(t))$

and $E_i(R(t)) = E_{i0} + V_i(R(t))$ then the time dependent angular frequency becomes

$$\begin{aligned} \phi(t) &= \hbar^{-1}[E_{j0} - E_{i0}] + \hbar^{-1}[V_j(R(t)) - V_i(R(t))] \\ &= \omega_0 + V_{ij}(R(t)), \end{aligned} \tag{65}$$

where $V_{ij}(R(t)) = V_j(R(t)) - V_i(R(t))$ is the term which measures the deviation from the fundamental frequency due to the position of the perturber. If there are N perturbers in the system, then this expression generalizes to the following, which for convenience in what follows is defined to be the time derivative of some function $\eta(t)$

$$\frac{\mathrm{d}\eta(t)}{\mathrm{d}t} \equiv \sum_{k=1}^{N} V_{ij}^{k}(R_k(t)). \tag{66}$$

This allows the following expression for $\omega(t)$

$$\phi(t) = \omega_0 + \frac{\mathrm{d}\eta(t)}{\mathrm{d}t}. \tag{67}$$

The function $\eta(t)$ contains all the time dependence of the angular frequency. The collision is assumed to start at time $t = 0$. The angular frequency is unperturbed at this time forcing $\frac{\mathrm{d}\eta(0)}{\mathrm{d}t} = 0$ (i.e. all the perturbers are in the asymptotic limit at this time).

Substituting Equation (67) into Equation (64) and working to zeroth order in powers of ω_0^{-1} yields the approximate solution [Trigt, 1966]

$$\begin{aligned} x(t) &= x_0 \exp\left\{ i \int_0^t \mathrm{d}\tau\, \phi(\tau) \right\} \\ &= x_0 \exp\left\{ i\omega_0 t + i \int_0^t \mathrm{d}\tau\, \frac{\mathrm{d}\eta(\tau)}{\mathrm{d}\tau} \right\} \\ &= x_0 \exp\left\{ i(\omega_0 t + \eta(t)) \right\}, \end{aligned} \tag{68}$$

where $i = sqrt{-1}$ and

$$\eta(t) = \int_0^t \mathrm{d}\tau \sum_{k=1}^{N} V_{ij}^k(R_k(\tau)). \tag{69}$$

In this theory one is not interested in the absolute but rather the relative intensity spectrum. Due to this, the constant x_0 will not be needed as the intensity spectrum will be normalized in the end and will be dropped for the rest of this discussion.

The intensity spectrum of the emitted radiation is given by the modulus square of the Fourier transform of the solution to the differential equation in Equation (64)

$$\begin{aligned}
I(\omega) &\propto \left| \int_{-\infty}^{+\infty} \mathrm{d}t \, \exp\{-i\omega t\} \, x(t) \right|^2 \\
I(\omega) &\propto \left| \int_{-\infty}^{+\infty} \mathrm{d}t \, \exp\{-i\omega t\} \, x(t) \right|^2 \\
&= \left| \int_{-\infty}^{+\infty} \mathrm{d}t \, \exp\{-i\omega t\} \exp\{i(\omega_0 t + \eta(t))\} \right|^2 \\
&= \left[\int_{-\infty}^{+\infty} \mathrm{d}t_1 \, \exp\{i\omega t_1\} \exp\{-i(w_0 t_1 + \eta(t_1))\} \right] \\
&\quad \times \left[\int_{-\infty}^{+\infty} \mathrm{d}t_2 \, \exp\{-i\omega t_2\} \exp\{i(w_0 t_2 + \eta(t_2))\} \right] \\
&= \int_{-\infty}^{+inf} \mathrm{d}t_1 \int_{-\infty}^{+\infty} \mathrm{d}t_2 \exp\{i\omega(t_2 - t_1)\} \\
&\quad \times \exp\{i(\omega_0(t_2 - t_1) + \eta(t_2) - \eta(t_1))\} \, .
\end{aligned} \tag{70}$$

At this point a change of variables is made in the integral over t_2 where t_1 is held constant. Let $s = t_2 - t_1$, then $\mathrm{d}s = \mathrm{d}t_2$ and $t_2 = s + t_1$. Substituting these expressions into Equation (70) and dropping the now obsolete subscript on t_1 yields

$$I(\omega) = \int_{-\infty}^{+\infty} \mathrm{d}t \int_{-\infty}^{+\infty} \mathrm{d}s \exp\{-i\omega s\} \exp\{i(\omega_0 s + \eta(s+t) - \eta(t))\} \, . \tag{71}$$

The following definition is made to simplify this expression for the intensity.

$$\begin{aligned}
\Delta\eta(t,s) &\equiv \eta(s+t)-\eta(t) \\
&= \int_0^{s+t}\sum_{k=1}^{N} V_{ij}^k(R_k(t)) - \int_0^{t}\sum_{k=1}^{N} V_{ij}^k(R_k(t)) \\
&= \int_t^{s+t}\sum_{k=1}^{N} V_{ij}^k(R_k(t)) \\
&= \sum_{k=1}^{N}\int_t^{s+t} V_{ij}^k(R_k(t)). \qquad (72)
\end{aligned}$$

Substituting Equation (72) into Equation (71) and rearranging yields

$$I(\omega) = \int_{-\infty}^{+\infty} \mathrm{d}s\, \exp\{-i\omega s\} \left\{ \int_{-\infty}^{+\infty} \mathrm{d}t \exp\{i(\omega_0 s + \Delta\eta(t,s))\} \right\}. \qquad (73)$$

The term in braces is a function of s, but it is not just any function. Define now the correlation function

$$\Phi'(s) \equiv \int_{-\infty}^{+\infty} \mathrm{d}t \exp\{i(\omega_0 s + \Delta\eta(t,s))\}. \qquad (74)$$

Substituting this into Equation (71) yields

$$I(\omega) = \int_{-\infty}^{+\infty} \mathrm{d}s\, \exp\{-i\omega s\}\, \Phi'(s). \qquad (75)$$

This illuminating form of the intensity reveals that it can be written as a Fourier transform of the correlation function. To simplify this, another change of variables $\omega \to \omega + \omega_0$ in Equation (73) is made so that now ω measures the angular frequency from line center instead of from zero. This leads to the simplification

$$I(\omega+\omega_0) = \int_{-\infty}^{+\infty} \mathrm{d}s\, \exp\{-i\omega s\}. \left\{ \int_{-\infty}^{+\infty} \mathrm{d}t \exp\{i\Delta\eta(t,s)\} \right\} \qquad (76)$$

The term in brackets is now defined as the line-center correlation function

$$\Phi(s) \equiv \int_{-\infty}^{+\infty} \mathrm{d}t \exp\left\{i\Delta\eta(t,s)\right\}, \tag{77}$$

and the line center intensity becomes

$$I(\omega+\omega_0) = \int_{-\infty}^{+\infty} \mathrm{d}s \, \exp\left\{-i\omega s\right\} \Phi(s). \tag{78}$$

Picking on the line center correlation function

$$\begin{aligned}
\Phi(s) &= \int_{-\infty}^{+\infty} \mathrm{d}t \exp\left\{i\Delta\eta(t,s)\right\} \\
&= \int_{-\infty}^{+\infty} \mathrm{d}t \exp\left\{ i \sum_{k=1}^{N} \int_{t}^{s+t} \mathrm{d}t' V_{ij}^{k}(R_k(t')) \right\} \\
&= \int_{-\infty}^{+\infty} \mathrm{d}t \prod_{k=1}^{N} \exp\left\{ i \int_{t}^{s+t} \mathrm{d}t' V_{ij}^{k}(R_k(t')) \right\}.
\end{aligned} \tag{79}$$

The integral over t in Equation (79) amounts to an average over a long time interval of a single emitter undergoing many collisions in this time. Since the collisional process is random, this picture is equivalent to an average over many emitters undergoing collisions in a short time interval all starting at the same initial time, here taken to be $t = 0$. The perturbers are assumed to follow straight line trajectories. Since the motion of the perturbers is isotropic and independent of each other they can all be assumed to travel in the x direction. Under these assumptions the position of the individual perturbers can be given the following functional form

$$R_k(t) = [b_k^2 + (x_{0k} + \overline{v}t)^2]^{\frac{1}{2}}, \tag{80}$$

where for the k^{th} perturber b_k is the impact parameter and x_{0k} is the initial position.

Under these assumptions the time average in Equation (79) becomes an average over collisions, denoted here as $\langle \ldots \rangle_{\text{collisions}}$, the line center correlation function becomes

$$\Phi(s) = \left\langle \prod_{k=1}^{N} \exp\left\{ i \int_0^s \mathrm{d}t \, V_{ij}^k([b_k^2 + (x_{0k} + \overline{v}t)^2]^{\frac{1}{2}}) \right\} \right\rangle_{\text{collisions}}. \tag{81}$$

At this point the perturbers are assumed to be identical (so they have the same interaction potential) and to act independently of each other. This allows the average of the product to be written as a product of the average

$$\Phi(s) = \left[\left\langle \exp\left\{ i \int_0^s \mathrm{d}t \, V_{ij}([b^2 + (x_0 + \overline{v}t)^2]^{\frac{1}{2}}) \right\} \right\rangle_{\text{collisions}} \right]^N. \tag{82}$$

The average over collisions is calculated by averaging over all initial positions of perturbers within a given volume $\mathcal{V} = 2\pi \int b \mathrm{d}b \int \mathrm{d}x_0$ yielding

$$\begin{aligned} \Phi(s) &= \left[\frac{2\pi}{\mathcal{V}} \int \int_{\mathcal{V}} b \, \mathrm{d}b \, \mathrm{d} \, x_0 \exp\left\{ -i \int_0^s \mathrm{d}t \, \hbar^{-1} V_{ij}([b^2 + (x_0^2 + \overline{v}t)^2]^{\frac{1}{2}}) \right\} \right]^N \\ &= \left[1 - \frac{2\pi}{\mathcal{V}} \int \int_{\mathcal{V}} b \, \mathrm{d}b \, \mathrm{d} \, x_0 \right. \\ &\quad \left. \times \left(1 - \exp\left\{ -i \int_0^s \mathrm{d}t \, \hbar^{-1} V_{ij} \left([b^2 + (x_0^2 + \overline{v}t)^2]^{\frac{1}{2}} \right) \right\} \right) \right]^N. \end{aligned} \tag{83}$$

In Equation (83) the line center correlation function has the form $[1-g]^N$. For $g \ll 1$ and $N \gg 1$ this form can be approximated $[1-g]^N \cong \exp\{-Ng\}$. Since g has a $\frac{1}{\mathcal{V}}$ in front, if the number density, n, is held constant while making the volume very large, the line center correlation function becomes

$$\Phi(s) = \exp\{-ng(s)\}, \tag{84}$$

where

$$g(s) = 2\pi \int_0^{+\infty} b\,\mathrm{d}b \int_{-\infty}^{+\infty} \mathrm{d}x_0 \times \left[1 - \exp\left\{-i \int_0^s \mathrm{d}t\, \hbar^{-1} V_{ij}([\rho^2 + (x_0 + \overline{v}t)^2]^{\frac{1}{2}})\right\}\right]. \quad (85)$$

Equations (84) and (85) form the basis for the general Anderson-Talman theory of spectral line broadening by collisions. The generality of the Anderson-Talman theory is illuminated by exploring two limiting cases.

4.1.1 Impact Approximation.

When the average velocity of the perturbers is high and the number density of the perturbers is low, it is possible to simplify the expression for the line center correlation function Equation (84). These conditions are equivalent to letting $s \to \infty$.

Consider the line center correlation function as s grows very large. The perturber will travel in the x-direction from x_0 to $x_0 + \overline{v}s$ during the time given for the collision. A large value for s results in a large distance traveled in the x-direction. In other words the perturbers are moving along very fast and only stay in the range of the interaction potential for a very short time. These are the conditions that meet what is called *the impact approximation*. It has been shown by Anderson [1952] that under these conditions $g(s)$ may be written

$$g(s) = (\alpha_0 + i\beta_0) + (\alpha + i\beta)s, \quad (86)$$

where

$$\alpha = 2\pi\overline{v} \int_0^{+\infty} b\,\mathrm{d}b \left[1 - cos\left\{(\hbar\overline{v})^{-1} \int_{-\infty}^{+\infty} \mathrm{d}x\, V([b^2 + x^2]^{\frac{1}{2}})\right\}\right], \quad (87)$$

$$\beta = 2\pi\overline{v}\int_0^{+\infty} b\,\mathrm{d}b\,sin\left\{(\hbar\overline{v})^{-1}\int_{-\infty}^{+\infty}\mathrm{d}x\,V([b^2+x^2]^{\frac{1}{2}})\right\}, \tag{88}$$

and the additive constant $\alpha_0 + i\beta_0$ is usually taken to be zero. Substituting these expressions into Equation (84) results in

$$\Phi(s) = \exp\{n(\alpha + i\beta)s\}. \tag{89}$$

The Fourier transform of this correlation function leads to an intensity spectrum which is a shifted and broadened Lorentzian. The unnormalized form of this is

$$I(\omega) = \frac{1}{(\omega - \omega_0 - n\beta)^2 + (n\alpha)^2}. \tag{90}$$

The shift is proportional to $n\beta$ and the broadening is proportional to $n\alpha$. As Michelson observed in 1895 [Michelson, 1885], these two quantities are linearly dependent on pressure.

4.1.2 Quasi-Static Approximation.

There are two conditions under which one arrives at another limiting expression for $g(s)$. If the pressure is increased dramatically by pumping more and more perturbers into the constant volume then the collision frequency is so high that the emitter is always undergoing a collision. At any point in time there there is some random number of perturbers in some random configuration around each emitter. When the average over a long time period for a single emitter is replaced with the average over collisions for many emitters under these conditions the positions of the perturbers in each collision can be considered constant. The other condition which leads to this limit is when the temperature is dropped very low causing the average velocity of the perturbers to be very small.

This other limit is achieved by letting $s \to 0$. In this case the interaction potential in $g(s)$ is no longer time dependent, being only a function of R. Changing to spherical coordinates yields

$$\begin{aligned} g(s) &= 2\pi \int_0^{+\infty} b\,\mathrm{d}b \int_{-\infty}^{+\infty} \mathrm{d}x_0 \\ &\quad \times \left[1 - \exp\left\{-i \int_0^s \mathrm{d}t\, \hbar^{-1} V_{ij}([\rho^2 + x_0^2]^{\frac{1}{2}})\right\}\right] \\ &= \int_{\mathcal{V}} \mathrm{d}\mathcal{V} \left[1 - \exp\left\{\frac{-i}{\hbar} V_{ij}(R)s\right\}\right] \\ &= 4\pi \int_0^{+\infty} \mathrm{d}r\, r^2 \left[1 - \exp\left\{\frac{-i}{\hbar} V_{ij}(R)s\right\}\right]. \end{aligned} \tag{91}$$

4.2 Computational model of AT theory

The remainder of this chapter details my work on computationally modeling the Anderson-Talman general theory of pressure broadening(AT). The goal is to calculate $g(s)$ as given in Equation (85) for a particular difference potential (DP) and value of the velocity. Imagine a half plane where the horizontal axis is labeled by x ranging from $-\infty < x < \infty$ and the vertical axis is labeled by b ranging from $0 \leq b < \infty$. The emitting atom is located at the origin. Consider all perturbers moving in the positive x direction with constant velocity $\bar{v}$. In this case the value of b becomes the impact parameter. By virtue of the cylindrical symmetry of the collision, if one carries out the integration in this half plane then one can just multiply the result by 2π to get the correct answer. Define (x_0,b) as the initial point of the perturber, s as the time it moves along its trajectory, $\hbar$ as Plank's constant divided by 2π, and $\Delta V(R)$ is the DP evaluated at internuclear separation R. It is now possible to define the following function,

$$\theta = \theta(x_0, b, s) \equiv -\hbar^{-1} \int_0^s \mathrm{d}\tau\, \Delta V\left([b^2 + (x_0 + \bar{v}\tau)^2]^{1/2}\right), \tag{92}$$

and $g(s)$ becomes,

$$g(s) = 2\pi \int_0^\infty b\,\mathrm{d}b \int_{-\infty}^\infty \mathrm{d}x_0 \left\{1 - \exp\{i\theta(x_0, b, s)\}\right\}. \tag{93}$$

$g(s)$ is a complex function. Its real and imaginary parts are given by,

$$\begin{aligned} \mathrm{Re}[g(s)] &= 2\pi \int_0^\infty b\,\mathrm{d}b \int_{-\infty}^\infty \mathrm{d}x_0 \left\{1 - \cos\{\theta(x_0, b, s)\}\right\} \\ \mathrm{Im}[g(s)] &= 2\pi \int_0^\infty b\,\mathrm{d}b \int_{-\infty}^\infty \mathrm{d}x_0 \left\{-\sin\{\theta(x_0, b, s)\}\right\}. \end{aligned} \tag{94}$$

The above formulation, while elegant mathematically, is computationally impractical. This is due, in part, to a rapidly oscillating integrand for a portion of the integral over x_0. Another issue is the above equations contain many computational redundancies. Modifying the above equations to eliminate these redundancies greatly reduces the amount of operations needed to perform the evaluation of $g(s)$. As an example of the computational effort required in directly integrating the above equations, an adaptive Gauss-Kronrod quadrature implemented in the Matlab programming environment was used to evaluate $g(s)$ for only one value of s did not complete after several days of running on a modern PC. A different approach is warranted for numerical integration of an arbitrary potential.

The above equations can be simplified for the purposes of computational expediency by taking advantages of certain properties of $\Delta V(R)$. As seen in Figure 24 $\Delta V(R) \to 0$ as $R \to \infty$, so $\Delta V(R)$ is a slowly varying function for sufficiently large values of R. However, as one moves in from the asymptotic limit, one reaches a point where $\Delta V(R)$ begins to change more appreciably. With this in mind, the following two variables are introduced: r_l is the value of R beyond which $\Delta V(R)$ is effectively zero for computational purposes and r_s is the value of R where $\Delta V(R)$ begins to change rapidly. Just by how much $\Delta V(R)$ needs to change with respect to R for

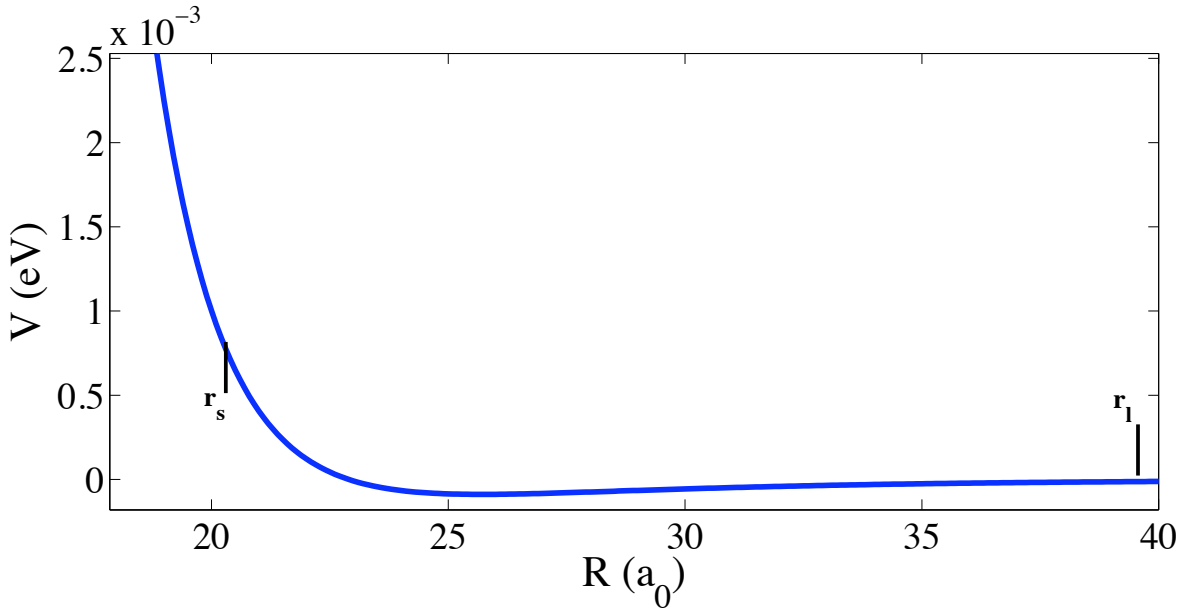

Figure 24. The Lenard-Jones difference potential derived from measurements of the D2 line of Rb perturbed by He. The difference potential is considered effectively zero beyond r_l and rapidly changing for $R < r_s$. This latter assumption is only true if the region of $R < r_s$ contains no extremums.

the change to be considered appreciable will become an adjustable parameter to the numerical calculation. Hence forth the region of the potential in between r_s and r_l will be denoted as the long range portion of $\Delta V(R)$, while the region between zero and r_s will be denoted as the short range portion of $\Delta V(R)$. The DP is assumed to be zero for $R > r_l$.

Figure 25 pictorially represents the inner and outer regions of the DP in the (x, b) plane and demonstrates two possible cases for the integration over x_0 dependent on the value of b for which this integration takes place. In case I b is greater than or equal to r_s and trajectories along this impact parameter will only interact with the long range portion of the DP. In case II b is smaller than r_s and trajectories along this impact parameter will interact with both the long and short range parts of $\Delta V(R)$. The integral over b can be broken up into two integrals: the first ranging from zero to r_s and the second ranging from r_s to r_l. Both of these cases will be considered

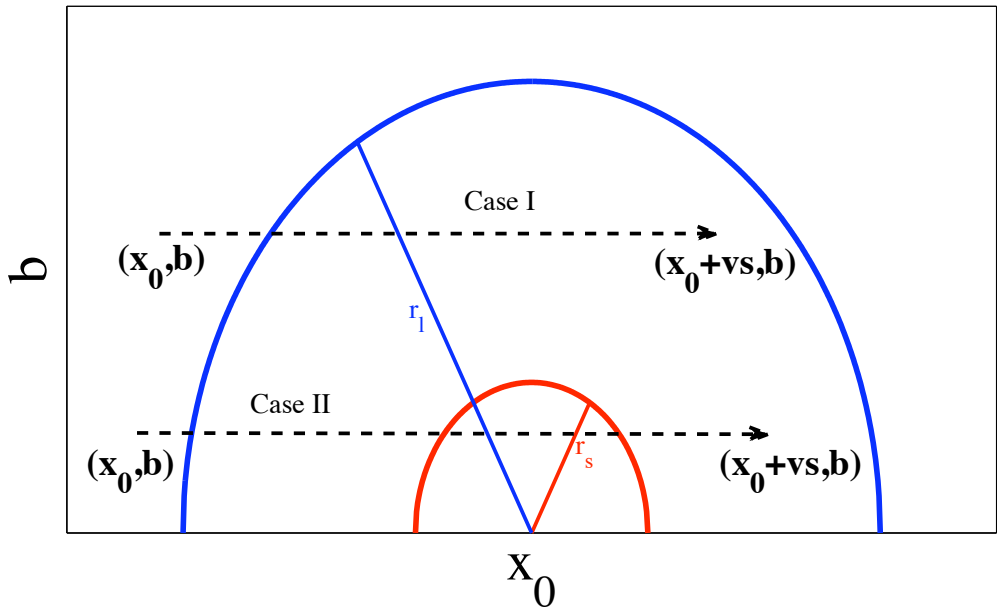

Figure 25. All perturbers are assumed moving in the positive x-direction with constant velocity and different impact parameters b. Two possible cases are treated and shown in the figure, one where $b < r_s$ and the other for $r_s \leq b < r_l$.

separately in what follows.

4.2.1 Case I: $b \geq r_s$.

Before proceeding it is beneficial to construct some useful quantities. First, given b, the values of x where a trajectory intersects the circle of radius r_l are

$$x_l^-(b) \equiv -(r_l^2 - b^2)^{1/2} \tag{95}$$

and

$$x_l^+(b) \equiv (r_l^2 - b^2)^{1/2}. \tag{96}$$

Another useful quantity is the time required for a perturber located at $x_l^-(b)$ to travel to $x_l^+(b)$. This is given by,

$$t_r(b) \equiv \frac{x_l^+(b) - x_l^-(b)}{\bar{v}}. \tag{97}$$

It will be shown that all numerical calculations for this value of b become redundant when $s \geq t_r(b)$, that is all calculations required to know $g(s > t_r(b))$ will have been calculated when $s = t_r(b)$. Thus, these values can simply be stored when $s = t_r(b)$ and then reused for greater values of s instead of inefficiently recalculated.

In order to numerically calculate $g(s)$ one must choose a set of values for s and then evaluate $g(s)$ at each of these points. For a given value of s and b, only a certain subset of the possible values for x_0 whose resultant trajectories cross the non-zero region of the DP will yield any contribution to $g(s)$. The values of x_0 which fit this criteria fall in the range $x_l^-(b) - \bar{v}s < x_0 < x_l^+(b)$. Thus,

$$\int_{-\infty}^{\infty} \mathrm{d}x_0 \, \{\cdots\} = \int_{x_l^-(b)-\bar{v}s}^{x_l^+(b)} \mathrm{d}x_0 \, \{\cdots\}, \tag{98}$$

where,

$$\{\cdots\} \equiv 1 - \exp\{i\theta(x_0, b, s)\}. \tag{99}$$

The DP's radial nature makes it symmetric about the b axis. This allows for a simplification of the expression in Equation (98) for $s \leq t_r(b)$. Define the distance between the limits in the right hand side of Equation (98) as,

$$d = d(b, s) \equiv x_l^+(b) - x_l^-(b) + \bar{v}s. \tag{100}$$

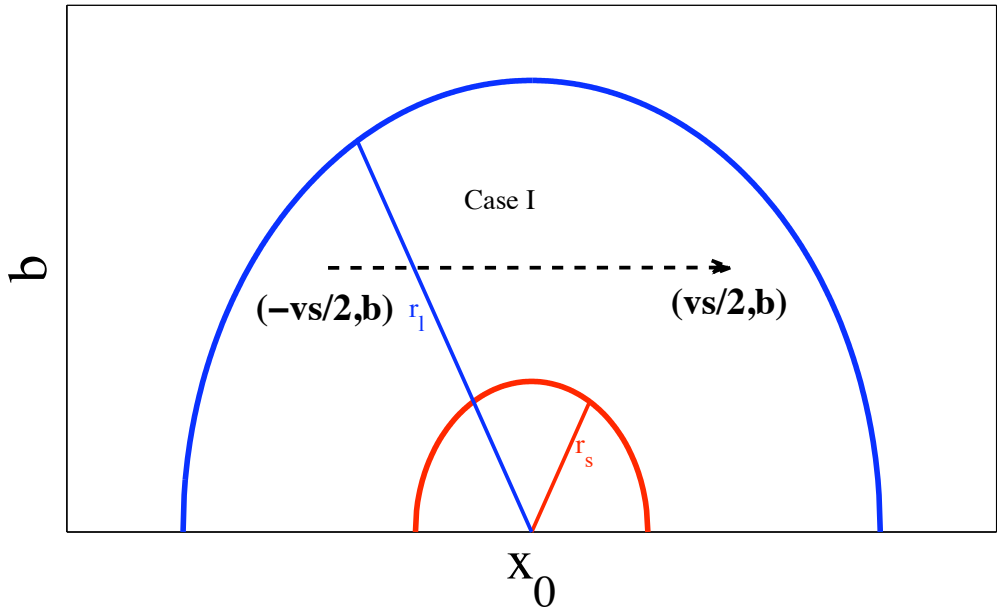

Figure 26. The nature of the spherical symmetry of the binary interaction causes the sum of all trajectories such that $x_0 < -\frac{vs}{2}$ be equal to the sum of the trajectories such that $x_0 > -\frac{vs}{2}$. A numerical routine need only calculate one of these, multiplying the result by two and saving half the work. Note that as s increases the starting point of the symmetrical trajectory drifts back to smaller values of x_0.

Consider the trajectory which has the initial condition,

$$\begin{aligned} x_0 &= x_l^+(b) - \frac{d}{2} \\ &= x_l^+ - \frac{1}{2}(x_l^+(b) - x_l^-(b) + \bar{v}s) \\ &= x_l^+ - \frac{1}{2}(2x_l^+(b) + \bar{v}s) \\ &= -\frac{\bar{v}s}{2}. \end{aligned} \tag{101}$$

Thus this trajectory starts at the point $(-\frac{\bar{v}s}{2}, b)$ and ends at the point $(\frac{\bar{v}s}{2}, b)$, covering symmetric regions of the DP. Now, if one imagines integrating over x_0 from $x_l^-(b) - \bar{v}s$ to $-\frac{\bar{v}s}{2}$ then one is integrating over all trajectories from the one whose end point is equal to $x_l^-(b)$ to the beginning of the symmetric trajectory just described. On the other hand, if one integrates over x_0 from $-\frac{\bar{v}s}{2}$ to $x_l^+(b)$ one is integrating over all trajectories beginning with the symmetric trajectory to the trajectory which begins at $x_0 = x_l^+(b)$. Since the potential is symmetric about the b axis the integration over these two sets of trajectories is equivalent and one can write,

$$\begin{aligned} \int_{x_l^-(b)-\bar{v}s}^{x_l^+(b)} \mathrm{d}x_0 \{\cdots\} &= 2\int_{x_l^+(b)-\frac{d}{2}}^{x_l^+(b)} \mathrm{d}x_0 \{\cdots\} \\ &= 2\int_{-\bar{v}s/2}^{x_l^+(b)} \mathrm{d}x_0 \{\cdots\} \end{aligned} \tag{102}$$

For $s \leq t_r(b)$, Equation (102) holds and its integral must be handled numerically. The situation changes when $s > t_r(b)$ and the remainder of this section will discuss these modifications.

Define the following useful quantities, dependent only on b, which are both evaluated when $s = t_r(b)$,

$$\phi_I(b) \equiv \left[2\int_{-\bar{v}s/2}^{x_l^+(b)} \mathrm{d}x_0 \{\cdots\} \right]_{s=t_r(b)}, \tag{103}$$

and,

$$\theta_{max}(b) \equiv \theta(x_l^-(b), b, t_r(b)). \tag{104}$$

The quantity $\theta_{max}(b)$ is the result of performing a line integral over a trajectory which entirely passes through the interaction region of the potential at a given impact parameter. The range of x_0 for which $\theta(x_0, b, s) = \theta_{max}(b)$ is given by $x_l^-(b) - \bar{v}(s - t_r(b)) \leq x_0 \leq x_l^-$, and $\theta(x_0, b, s)$ is constant over this region. Breaking up the original integral in Equation (98) with this in mind one arrives at,

$$\begin{aligned}
\int_{x_l^-(b)-\bar{v}s}^{x_l^+(b)} \mathrm{d}x_0 \{\cdots\} &= \int_{x_l^-(b)-\bar{v}s}^{x_l^-(b)-\bar{v}(s-t_r(b))} \mathrm{d}x_0 \{\cdots\} \\
&\quad + \int_{x_l^-(b)-\bar{v}(s-t_r(b))}^{x_l^-(b)} \mathrm{d}x_0 \{\cdots\} \\
&\quad + \int_{x_l^-(b)}^{x_l^+(b)} \mathrm{d}x_0 \{\cdots\}.
\end{aligned} \tag{105}$$

The first and third terms in this equation pick up all the values of x_0 which have not yet reached θ_{max} (and the values of $x_0 > x_l^-(b)$ never will). The sum of these two terms is what is captured in Equation (103). Therefore, the first and third terms in Equation (105) may be replaced by $\phi_I(b)$ and are no longer functions of s. As for the second term in Equation (105), $\theta(x_0, b, s)$ is constant over the range of the integral and equal to θ_{max}. One can then write,

$$\begin{aligned}
\int_{x_l^-(b)-\bar{v}(s-t_r(b))}^{x_l^-(b)} \mathrm{d}x_0 \{\cdots\} &= \{\cdots|_{\theta=\theta_{max}}\} \int_{x_l^-(b)-\bar{v}(s-t_r(b))}^{x_l^-(b)} \mathrm{d}x_0 \\
&= \{\cdots|_{\theta=\theta_{max}}\} \bar{v}(s - t_r(b)).
\end{aligned} \tag{106}$$

Combining the above results one can finally write,

$$\int_{-\infty}^{\infty} \mathrm{d}x_0 \{\cdots\} = 2\int_{x_l^-(b)-\frac{d(b,s)}{2}}^{x_l^+(b)} \mathrm{d}x_0 \{\cdots\}, s < t_r(b)$$
$$\phi_I(b) + \{\cdots|_{\theta=\theta_{max}}\}\bar{v}(s - t_r(b)), s \geq t_r(b). \quad (107)$$

As s becomes large enough, all contributions from the integrals over x_0 for $b \geq r1$ become linear with s. Further, for $s > t_r(b)$ the evaluation of the integral over x_0 requires no new numeric effort, only the values $\phi_I(b)$ and θ_{max} are required. Therefore any new numeric calculations would be redundant and $s = t_r(b)$ is the time beyond which these redundancies would occur.

4.2.2 Case II: $b < r_s$.

In this region of b, in addition to the values of $x_l^-(b)$ and $x_l^+(b)$ defined above, the following definitions will be useful,

$$x_s^-(b) \equiv -(r_s^2 - b^2)^{1/2}, \quad (108)$$

and,

$$x_s^+(b) \equiv (r_s^2 - b^2)^{1/2}. \quad (109)$$

The s in the above subscripts stands for short-range potential. As in case I there will be a redundant time here. An exploration of the integral over x_0 will illuminate the proper definition the redundant time in case II. In this pursuit the following definitions will prove useful,

$$t_s(b) \equiv \frac{x_s^+(b) - x_s^-(b)}{\bar{v}}, \quad (110)$$

and,

$$t_l(b) \equiv \frac{x_l^+(b) - x_s^+(b)}{\bar{v}}. \tag{111}$$

The time defined by $t_s(b)$ is the time it takes a trajectory to cross the short-range portion of ΔV. Analogously the time defined by $t_l(b)$ is the time it takes a trajectory to cross the long range portion of the potential, either on the negative or positive portions of the x-axis. This means that the time it takes to cross the entire range of the potential for a given impact parameter is $t_s(b) + 2t_l(b)$ (spoiler: this total time is the $t_r(b)$ for case II).

To proceed in analyzing case II consider that Equation (98) still holds, and the integral over x_0 can be further broken up as follows,

$$\begin{aligned}\int_{-\infty}^{\infty} \mathrm{d}x_0 \{\cdots\} &= \int_{x_l^-(b)-\bar{v}s}^{x_s^-(b)-\bar{v}s} \mathrm{d}x_0 \{\cdots\} + \int_{x_s^-(b)-\bar{v}s}^{x_s^+(b)} \mathrm{d}x_0 \{\cdots\} \\ &\quad + \int_{x_s^+(b)}^{x_l^+(b)} \mathrm{d}x_0 \{\cdots\}. \end{aligned} \tag{112}$$

Consider the first and third terms in this expression. Notice that the distance from the lower limit to the upper limit is the same in each term. The spherically symmetric nature of the DP implies that the integration of all the trajectories ending in the long-range portion of ΔV on the negative side of the x-axis is equivalent to integrating all trajectories which begin in the long-range portion of ΔV on the positive side of the x-axis. Thus one can write,

$$\int_{x_l^-(b)-\bar{v}s}^{x_s^-(b)-\bar{v}s} \mathrm{d}x_0 \{\cdots\} + \int_{x_s^+(b)}^{x_l^+(b)} \mathrm{d}x_0 \{\cdots\} = 2\int_{x_s^+(b)}^{x_l^+(b)} \mathrm{d}x_0 \{\cdots\}. \tag{113}$$

The integral on the right hand side of Equation (113) starts from zero when $s = 0$ and grows to a maximum contribution at $s = t_l(b)$. After this time the value of the integral becomes constant and may be stored for future use instead of expending more

computational resources on its evaluation. This discussion motivates the following definition,

$$\phi_l(b) = \left[2 \int_{x_s^+(b)}^{x_l^+(b)} \mathrm{d}x_0 \, \{\cdots\} \right]_{s=t_l(b)} \tag{114}$$

The quantity $\phi_l(b)$ represents the maximal and constant contribution to the integral over x_0 of the terms in Equation (113) for $s \geq t_l(b)$.

The second term in Equation (112) warrants some special consideration and is restated here for emphasis,

$$\int_{x_s^-(b)-\bar{v}s}^{x_s^+(b)} \mathrm{d}x_0 \, \{\cdots\} \tag{115}$$

The range of this integral contains every value of x_0 whose trajectory will cross the short range portion of the potential for the given value of s. To further break this integral up one must consider several ranges of time.

For $s \leq t_s(b)$ every trajectory starting from an x_0 in the range of Equation (115) will either start or end in the short-range portion of ΔV. Therefore, the values of $\theta(x_0, b, s)$ for x_0 in close proximity to each other will be changing considerably, and the integrands belonging to the integral over x_0 will be oscillating very quickly. As a result, the integral over this range of x_0 can be approximated. For the real part $\mathrm{Re}[\{\cdots\}] = 1 - \cos\{\theta(x_0, b, s)\}$ the integrand rapidly oscillates between zero and two over a region of x defined by the limits of the integral. In the limit of infinite frequency this oscillation will pick up exactly half the area of the box, i.e. $x_s^+(b) - x_s^-(b) + \bar{v}s$. For the imaginary part $\mathrm{Im}[\{\cdots\}] = -sin\{\theta(x_0, b, s)\}$ the integrand rapidly oscillated between the values of negative one and one, thereby canceling any positive contribution with an equal amount of negative contribution. In summation, for $s < t_s(b)$ one can write,

$$\int_{x_s^- - \bar{v}s}^{x_s^+(b)} \mathrm{d}x_0 \, \{\cdots\} \approx x_s^+(b) - x_s^-(b) + \bar{v}s. \tag{116}$$

When $s = t_s(b)$ then the above integral reaches its maximum for the real part (the imaginary contribution is always zero). Define the following quantity which is equal to Equation (116) for $s = t_s(b)$,

$$\begin{aligned} \phi_a(b) &\equiv \left[\int_{x_s^- - \bar{v}s}^{x_s^+(b)} \mathrm{d}x_0 \, \{\cdots\} \right]_{s=t_s(b)} \\ &= 2(x_s^+(b) - x_s^-(b)). \end{aligned} \tag{117}$$

$\phi_a(b)$ approximates the total contribution of trajectories which either begin or end in the short-range portion of ΔV for all $s \geq t_s(b)$.

Next consider the range of time $t_s(b) < s \leq t_s(b) + t_l(b)$. For this range one can break up Equation (115) in the following manner,

$$\begin{aligned} \int_{x_s^-(b) - \bar{v}s}^{x_s^+(b)} \mathrm{d}x_0 \, \{\cdots\} &= \int_{x_s^-(b) - \bar{v}s}^{x_s^+(b) - \bar{v}s} \mathrm{d}x_0 \, \{\cdots\} + \int_{x_s^+(b) - \bar{v}s}^{x_s^-(b)} \mathrm{d}x_0 \, \{\cdots\} \\ &\quad + \int_{x_s^-(b)}^{x_s^+(b)} \mathrm{d}x_0 \, \{\cdots\}. \end{aligned} \tag{118}$$

Consider the first and third terms in this equation. First note that the differences of their limits are the same. The first term represents all trajectories which end in the short range portion of the potential. The third term represents all the trajectories which begin in the short range portion of the potential. As a result, the integrands for these regions will be rapidly oscillating and the results above for $s < t_s(b)$may be applied to these integrals. As a consequence both of these terms are equal to each other and their sum is equal to $\phi_a(b)$.

As for the second term in Equation (118), this represents all of the trajectories which begin inn the long-range portion of ΔV on the negative side of the x-axis, pass entirely through the short-range portion of ΔV, and end in the long-range portion of ΔV. An example of one of these trajectories is shown in Figure 27.

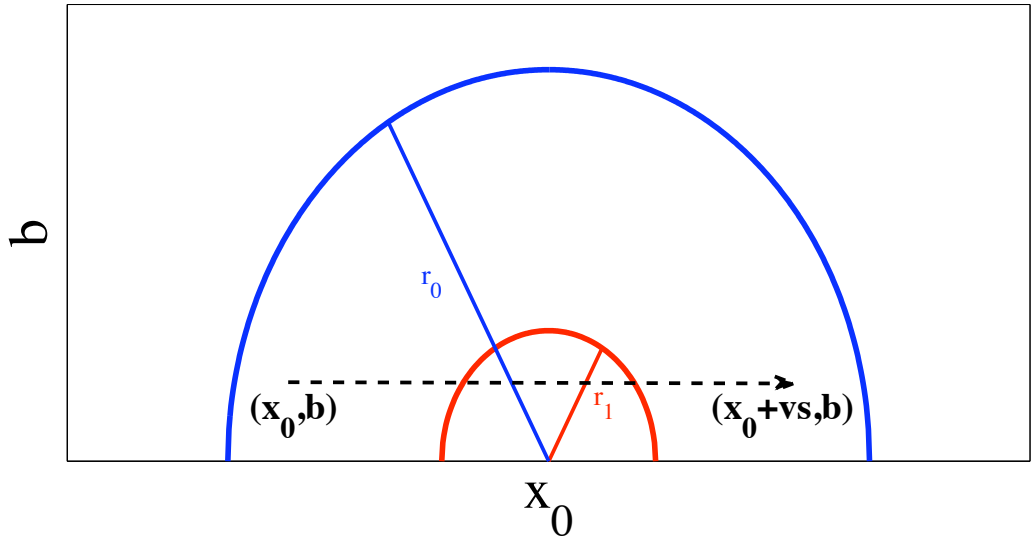

Figure 27. An example of a trajectory which starts in the long range portion of the potential, passes through the short range portion, and ends again in the long range portion.

When $s = t_s(b)$ this term is zero as no trajectories fit the criteria given in Figure 27. Only the value of $x_0 = x_s^-(b)$ has a trajectory that completely crosses the inner potential. As s grows more and more values of x_0 have this type of trajectory, specifically the ones falling in the range $x_s^-(b) - \bar{v}(s - t_s(b)) < x_0 \leq x_s^-(b)$. This continues until s grows to the value $s = t_s(b) + t_l(b)$ when the second term in Equation (118) reaches its maximum amount of contribution. This is because at this time all trajectories starting from a x_0 in the range $x_l^-(b) < x_0 < x_s^-(b)$ entirely cross the short-range portion of ΔV and end in the long-range portion of ΔV on the positive side of the x-axis. Each trajectory which entirely cross the short-range portion of ΔV will pick up the same contribution to $\theta(x_0, b, s)$ during this time which will be defined as,

$$\theta_s(b) \equiv \theta(x_s^-(b), b, t_s(b)). \tag{119}$$

This means that the differences in $\theta(x_0, b, s)$ for these values of x_0 are due to sampling

different portions of the long-range portion of ΔV. Therefore these variations will be small and the integrand for the integration over x_0 will no longer be rapidly oscillating.

If one considers the evaluation of $\theta(x_0, b, s)$ for the second term in Equation (118) it is possible to write,

$$\begin{aligned}
\theta(x_0,b,s) &= -\hbar^{-1}\int_0^s \mathrm{d}\tau\, \Delta V(\cdots) \\
&= -\hbar^{-1}\int_0^{s_1} \mathrm{d}\tau\, \Delta V(\cdots) - \hbar^{-1}\int_{s_1}^{s_2} \mathrm{d}\tau\, \Delta V(\cdots) \\
&\quad -\hbar^{-1}\int_{s_2}^{s} \mathrm{d}\tau\, \Delta V(\cdots) \\
&= -\hbar^{-1}\int_0^{s_1} \mathrm{d}\tau\, \Delta V(\cdots) + \theta_s(b) - \hbar^{-1}\int_{s_2}^{s} \mathrm{d}\tau\, \Delta V(\cdots), \qquad (120)
\end{aligned}$$

where $\Delta V(\cdots) = \Delta V([b^2 + (x_0 + \bar{v}\tau)^2]^{1/2})$, $s_1 = s_1(x_0, b) \equiv (x_s^-(b) - x_0)/\bar{v}$, and $s_2 = s_2(x_0, b) \equiv (x_0 - x_s^+(b))/\bar{v}$.

Note that for $t_s(b) < s < t_s(b)+t_l(b)$ one can write $x_s^+(b)-\bar{v}s = x_s^-(b)-\bar{v}(s-t_s(b))$. All of this allows one to write, for $t_s(b) < s \leq t_s + t_l$,

$$\int_{x_s^-(b)-\bar{v}s}^{x_s^+(b)} \mathrm{d}x_0\, \{\cdots\} = \int_{x_s^-(b)-\bar{v}(s-t_s(b))}^{x_s^-(b)} \mathrm{d}x_0\, \{\cdots\} + \phi_A(b). \qquad (121)$$

Now consider the range of s where $t_s(b) + t_l(b) < s \leq t_s(b) + 2t_l(b)$. In this case Equation (115) can be written,

$$\begin{aligned}
\int_{x_s^-(b)-\bar{v}s}^{x_s^+(b)} \mathrm{d}x_0\, \{\cdots\} &= \int_{x_s^-(b)-\bar{v}s}^{x_s^+(b)-\bar{v}s} \mathrm{d}x_0\, \{\cdots\} + \int_{x_s^+(b)-\bar{v}s}^{x_l^-(b)} \mathrm{d}x_0\, \{\cdots\} \\
&\quad + \int_{x_l^-(b)}^{x_l^+(b)-\bar{v}s} \mathrm{d}x_0\, \{\cdots\} + \int_{x_l^+(b)-\bar{v}s}^{x_s^-(b)} \mathrm{d}x_0\, \{\cdots\} \\
&\quad + \int_{x_s^-(b)}^{x_s^+(b)} \mathrm{d}x_0\, \{\cdots\} \qquad (122)
\end{aligned}$$

The first term in this equation represents all trajectories which end inside the short

range potential, while the last term represents all trajectories which start in this region. As before, these two terms are equal and their sum is equal to $\phi_A(b)$.

At this point it is useful to consider that, for this range of s, the limit $x_s^+(b) - \bar{v}s = x_l^-(b) - \bar{v}(s - [t_s(b) + t_r(b)])$ and $x_l^+(b) - \bar{v}s = x_s^-(b) - \bar{v}(s - [t_s(b) + t_r(b)])$. These relationships help to simplify the limits on the integrals in the above expression.

Examining the second term in Equation (122) one can see that the upper and lower limits are the same for $s = t_s(b) + t_l(b)$, thus this term equals zero for this value of s. As s grows this term captures all the trajectories which start outside the full range of the potential (i.e. $x_0 < x_l^-(b)$) and pass through the DP far enough to end in the second part of the long range potential. An example of this kind of trajectory is shown in Figure 28.

As s increases to $s = t_s(b) + 2t_l(b)$ the range of x_0 whose trajectories fit this description grows to $x_s^+(b) - \bar{v}s < x_0 < x_l^+(b) - \bar{v}s$. The difference of the the upper and lower limits of this range is equal to $x_l^+ - x_s^+$, so the full span of the long-range portion of ΔV on the positive side of the x-axis has trajectories ending in it which are due to the second term in Equation (122). As time increases beyond this value the range of x_0 whose trajectories meet this condition stays the same in length, as the endpoints of the range both move the $s = t_s(b) + t_l(b)$ to a maximum contribution when $s = t_s(b) + 2t_l(b)$ and be constant beyond this time.

To calculate a value of $\theta(x_0, b, s)$ for the second term in Equation (122) first define,

$$\begin{aligned} \theta_l(b) &\equiv \theta(x_l^-(b), b, t_l(b)) \\ &= \theta(x_s^+(b), b, t_l(b)). \end{aligned} \tag{123}$$

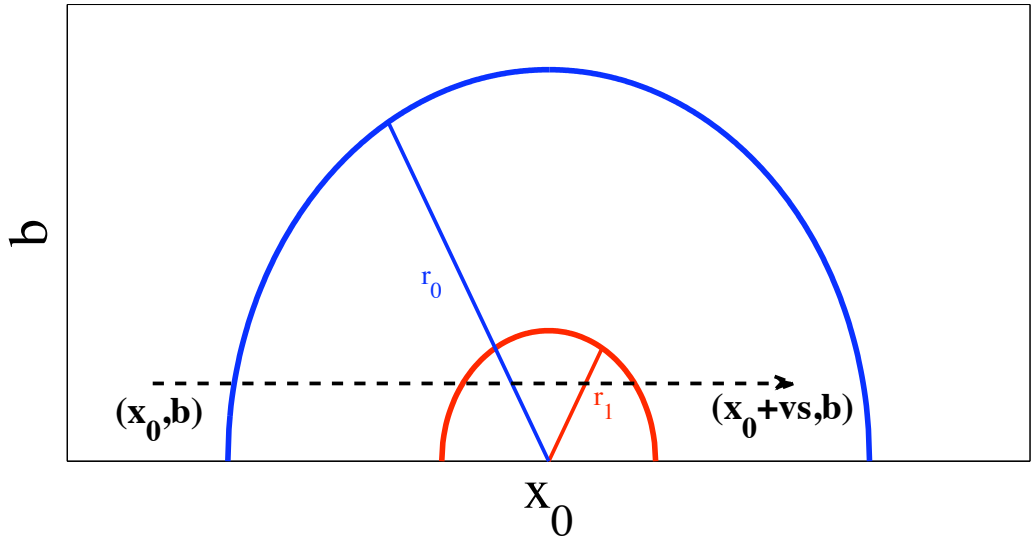

Figure 28. An example of a trajectory which starts outside the full range of the potential, passes through the first long range and short range portions, and ends in the second long range portion.

This allow one to write,

$$\begin{aligned}
\theta(x_0, b, s) &= -\hbar^{-1} \int_0^s \mathrm{d}\tau\, \Delta V(\cdots) \\
&= -\hbar^{-1} \int_0^{s_1} \mathrm{d}\tau\, \Delta V(\cdots) - \hbar^{-1} \int_{s_1}^{s_2} \mathrm{d}\tau\, \Delta V(\cdots) \\
&\quad -\hbar^{-1} \int_{s_2}^{s} \mathrm{d}\tau\, \Delta V(\cdots) \\
&= \theta_l(b) + \theta_s(b) - \hbar^{-1} \int_{s_2}^{s} \mathrm{d}\tau\, \Delta V(\cdots). \qquad (124)
\end{aligned}$$

Here s_1, s_2, and $\Delta V(\cdots)$ carry their same definition as in Equation (120).

Now consider the third term in Equation (122). This term is equivalent to the second term in Equation (118) in so far as it represents all trajectories of the type in Figure 27. At the beginning of this time interval, when $s = t_s(b) + t_l(b)$, every trajectory starting in the range $x_l^-(b) \leq x_0 < x_s^-(b)$ falls into this category and the contribution of this term is at a maximum. As s increases the range of x_0 which

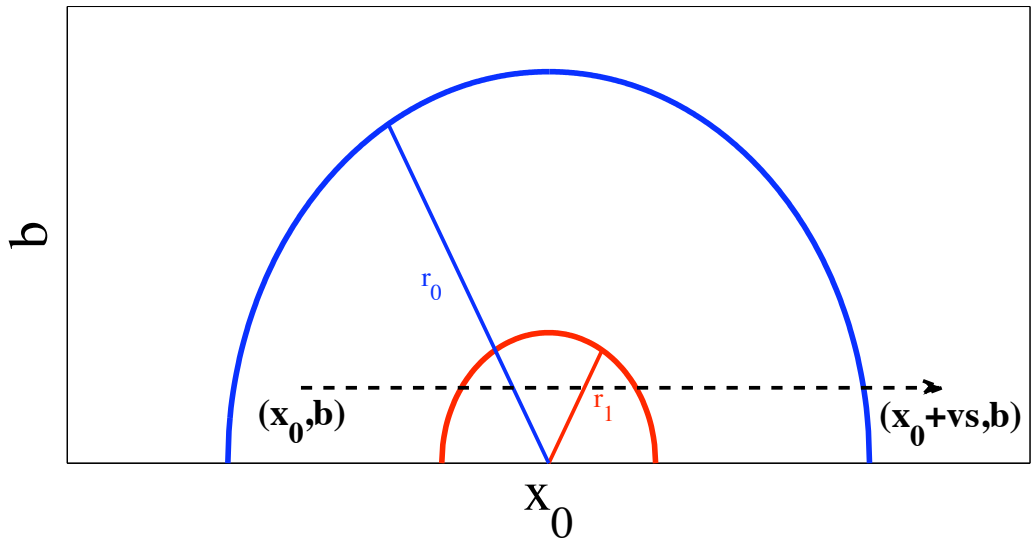

Figure 29. An example of a trajectory which starts inside the long range of the potential, passes entirely through the short range and second long range portions, and ends outside the full range of the potential.

produces trajectories in this category reduces, being $x_l^-(b) \leq x_0 < x_s^-(b) - \bar{v}(s - [t_s(b) + t_l(b)])$. All trajectories which fall into this category disappear completely for $s \geq t_s(b) + 2t_l(b)$ and this term goes to zero when $s = t_s(b) + 2t_l(b)$. Evaluations of $\theta(x_0, b, s)$ for values of x_0 in this term can be made using Equation (120).

The fourth term in Equation (122) is the final term in this equation to consider. Just as in the case of the second term in this equation, the fourth term starts as zero when $s = t_s(b) + t_l(b)$ due to the upper and lower limits being the same. As s increases, this term captures all trajectories which begin in the range $x_s^-(b) - \bar{v}(s - [t_s(b) + t_l(b)]) \leq x_0 < x_s^-(b)$, pass entirely through the short-range portion of ΔV as well as the long-range portion of ΔV on the positive side of the x-axis, ending totally outside the range of the potential. An example of this kind of trajectory is given in Figure 29. As s goes to $s = t_s(b) + 2t_l(b)$ this term grows to a maximum because at this value of s all trajectories starting in the range $x_l^-(b) \leq x_0 < x_s^-(b)$ fall into this category.

To calculate a value of $\theta(x_0, b, s)$ for the fourth term in Equation (122) one can write,

$$\begin{aligned}
\theta(x_0, b, s) &= -\hbar^{-1} \int_0^s \mathrm{d}\tau \, \Delta V(\cdots) \\
&= -\hbar^{-1} \int_0^{s_1} \mathrm{d}\tau \, \Delta V(\cdots) - \hbar^{-1} \int_{s_1}^{s_2} \mathrm{d}\tau \, \Delta V(\cdots) \\
&\quad -\hbar^{-1} \int_{s_2}^{s} \mathrm{d}\tau \, \Delta V(\cdots) \\
&= -\hbar^{-1} \int_0^{s_1} \mathrm{d}\tau \, \Delta V(\cdots) + \theta_s(b) + \theta_l(b). \qquad (125)
\end{aligned}$$

It is worth exploring the relationship between the second and fourth terms in Equation (122). Over the range $t_s(b) + t_l(b) < s \leq t_s(b) + 2t_l(b)$ both of these terms start at zero and, as can be seen when considering the symmetry of the potential about the b-axis, they both accumulate to the same value. Now, consider the first time increment above the lower limit. The second term picks up a small contribution to the negative side of $x_s^-(b)$ while the fourth term picks up the same symmetric region to the positive side of $x_s^+(b)$. Thus both terms accumulate the same contribution for this step. This pattern continues over the entire range of s in this interval, and at each time the contributions of the two terms is the same.

With all of these considerations it is possible to write for $t_s(b) + t_l(b) < s \leq t_s(b) + 2t_l(b)$,

$$\begin{aligned}
\int_{x_s^-(b)-\bar{v}s}^{x_s^+(b)} \mathrm{d}x_0 \, \{\cdots\} &= \int_{x_l^-(b)}^{x_l^+(b)-\bar{v}s} \mathrm{d}x_0 \, \{\cdots\} \\
&\quad +2 \int_{x_l^+(b)-\bar{v}s}^{x_s^-(b)} \mathrm{d}x_0 \, \{\cdots\} + \phi_a(b) \qquad (126)
\end{aligned}$$

The final range of s to be considered is $s > t_s(b) + 2t_l(b)$. Now Equation (115)

can be written in the following illuminating form,

$$\begin{aligned}\int_{x_s^-(b)-\bar{v}s}^{x_s^+(b)} \mathrm{d}x_0 \{\cdots\} &= \int_{x_s^-(b)-\bar{v}s}^{x_s^+(b)-\bar{v}s} \mathrm{d}x_0 \{\cdots\} + \int_{x_s^+(b)-\bar{v}s}^{x_l^+(b)-\bar{v}s} \mathrm{d}x_0 \{\cdots\} \\ &+ \int_{x_l^+(b)-\bar{v}s}^{x_l^-(b)} \mathrm{d}x_0 \{\cdots\} + \int_{x_l^-(b)}^{x_s^-(b)} \mathrm{d}x_0 \{\cdots\} \\ &+ \int_{x_s^-(b)}^{x_s^+(b)} \mathrm{d}x_0 \{\cdots\}. \end{aligned} \tag{127}$$

Here the first and last terms should be looking very familiar. They encompass all the trajectories which end in or start from, respectively, the short range potential. They are equal and their sum is $\phi_A(b)$. Further, the second and fourth terms of this equation correspond to the second and fourth terms in Equation (122). They represent all trajectories which are represented in Figures 28 and 29. As was noted before these terms grow to a maximum contribution when $s = t_s(b) + 2t_l(b)$ and remain constant thereafter. Also, they are equal to each other at all values of s, being zero for $s \leq t_s(b) + t_l(b)$. For convenience define the following quantity,

$$\phi_s(b) \equiv \phi_a(b) + \left[2 \int_{x_l^+(b)-\bar{v}s}^{x_s^-(b)} \mathrm{d}x_0 \{\cdots\} \right]_{s=t_s(b)+2t_l(b)} \tag{128}$$

$\phi_s(b)$ is equal to the sum of the first, second, fourth, and last terms in Equation (127). That leaves the third term as the last one to be considered. This term contains all trajectories which pass entirely through the full range of the potential. As such, they will all accumulate the same value of $\theta(x_0, b, s)$. Define this value as,

$$\theta_{max} \equiv \theta_s(b) + 2\theta_l(b). \tag{129}$$

Since $\theta(x_0, b, s)$ is constant over this range terms involving it come outside of the

integral and we have,

$$\int_{x_l^+(b)-\bar{v}s}^{x_l^-(b)} \mathrm{d}x_0 \{\cdots\} = \{\cdots|_{\theta=\theta_{max}}\}\bar{v}(s-[t_s(b)+2t_l(b)]) \tag{130}$$

So for $s > t_s(b) + 2t_l(b)$ one can write,

$$\int_{x_s^-(b)-\bar{v}s}^{x_s^+(b)} \mathrm{d}x_0 \{\cdots\} = \phi_s(b) + \{\cdots|_{\theta=\theta_{max}}\}\bar{v}(s-[t_s(b)+2t_l(b)]). \tag{131}$$

Define the following quantity,

$$\phi_{II}(b) \equiv \phi_s(b) + \phi_l(b). \tag{132}$$

$\phi_{II}(b)$ represents all calculations which eventually become redundant, i.e. they become constant with time. The entire integral over x_0 in Case II may now be expressed as,

$$\begin{aligned}
\int_{-\infty}^{\infty} \mathrm{d}x_0 \{\cdots\} &= 2\int_{x_s^+(b)}^{x_l^+(b)} \mathrm{d}x_0 \{\cdots\} + (x_s^+(b) - x_s^-(b) + \bar{v}s), s < t_l(b) \\
&= \phi_l(b) + (x_s^+(b) - x_s^-(b) + \bar{v}s), t_l(b) \le s < t_s(b) \\
&= \int_{x_s^-(b)-\bar{v}(s-t_s(b))}^{x_s^-(b)} \mathrm{d}x_0 \{\cdots\} + \phi_a(b) + \phi_l(b), t_s(b) \le s < t_s(b) + t_l(b) \\
&= \int_{x_l^-(b)}^{x_l^+(b)-\bar{v}s} \mathrm{d}x_0 \{\cdots\} + 2\int_{x_l^+(b)-\bar{v}s}^{x_s^-(b)} \mathrm{d}x_0 \{\cdots\} + \phi_a(b) + \phi_l(b), \\
&\quad t_s(b) + t_l(b) \le s < t_s(b) + 2t_l(b) \\
&= \{\cdots|_{\theta=\theta_{max}}\}\bar{v}(s-[t_s(b)+2t_l(b)]) + \phi_{II}(b), \\
&\quad s \ge t_s(b) + 2t_l(b)
\end{aligned} \tag{133}$$

Since the integral over x_0 becomes linear in s when $s \ge t_s(b) + 2t_l(b)$ the time for

which the numerical calculations becomes redundant in case II is,

$$t_r(b) \equiv t_s(b) + 2t_l(b), b < r_s. \tag{134}$$

These results clearly show the linear dependence of $g(s)$ on s as $s \to \infty$. In this computational scheme $g(s)$ becomes linear when $s > \max\{t_r(b)\}$ where values of b from both Case I and Case II are considered.

4.2.3 Conclusions of the computational model.

The results contained in Equations (107) and (133) were modeled in C++ and tested extensively. I first tested my results against code that calculates $g(s)$ for a Lennard-Jones type potential. Then I compared my results for a square well against an analytic result reported in Allard [1978]. Finally, another code developed by Gorden Hager (private communication 2014) implements the AT model by first fitting the DP to a power series in inverse powers of R. A comparison of our two codes showed that we obtained the same results.

A comparison of run times showed that taking advantage of the spherical nature of the DP reduced the time of calculation by a half. Storing the results of the various ϕ's discussed above also resulted in significant time savings, though not quite as much as taking advantage of the symmetry. Another way to save time is to store the current valuse of $\theta(x_0, b, s_0)$. This way when one visits this point (x_0, b) again for a later value of $s = s_1$, the integration over time only has to be performed from s_0 to s_1 and added to the previously stored value instead of integrating all the way from 0 to s_1. One more significant optimization which was performed has to do with memory efficiency. If one codes up Equations (107) and (133) directly, then one first starts with a particular time $s = s_0$, then calculates $g(s_0)$. This means one must visit each unique point (x_0, b) on a two dimensional grid and then perform the integral over

time. As one increases the size of the grid by making the points more closely spaced, the memory requirements for storing all of the θ values becomes unmanageably large very quickly, certainly much earlier than the calculation will converge. The way that I resolved this was to swap the order of the loop over s and the loop over b. So the code first considers a given $b = b_0$, and then calculates that impact parameter's effect on $g(s)$ for all the values of s one wishes to consider. Thus, the θ's only need to be stored for that one b, and can be thrown away when moving on to the next impact parameter to consider. This reduces the two-dimensional array which stores θ to a one-dimensional array, effectively reducing the memory requirements to the square root of the memory needed for the two dimensional array.

The code is designed to take the values of r_s and r_l as parameters from the user. It is expected that if the value of r_s entered is too large than the model won't converge properly due to treating too big a region of the potential as rapidly changing. Thus, one can start with a large value of r_s and then slowly reduce it until the results converge. This is precisely what was observed in tests. It was also observed that as one further decreases $r_s \to 0$ from where it converged at first the results of the calculation don't change. A value of $r_s = 0$ is effectively like treating the whole problem in the context of case I. This means that numerically integrating straight through the inner region of the DP is perfectly accurate. Also, one would expect that a case II treatment would slightly improve run times as it handles certain parts of the integration analytically, however no slow down was noticed by doing everything with case I.

V. Results of the Anderson-Talman Model Calculations

In this chapter I use the AT theory, reviewed extensively by Allard and Kielkopf [1982], to compute the broadening(α) and shifting(β) coefficients, as well as the asymmetries, of the line shapes of K, Rb, and Cs perturbed by He, Ne, and Ar. This theory assumes that the dipole transition moment between states remains constant for the duration of each collision. The correction for the variance of the dipole moment with R used by the authors above is shown to only have a significant effect in the wings of the line profile, especially in the vicinity of any satellite features which occur in a region of the PEC where the dipole transition moment is changing appreciably. Thus, their theory and ours are effectively the same when considering only the Lorentzian line core. A theoretical understanding of the molecular potentials, including the effects of the spin-orbit interaction, is required for this approach to calculating the line profile. I use my own *ab initio* PECs (see Chapter III), which have been developed for this purpose, as input to the theory. I explore the temperature dependence of the coefficients and asymmetry over a range of $50K$ to $3000K$. The results are compared to other calculations which use the quantum theory due to Baranger and the same *ab initio* PECs. I also compare my results to other theoretical and experimental results where available.

5.1 Theory

The formulation of the non-degenerate semi-classical AT theory is reviewed in Allard and Kielkopf [1982] and extended to handle degenerate atomic levels by Allard et al. [1999, 1994]. We briefly summarize the theory here starting with the non-degenerate case where the line shape is given by $I(\omega, T)$, ω is the angular frequency measured from the unshifted line center, and T is the temperature. The inten-

sity, $I(\omega, T)$ is proportional to the Fourier transform of the autocorrelation function $\Phi(s, T)$,

$$I(\omega, T) = \int_{-\infty}^{\infty} \Phi(s, T) e^{i\omega s} ds \tag{135}$$

where,

$$\Phi(s, T) = \exp\{-ng(s, T)\}, \tag{136}$$

and,

$$g(s, T) = \int_{0}^{\infty} f(v, T) g(s, v)\, \mathrm{d}v \tag{137}$$

with,

$$\begin{aligned} g(s, v) &= 2\pi \int_{0}^{\infty} b\, \mathrm{d}b \int_{-\infty}^{\infty} \mathrm{d}x_0 \\ &\quad \times \left[1 - \exp\left\{-i \int_{0}^{s} \hbar^{-1} \Delta V[R(t)] \mathrm{d}t\right\}\right]. \end{aligned} \tag{138}$$

Here n is the number density of the perturbing gas, s is time, $f(v, T)$ is the Maxwell speed distribution, $\Delta V(R)$ is the difference potential (DP), and $R(t)$ is the time-dependent internuclear seperation and will be discussed further below. The DP is a function of internuclear separation, R, and is given by $\Delta V(R) = (V_i(R) - V_f(R)) - (E_i - E_f)$ where $V_i(R)$ and $V_f(R)$ are $M + Ng$ PECs. As $R \to \infty$, $V_i(R) \to E_i$ and $V_f(R) \to E_f$ where E_i and E_f are the initial and final atomic energies of the transition for which the line shape is being calculated.

The full integration used to compute $g(s, v)$ is performed over all space using cylindrical coordinates where the integral over the azimuthal angle yields the factor

of 2π in Equation (138). The emitter is stationary at the origin and the remaining integrations in Equation (138) are over impact parameter b and initial condition x_0 of a perturber with reduced mass μ of the $M + Ng$ pair. The perturber is assumed to move in a straight line with constant speed v in the positive x-direction, where $x = x_0 + vt$. The straight line trajectory together with the impact parameter, b, yields an internuclear separation given by $R(t) = (b^2 + (x_0 + vt)^2)^{1/2}$. Finally, an average over the Maxwell speed distribution, $f(v, T)$, is performed in Equation (137) to obtain $g(s, T)$ as a function of temperature. As an approximation to the average over speed, the integral in Equation (137) may be omitted and $g(s, v)$ may instead be evaluated at the average atomic speed $\bar{v}(T) = (8kT/\pi\mu)^{1/2}$ where k is Boltzmann's constant.

In the impact limit the number density of perturbers is low and $g(s, v)$ must be computed for sufficiently large s so that the autocorrelation function given by Equation (136) decays to zero. In the limit $s \to \infty$, $g(s, v) \to g_I(s, v)$ where $g_I(s, v)$ is a linear function of time,

$$g_I(s, v) = \{\alpha(v) + i\beta(v)\}s + \{\alpha_0(v) + i\beta_0(v)\}. \tag{139}$$

Either an average over speed or the substitution $v = \bar{v}(T)$ yields $g_I(s, T)$ and, through Equations (135) and (136), an analytic expression for the intensity,

$$I(\omega, T) \;=\; 2\exp(-n\alpha_0)\left(\frac{n\alpha\cos(-n\beta_0) - (\omega - n\beta)\sin(-n\beta_0)}{(\omega - n\beta)^2 + (n\alpha)^2}\right). \tag{140}$$

When $\alpha_0 = 0$ and $\beta_0 = 0$ the intensity in Equation (140) becomes Lorentzian with a half width at half max given by $n\alpha$ and a shift given by $n\beta$. In the impact limit, the broadening coefficient α and shifting coefficient β may be written explicitly as,

$$\alpha(v) = 2\pi v \int_0^\infty b\,\mathrm{d}b\,(1 - \cos\{\theta(v,b)\})\,, \tag{141}$$

and

$$\beta(v) = 2\pi v \int_0^\infty b\,\mathrm{d}b \sin\{\theta(v,b)\}\,, \tag{142}$$

where the accumulated phase $\theta(v,b)$ is given by,

$$\theta(v,b) = (\hbar v)^{-1} \int_{-\infty}^{\infty} \Delta V[(b^2 + x^2)^{1/2}]\mathrm{d}x. \tag{143}$$

In Equation (139), $\alpha_0(v)$ is the intercept of the real part of $g_I(s,v)$ and, as a scale factor for the total line shape in Equation (140), may be eliminated from consideration by rescaling the intensity. The asymmetry coefficient $\beta_0(v)$ is the intercept of the imaginary part of $g_I(s,v)$ and in Equation (140) parameterizes the line shape asymmetry. While expressions for $\alpha(v)$ and $\beta(v)$ in the impact limit are given by Equations (141) and (142), there is no corresponding impact limit expression for $\beta_0(v)$. To compute $\beta_0(v)$, the full integral for $g(s,v)$ in Equation (138) must be evaluated. For this reason, all calculations of the broadening, shifting, and asymmetry coefficients in this paper are performed using Equation (138) where a linear fit to $g(s,v)$ is performed in the limit $s \to \infty$. The slope of the linear fit to the real part of $g(s,v)$ is $\alpha(v)$ and the slope and intercept of the linear fit to the imaginary part of $g(s,v)$ are $\beta(v)$ and $\beta_0(v)$ respectively. Even though we use Equation (138) for all calculations, we are able interpret our results for $\alpha(v)$ and $\beta(v)$ using Equations (141) and (142) because we are evaluating $g(s,v)$ in the impact limit of large s.

For each $M + Ng$ pair there are four PECs, $V_{X^2\Sigma_{1/2}}(R)$, $V_{A^2\Pi_{1/2}}(R)$, $V_{A^2\Pi_{3/2}}(R)$, and $V_{B^2\Sigma_{1/2}}(R)$. As the internuclear separation $R \to \infty$, the ground $X^2\Sigma_{1/2}$ PEC correlates with the ground $^2\mathrm{S}_{1/2}$ alkali-metal atom energy level, the excited $A^2\Pi_{1/2}$

PEC correlates with the excited $^2P_{1/2}$ alkali-metal atom energy level, and the excited $A^2\Pi_{3/2}$ and $B^2\Sigma_{1/2}$ PECs correlate with the excited $^2P_{3/2}$ alkali-metal atom energy level. The four PECs of each $M + Ng$ pair are used to compute three DPs required by AT theory to calculate the D_1 and D_2 line shapes,

$$\begin{aligned}
\Delta V_{\Pi_{1/2}}(R) &= (V_{A^2\Pi_{1/2}} - V_{X^2\Sigma_{1/2}}) - E_{\mathrm{D1}} \\
\Delta V_{\Pi_{3/2}}(R) &= (V_{A^2\Pi_{3/2}} - V_{X^2\Sigma_{1/2}}) - E_{\mathrm{D2}} \\
\Delta V_{\Sigma_{1/2}}(R) &= (V_{B\Sigma_{1/2}} - V_{X^2\Sigma_{1/2}}) - E_{\mathrm{D2}}.
\end{aligned} \tag{144}$$

where E_{D1} and E_{D2} are the atomic alkali-metal atom D_1 and D_2 transition energies, subtracted so that $\Delta V \to 0$ as $R \to \infty$.

When non-adiabatic effects are neglected, the D_1 line shape in AT theory is determined by a single DP, $\Delta V_{\Pi_{1/2}}(R)$. The situation is more complicated for the D_2 line shape where two DPs, $\Delta V_{\Pi_{3/2}}(R)$ and $\Delta V_{\Sigma_{1/2}}(R)$, must both be considered when calculating the line shape. This is accomplished by modifying the autocorrelation function in Equation (136) to include a weighted sum [Allard et al., 1994] over $g_i(s,T)$, where $i = \Pi_{3/2}, \Sigma_{1/2}$ labels the DP used in Equation (138) to compute the corresponding $g_i(s,v)$,

$$\Phi(s,T) = \exp\left(-n\sum_i \pi_i g_i(s,T)\right). \tag{145}$$

To determine the weights, π_i, we make the approximation that the dipole transition moments are constant and equal to the asymptotic atomic value for the duration of each collision. This essentially reduces the dipole autocorrelation formulation of $g_i(s,v)$ discussed by Allard et al. [1999] to the AT expression in Equation (138), slightly modified to include a factor of $d_{\mathrm{PS}}/(2d_{\mathrm{PS}})$. Here the quantity d_{PS} is the

dipole matrix element between the $^2P_{3/2}$ and $^2S_{1/2}$ atomic states. This yields a weight $\pi_i = 1/2$ for each $g_i(s,T)$ used in Equation (138). As discussed by Allard et al. [1999] the approximation of constant dipole moment primarily influences the line wing and is not expected to significantly effect broadening, shifting and asymmetry coefficients of the line core.

5.2 Difference Potentials

The DPs in Equation (144) are calculated using $V_{X^2\Sigma_{1/2}}(R)$, $V_{A^2\Pi_{1/2}}(R)$, $V_{A^2\Pi_{3/2}}(R)$, and $V_{B^2\Sigma_{1/2}}(R)$ PECs [Blank et al., 2012] and are plotted in Figures 30-32. Each figure also contains an inset illustrating the asymptotic form of these curves. The variation between these 27 DPs, three for each of the nine $M + Ng$ pairs, provides a rich computational laboratory to study the relationship between PECs and spectral line shape as determined by AT theory. For all $M + Ng$ systems, DPs originating from either the $A^2\Pi_{1/2}$, $A^2\Pi_{3/2}$, or $B^2\Sigma^+_{1/2}$ PECs share the same qualitative features.

When considering the approach of a perturber from the asymptotic limit, the $\Delta V_{\Pi_{1/2}}$ DPs plotted in Figure 30 all slowly rise to a maximum of less than 40cm^{-1} before decreasing. These maxima are caused in part by a local maxima in the $A^2\Pi_{1/2}$ PECs together with the wells in the ground $X^2\Sigma^+_{1/2}$ PECs, both which occur at roughly the same R. As illustrated in Figure 31 the $\Delta V_{\Pi_{3/2}}$ DPs essentially decrease as R decreases from the asymptotic limit. This occurs because the onset of the deeper wells in the $A^2\Pi_{3/2}$ PECs offset the effect of the shallow wells in the $X^2\Sigma_{1/2}$ ground state PECs. However, because the onset of the $X^2\Sigma_{1/2}$ wells occurs at slightly larger R that the onset of the $A^2\Pi_{3/2}$, there is a very small maximum in the $\Delta V_{\Pi_{3/2}}$ DPs at $R \approx 8$Å as shown in the inset in Figure 31. The $\Delta V_{\Sigma_{1/2}}$ DPs are plotted in Figure 32 and are qualitatively similar to the $\Delta V_{\Pi_{1/2}}$ DPs shown in Figure 30, however, the maxima of the $\Delta V_{\Sigma_{1/2}}$ DPs occur at much higher energies and for smaller values of

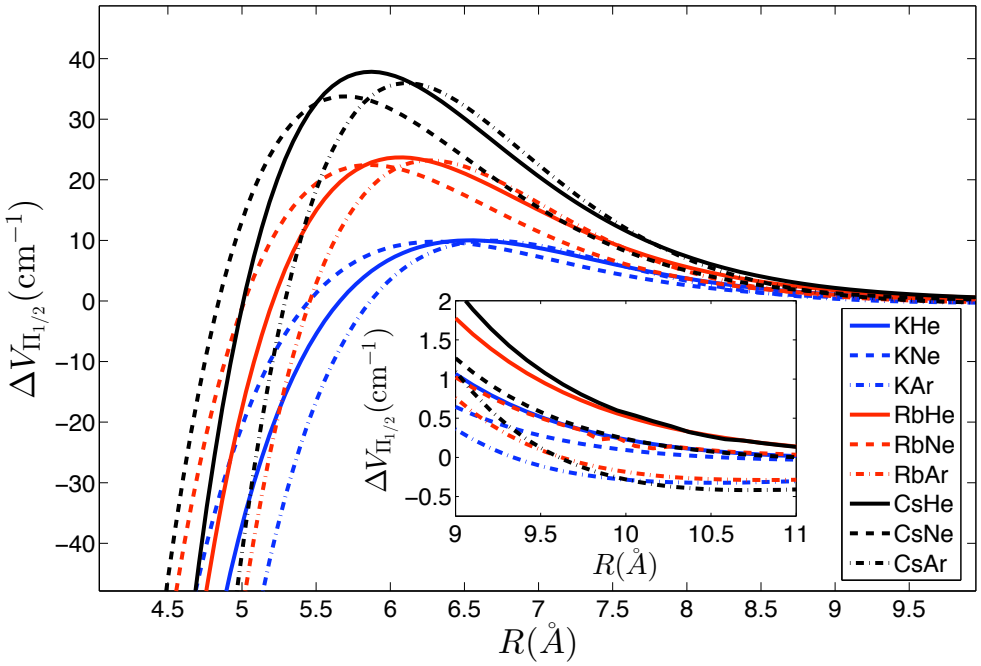

Figure 30. The $\Delta V_{\Pi_{1/2}}$ difference potentials for all $M + Ng$ combinations.

R than the maxima exhibited by the $\Delta V_{\Pi_{1/2}}$ DPs. These larger peaks in the $\Delta V_{\Sigma_{1/2}}$ DPs occur because the $V_{B^2\Sigma_{1/2}}$ PECs all exhibit a barrier as R decreases, followed by a shoulder at fairly high energies. It is the location and shape of these shoulders which give rise to the maxima seen in the $\Delta V_{\Sigma_{1/2}}$ DPs. The energies of these maxima correspond to the frequency, measured from line center, of satellite peaks [Blank et al., 2012] predicted to appear by the AT theory [Allard and Kielkopf, 1982]. At values of $R \approx 10$Å several of the $\Delta V_{\Sigma_{1/2}}$ DPs exhibit a very shallow well as shown by the inset in the Figure 32. These wells correspond to a very shallow well in the $B^2\Sigma^+_{1/2}$ PECs caused by diabatic coupling between the $A^2\Pi_{1/2}$ and $B^2\Sigma^+_{1/2}$ electronic states.

At values of $R \approx 3.0$Å all DPs in Figures 30-32 are decreasing in energy as R decreases. At even smaller values of $R \approx$ 1-2Å not shown in the figures, the DPs turn around and start to increase rapidly in energy with decreasing R.

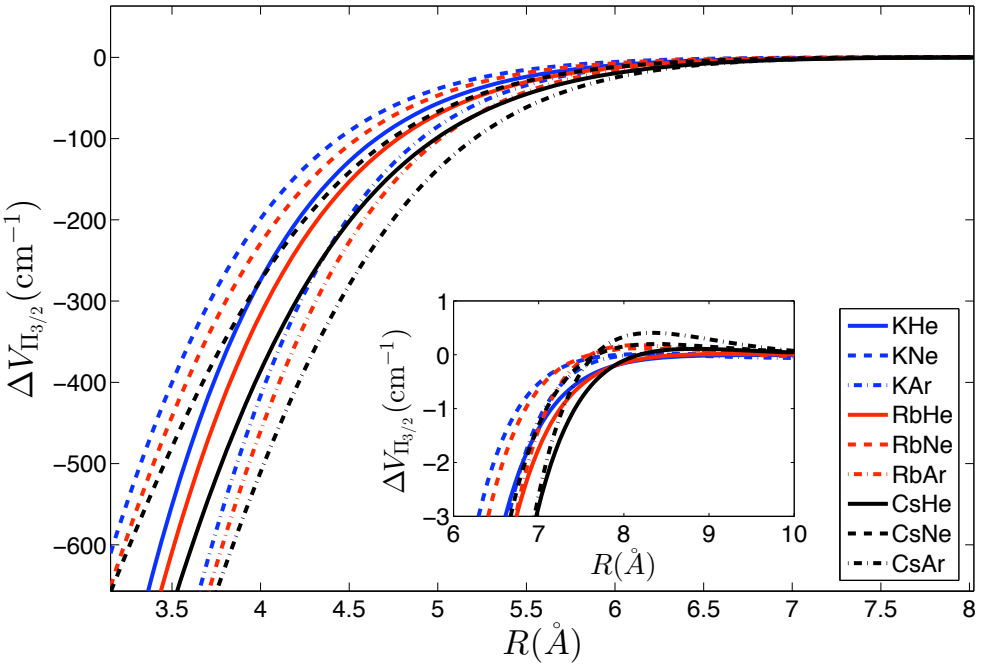

Figure 31. The $\Delta V_{\Pi_{3/2}}$ difference potentials for all $M + Ng$ combinations.

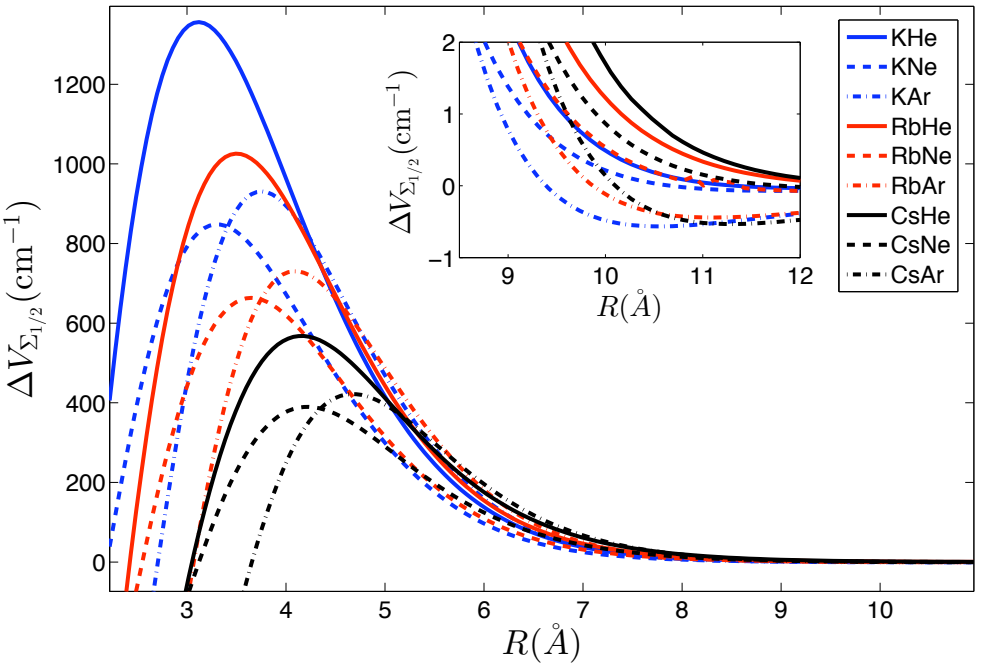

Figure 32. The $\Delta V_{\Sigma_{1/2}}$ difference potentials for all $M + Ng$ combinations.

5.3 Computational Details

The broadening $\alpha(T)$, shifting $\beta(T)$, and asymmetry $\beta_0(T)$, coefficients are calculated by numerically evaluating $g(s, v)$ in Equation (138). A linear fit to $g(s, v)$ is performed in the impact limit $s \to \infty$ where the slope of the real part of $g(s, v)$ is the broadening coefficient $\alpha(v)$, and the slope and intercept of the imaginary part of $g(s, v)$ are the shifting coefficient $\beta(v)$ and asymmetry coefficient $\beta_0(v)$, respectively. An average over the Maxwell speed distribution is performed to yield the coefficients as a function of temperature.

An analysis of the impact limit of $g(s, v)$ in Equation (138) used to compute $\alpha(v)$ and $\beta(v)$ can be performed by examining the integrands, $\alpha_{int}(v, b)$ and $\beta_{int}(v, b)$, of Equations (141) and (142),

$$\alpha_{int}(v, b) = b\left[1 - \cos\left\{\theta(v, b)\right\}\right], \tag{146}$$

and

$$\beta_{int}(v, b) = b \sin\left\{\theta(v, b)\right\}. \tag{147}$$

A plot of these integrands calculated using the Cs + He $\Delta V_{\Sigma_{1/2}}$ DP is shown in Figure 33 along with the $\Delta V_{\Sigma_{1/2}}$ DP and $\theta(v, b)$ as defined in Equation 143. The total area under the integrands yields α and β up to a factor of $2\pi v$. With the exception of the regions $b \approx 1.8\mathring{A}$ and $b \approx 3.75\mathring{A}$, the integrands rapidly oscillate with some average wavelength $\bar{\lambda}$ until $b = b_0$, where b_0 is defined by the largest value of b for which $\theta(v, b) = \pm\pi$. As b increases beyond b_0, α_{int} decays to zero, and β_{int} oscillates for one more quarter cycle and then decays to zero as well. The bounds on the oscillation amplitude for α_{int} are between 0 and $2b$, and and for β_{int} are between $-b$ and b. For values of the impact parameter in the range $0 \leq b \leq b_0$, $\bar{\lambda}$ is large and $\theta(v, b) \sim \bar{\lambda} b$.

In the limit of large $\bar{\lambda}$ over this range of b, $\int b\,\mathrm{d}b\cos(\bar{\lambda}b) \to 0$ and $\int b\,\mathrm{d}b\sin(\bar{\lambda}b) \to 0$. As a result, when Equations (146) and (147) are integrated from $b = 0$ to $b = b_0$ the area under α_{int} is approximately $b_0^2/2$ and the area under β_{int} is approximately zero. As illustrated in Figure 34, the impact parameter $b = b_0$ can therefore be used with Equations (141) and (142) to define an effective hard sphere contribution to the broadening and shifting coefficients,

$$\begin{aligned} \alpha_{hs}(v, b_0) &= 2\pi v \int_0^{b_0} b\,\mathrm{d}b\,[1 - \cos\{\theta(v, b)\}] \\ &\approx v\pi b_0^2 \end{aligned} \tag{148}$$

and,

$$\begin{aligned} \beta_{hs}(v, b_0) &= 2\pi v \int_0^{b_0} b\,\mathrm{d}b\ sin\{\theta(v, b)\} \\ &\approx 0. \end{aligned} \tag{149}$$

The broadening and shifting coefficients given by Equations (141) and (142) may then be re-expressed as the sum of this effective hard sphere contribution together with a long range correction,

$$\begin{aligned} \alpha(v) &= \alpha_{hs} + \alpha_{lr} \\ \beta(v) &= \beta_{hs} + \beta_{lr} \end{aligned} \tag{150}$$

where the long range corrections are given by,

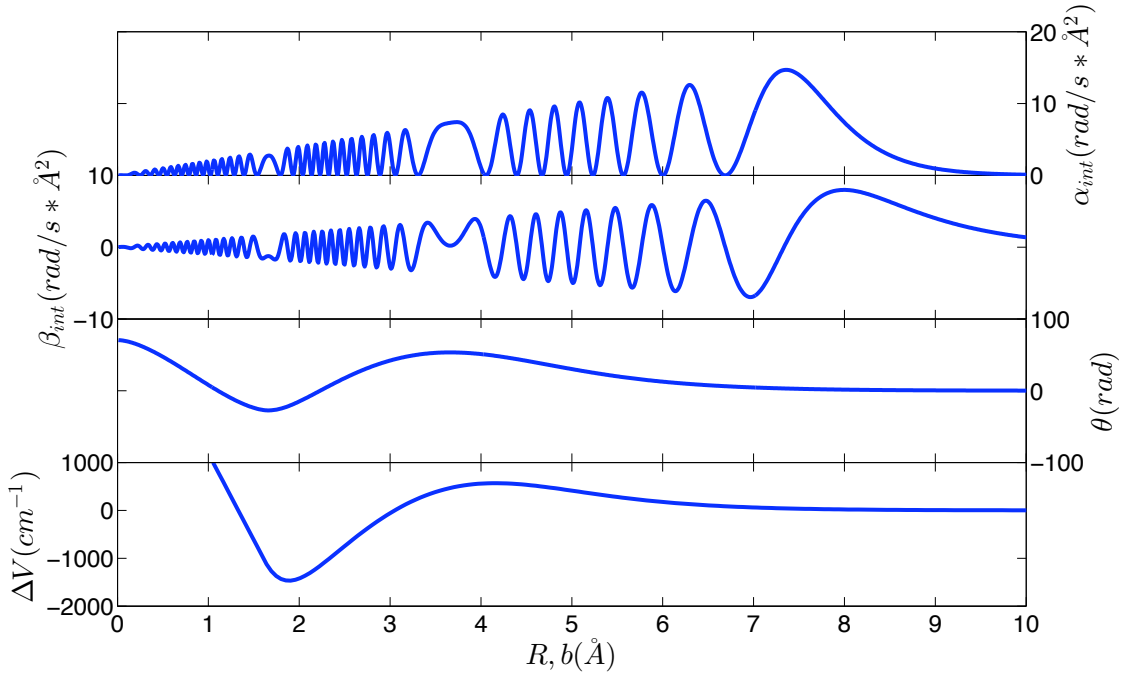

Figure 33. The Cs + He $\Delta V_{\Sigma_{1/2}}$ difference potential is plotted along with the corresponding integrands α_{int} and β_{int} given by Eqs. (146),(147), and $\theta(v,b)$ given by Eq. (143) calculated at $\bar{v}(\mathrm{T} = 500\mathrm{K})$. Note that *ab initio* calculations were not performed for $R < 1.6$Å and the Cs + He $\Delta V_{\Sigma_{1/2}}$ DP is linearly extended for values of $R < 1.6$Å.

$$\alpha_{lr}(v, b_0) = 2\pi v \int_{b_0}^{\infty} b\,\mathrm{d}b\,[1 - \cos\{\theta(v,b)\}]\,, \tag{151}$$

and

$$\beta_{lr}(v, b_0) = 2\pi v \int_{b_0}^{\infty} b\,\mathrm{d}b\ sin\{\theta(v,b)\}\,. \tag{152}$$

Values of the impact parameter in Equations (148) and (149) for which $b < b_0$ correspond to straight line trajectories that explore the short range region of the DPs. Any variability in the short range DPs, and by extension the short range PECs, will not significantly alter the rapid oscillations of α_{int} and β_{int} for impact parameters $0 \leq b \leq b_0$. As a result, the effective hard sphere broadening contribution given by $\alpha_{hs} \approx v\pi b_0^2$ in Equation (148) is sensitive to the PECs only through the value of b_0,

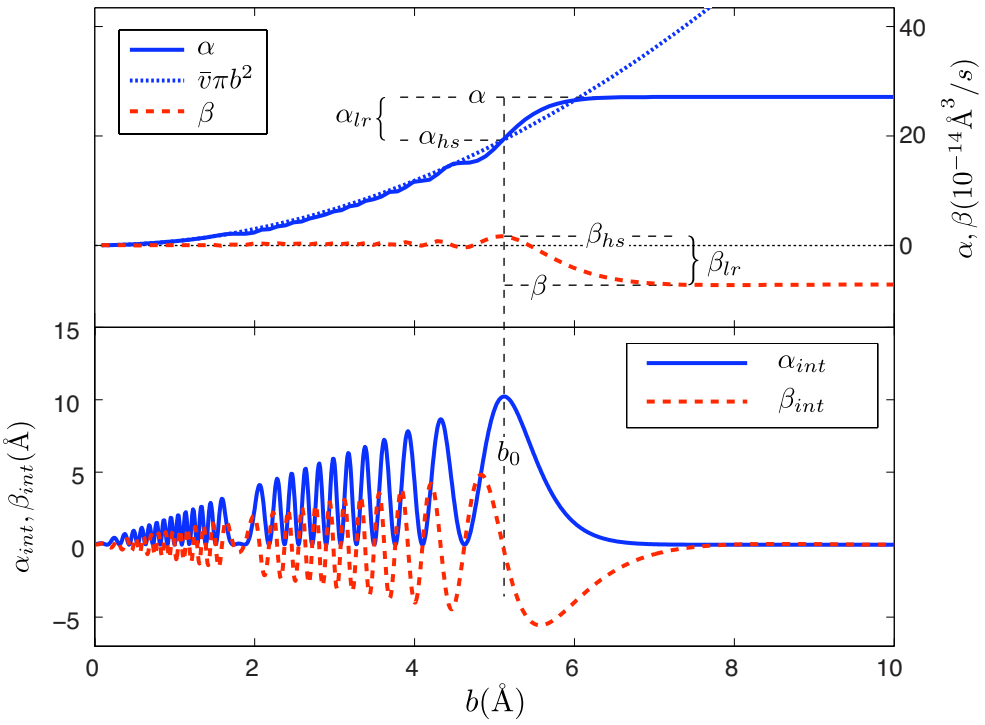

Figure 34. Integrands α_{int} and β_{int} given by Eqs. (146) and (147) computed using the Cs + He $\Delta V_{\Pi_{3/2}}$ DP at $\bar{v}(\mathrm{T} = 1000\mathrm{K})$ are plotted on the bottom. The integrals $2\pi\bar{v}\int_0^b \mathrm{d}b'\,\alpha_{int}(b')$ and $2\pi\bar{v}\int_0^b \mathrm{d}b'\,\beta_{int}(b')$ are plotted on the top and closely follow the effective hard sphere value until $b = b_0$.

and both broadening and shifting coefficients given by Equations (148) and (149) are not sensitive to the details of the short range PECs for $R < b_0$.

Values of the impact parameter in Equations (151) and (152) for which $b > b_0$ correspond to straight line trajectories that sample the asymptotic region of the DPs. The long range contributions to the broadening and shifting coefficients given by Equations (151) and (152) are therefore sensitive to the DPs, and by extension the PECs, through the value of b_0. Because $\theta(v, b)$ does not rapidly oscillate for $b > b_0$, both $\alpha_{lr}(v, b_0)$ and $\beta_{lr}(v, b_0)$ are also sensitive to the details of the long range PECs for $R > b_0$. In this long range region, $\alpha_{int}(v, b)$ will approach zero as a quadratic function of $\theta(v, b)$ while $\beta_{int}(v, b)$ will approach zero as a linear function of $\theta(v, b)$. As a result $\alpha_{lr}(v, b_0)$ is less sensitive to the long range PECs than $\beta_{lr}(v, b_0)$.

The broadening coefficient $\alpha(v)$ given by Equation (150) is therefore determined in large part by an effective hard sphere term α_{hs} that is sensitive to the PECs through the value of b_0, together with a long range correction term α_{lr} that is sensitive to the long range details of the PECs through α_{int}, where α_{int} decays quadratically with $\theta(v, b)$ to zero. In contrast, the shifting coefficient $\beta(v)$ given by Equation (150) is determined almost entirely by the long range term β_{lr} and is therefore more sensitive to the long range details of the PECs through β_{int}, where β_{int} decays linearly with $\theta(v, b)$ to zero. This lower sensitivity of $\alpha(v)$ to the details of the PECs yields general agreement between broadening coefficients calculated using different $M + Ng$ PECs and general agreement with experimental observation. In contrast, the shifting coefficient is more sensitive to the details of the long range PECs where a difference of less than a wave number over $10 - 20$Å can significantly change the value obtained for $\beta(v)$ and may even change the sign of the shifting coefficient. As a result, there can be significant disagreement between various calculations and experimental observations of the shifting coefficient.

This sensitivity of the shifting coefficient to the long range PECs is also expected to be present in the dipole autocorrelation formulation [Allard et al., 1999] where the dipole autocorrelation formulation essentially reduces to AT theory in the line core. An increased sensitivity of the shifting coefficient to the long range PECs compared to the broadening coefficient appears in the full quantum mechanical Baranger theory [Baranger, 1958] as well through the cosine and sine terms in Equations (141) and (142) where $\theta(v,b)$ is replaced by $\theta(E,J) = \phi_i(E,J) - \phi_f(E,J)$. In Baranger theory the $\phi_i(E,J)$ and $\phi_f(E,J)$ are scattering phase shifts computed using the $V_i(R)$ and $V_j(R)$ PECs and are functions of kinetic energy, E, and total angular momentum, J [Loper, 2013, Loper and Weeks, in preparation].

It is interesting to note that the rapid oscillation of α_{int} and β_{int} in Figure 33 is interrupted at impact parameters $b \approx 1.8\mathring{A}$ and $b \approx 3.75\mathring{A}$. These windows of interruption occur at values of b_i where $\theta(v,b_i) = \theta_i$ is an extremum, and the width of the window depends on how rapidly $\theta(v,b)$ varies in the vicinity of the i^{th} extremum. The area under the window of interruption depends on this width and on the value of θ_i. The integrands, α_{int} and β_{int}, shown in Figure 33 are calculated using a mean speed $\bar{v}(T) = (8kT/\pi\mu)^{1/2}$ corresponding to a temperature $T = 500K$. The speed dependence enters the calculation of the integrands through the v^{-1} term in Equation (143). An increase in $v(T)$ will therefore reduce the overall amplitude of $\theta(v,b)$ causing the θ_i to decrease. As illustrated in Figure 35, when θ_i changes value, α_{int} and β_{int} will oscillate into and out of these windows of interruption and cause the total area under α_{int} and β_{int} to oscillate. These oscillations are illustrated in Figure 36 as a function of T for the Cs + He $B^2\Sigma^+_{1/2}$ DP where the approximation $v = \bar{v}$ is made. The oscillations are eliminated when the approximation $v = \bar{v}$ is replaced by an average over the Maxwell speed distribution. As illustrated in Figure 36, the average result can substantially differ from the $v = \bar{v}$ approximation at higher temperatures.

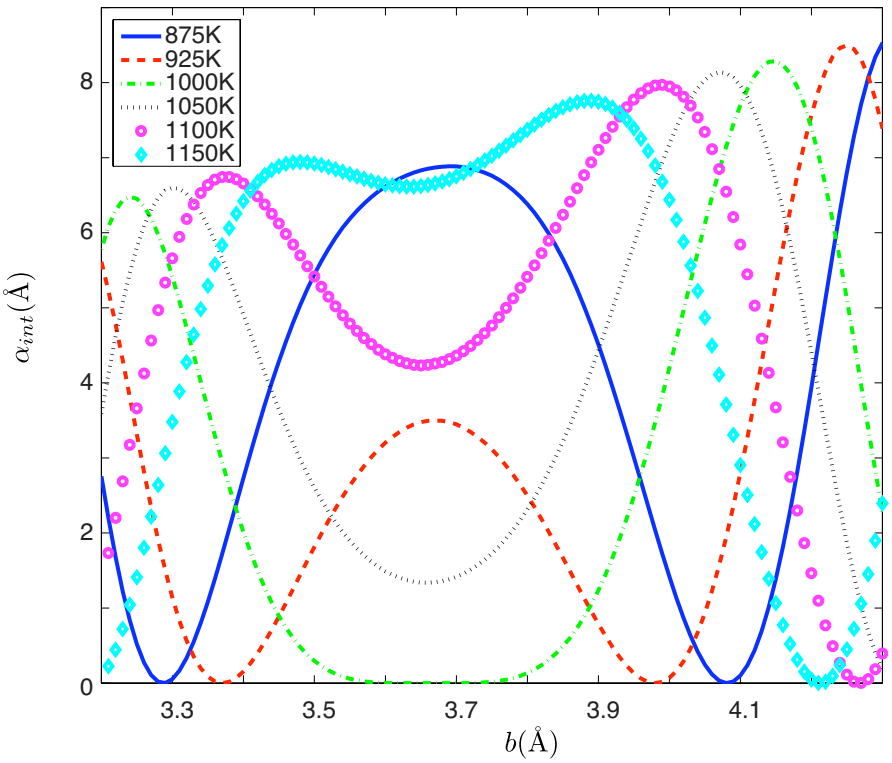

Figure 35. The integrand α_{int} given by Eq. (146) is computed using the Cs+He $\Delta V_{\Sigma_{1/2}}$ DP for several different values of $\bar{v}$(T) and corresponds to the window of interruption at $b \approx 3.75\AA$ in Fig. 33.

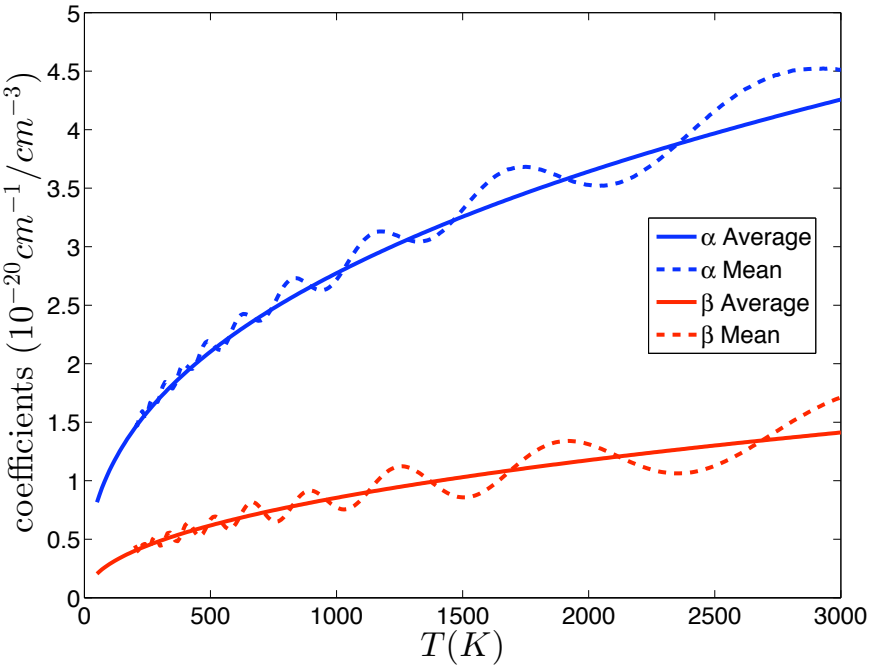

Figure 36. Broadening and shifting coefficients computed using the Cs + He $\Delta V_{\Sigma_{1/2}}$ DP. The α average and β average results are an average over the Maxwell speed distribution while the α mean and β mean results are computed using $\bar{v}$(T). One cycle of the oscillation of α mean about α average begins with a local maximum at T=875K, followed by a local minimum at T=1000K, and ends with a local maximum at T=1150K, and corresponds to the oscillations of α_{int} into and then back out of the window of interruption in Fig. 35.

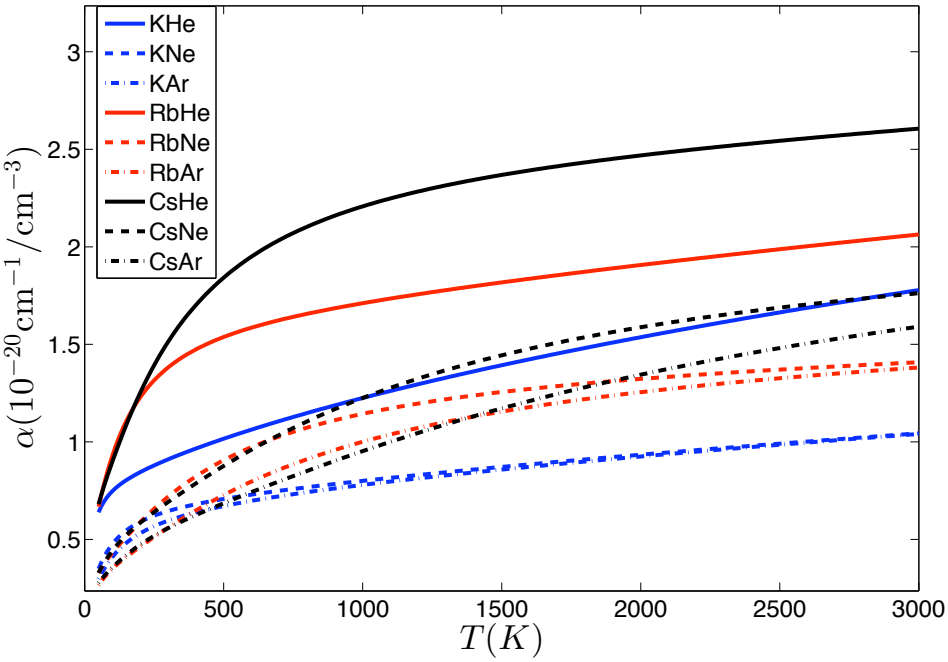

Figure 37. Predicted broadening (half-width) coefficients for the D1 line of all $M + Ng$ combinations.

5.4 Results

The temperature dependence of the broadening coefficients for the D_1 and D_2 alkali-metal atom line shapes of all $M + Ng$ combinations is plotted in Figures 37 and (38), respectively, over a range of $T = 50 - 3000K$. These figures show that the broadening coefficient for the $M+Ng$ pairs is roughly grouped according to noble-gas atom, with M + He combinations showing the most broadening, followed by M + Ne and then M + Ar. A strong dependence on noble-gas atom is clearest for the D_2 broadening coefficients, where the argon, neon, and helium groups exhibit no overlap, and is also evident to a lesser degree for the D_1 curves. This trend occurs because the average over speed in Equation (137) is weighted in favor of $\alpha(v)$ in Equation (141) for which v is inversely proportional to the square root of the reduced mass.

The relationship between DPs and the broadening coefficient $\alpha(T)$ as determined

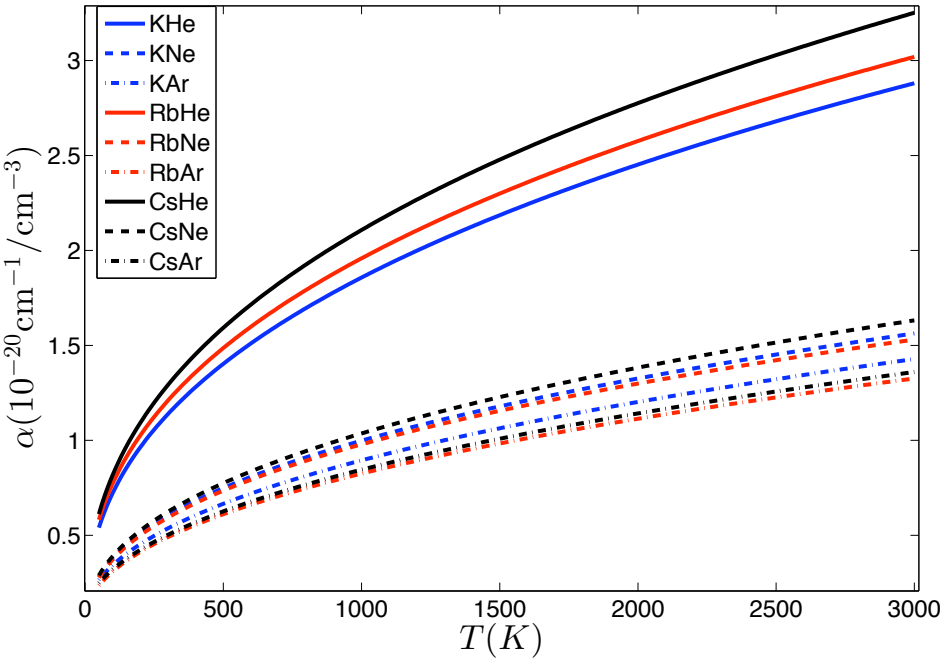

Figure 38. Predicted broadening (half-width) coefficients for the D2 line of all $M + Ng$ combinations.

by AT theory is explored in Figure 39. The value of $R = b_0$ at which the DPs in Figure 39 exhibit sufficient amplitude for $\theta(v, b_0) = \pm\pi$ defines the effective hard sphere contribution to $\alpha(T)$. As R decreases from the asymptotic limit in Figure 39, the $B^2\Sigma^+_{1/2}$ DP is the first to depart from zero and reach a value for which $\theta(v, b_0) = \pm\pi$. This is followed at a smaller value of $R = b_0$ for the $A^2\Pi_{1/2}$ DP, and then finally the $A^2\Pi_{3/2}$ DP. The effective hard sphere contribution to the broadening coefficients, $\alpha_{hs} = v\pi b_0^2$, is therefore largest for $\Delta V_{\Sigma_{1/2}}(R)$ followed by$\Delta V_{\Pi_{1/2}}(R)$, and then $\Delta V_{\Pi_{3/2}}(R)$, and the broadening coefficients $\alpha(T)$ exhibit the same ordering as shown in Figure 39.

As mentioned in the previous section, an increase in v will reduce the overall amplitude of $\theta(v, b)$ in Equation (143), and thereby lower the value of $b = b_0$ for which $\theta(v, b_0) = \pm\pi$. The rate at which b_0, and by extension α_{hs}, changes is also a function of the DP. As seen in Figure 40, $b_0 \approx 7.2$Å at 100K, and as seen in

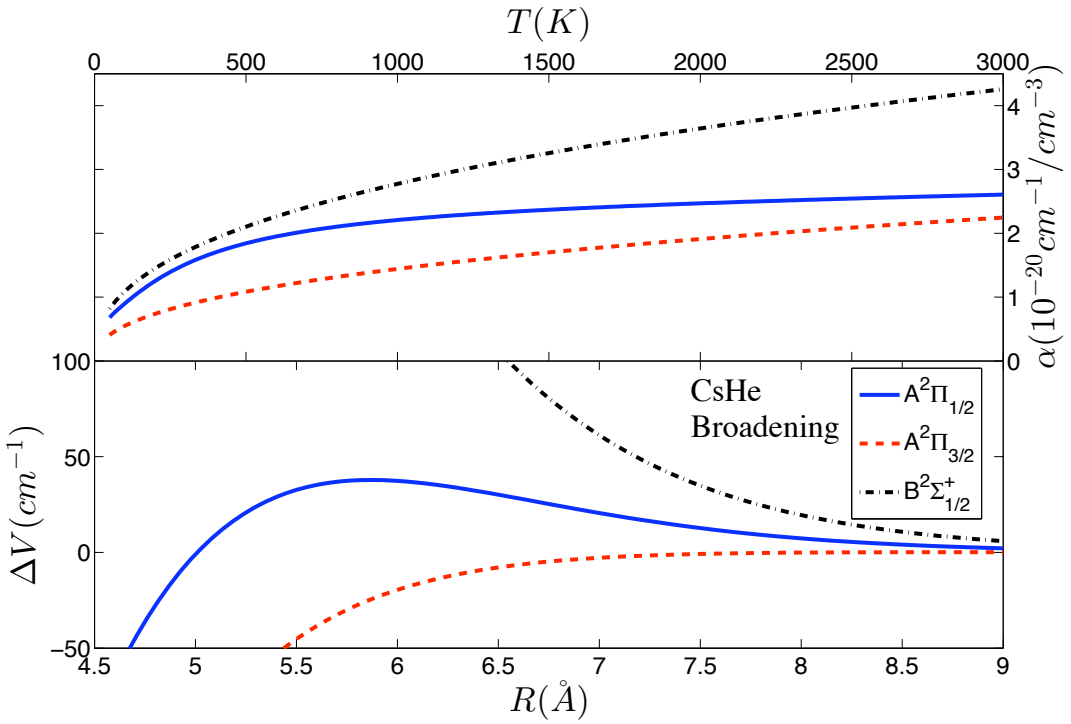

Figure 39. The Cs + He $\Delta V_{\Pi_{1/2}}$, $\Delta V_{\Pi_{3/2}}$, and $\Delta V_{\Sigma_{1/2}}$ DPs are plotted on the bottom and the corresponding broadening coefficients α(T) are plotted on the top. The $A^2\Pi_{3/2}$ and $B^2\Sigma^+_{1/2}$ broadening coefficients are plotted here separately. Their weighted average in Eq. (145) is used to compute the D2 broadening coefficient.

Figure 39 the $\Delta V_{\Pi_{1/2}}$ DP is similar to the $\Delta V_{\Sigma_{1/2}}$ DP near $R \approx 7.2$Å where they are both monotonically decreasing functions of R. As a result, values of α_{hs} computed using $\Delta V_{\Pi_{1/2}}$ will be similar at lower temperatures to values of α_{hs} computed using $\Delta V_{\Sigma_{1/2}}$. At a higher temperature $T = 2000$K, $b_0 \approx 4.1$Å in Figure 40, and as seen in Figure 39 the $\Delta V_{\Pi_{1/2}}$ DP is similar to the $\Delta V_{\Pi_{3/2}}$ DP near $R \approx 4.1$Å where they are both monotonically increasing functions of R. As a result, values of α_{hs} computed using $\Delta V_{\Pi_{1/2}}$ will be similar at higher temperatures to values of α_{hs} computed using $\Delta V_{\Pi_{3/2}}$. This behavior is seen in Figure 39 where the $A^2\Pi_{1/2}$ broadening coefficient closely follows the $B^2\Sigma_{1/2}$ broadening coefficient at low temperatures and crosses over at higher temperatures to follow the $A^2\Pi_{3/2}$ broadening coefficient.

The D_1 and D_2 broadening coefficients plotted in Figures 37 and 38) are smooth, monotonically increasing functions of temperature and are fit by a power law given

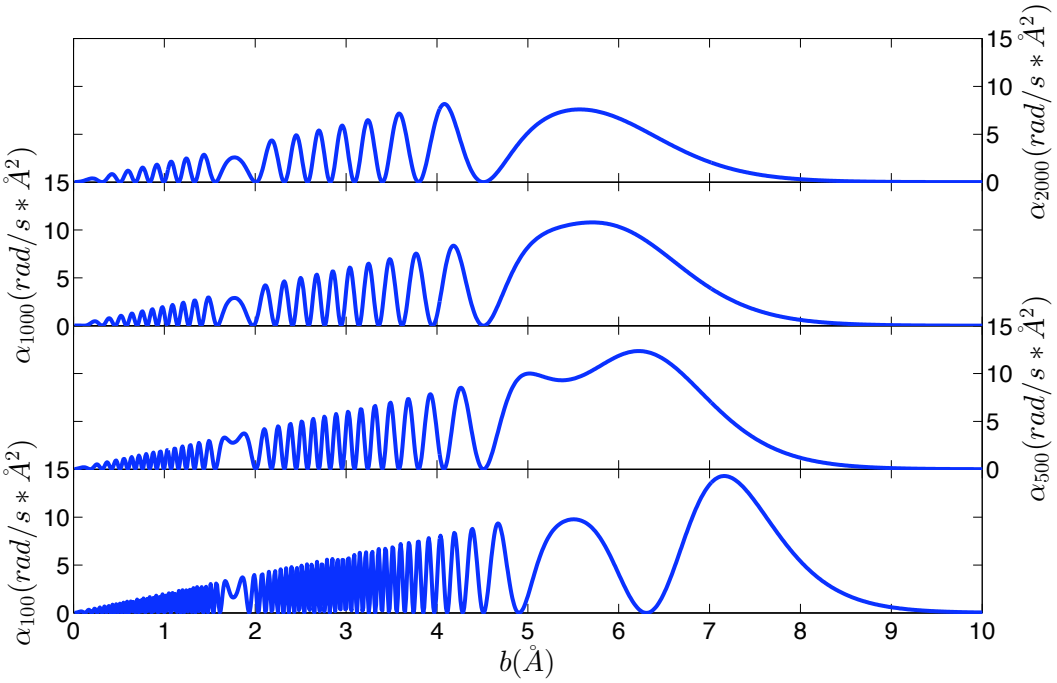

Figure 40. The integrand $\alpha_{int}(v,b)$ given by Eq. (146) is calculated using the Cs + He $A^2\Pi_{1/2}$ DP and plotted for several different temperatures. As the temperature increases from 100K in the bottom panel to 2000K in the top panel, the value of b_0 drops from 7.2Å down to 4.1Å. As b_0 decreases it crosses through a window of interruption corresponding to the maximum in $\Delta V_{\Pi_{1/2}}$ at R=5.9Å and becomes somewhat ambiguous at 1000K.

by cT^d with fit parameters c and d listed in Table 12. The D_2 broadening coefficients are given by the weighted average of the $A^2\Pi_{3/2}$ and $B^2\Sigma^+_{1/2}$ broadening coefficients in Equation (145) and are fit to cT^d with residuals that differ from unity by less than 10^{-4} in all cases. This suggests that the $A^2\Pi_{3/2}$ and $B^2\Sigma^+_{1/2}$ broadening coefficients may be individually fit to cT^d with the same power d. This was verified for all $M+Ng$ pairs, where the value of d for the $A^2\Pi_{3/2}$ and $B^2\Sigma^+_{1/2}$ broadening coefficients are essentially identical to the D_2 values of d listed in Table 12. The values of the parameter c for the $A^2\Pi_{3/2}$ broadening coefficients are smaller than the values of c for the $B^2\Sigma^+_{1/2}$ broadening coefficients as seen in Figure 39 for Cs + He. Note that the residuals listed in Table 12 for the D_1 fit are smaller than those for the D_2 fit. This is caused by the crossover of the $A^2\Pi_{1/2}$ broadening coefficients from $B^2\Sigma^+_{1/2}$ behavior at low temperature to $A^2\Pi_{3/2}$ behavior at high temperature as shown in Figure 39 for Cs + He. Note also that the broadening coefficients all have a temperature dependence of $T^{d<1/2}$. If the temperature dependence of the broadening coefficient was solely due to the v term in front of the integral over impact parameter in Equation (141) then $\alpha(T)$ would be proportional to $T^{d=1/2}$. It is the v^{-1} term in front of the integral for $\theta(b,v)$ in Equation (143) that gives rise to this reduced value of $d < 1/2$.

The temperature dependence of the shifting coefficients for the D_1 and D_2 line shapes of all $M+Ng$ combinations is shown in Figures 41 and 42, respectively. The shifting coefficients are grouped according to noble-gas atom, with the helium curves being the highest, followed by neon, and then finally argon. As with the broadening coefficients, this trend occurs because the average over speed in Equation (137) is weighted in favor of $\beta(v)$ in Equation (142) for which v is inversely proportional to the square root of the reduced mass. As illustrated in Figure 41, the M + He and M + Ne D_1 shifting coefficients are all positive over the entire temperature range, while the M + Ar D_1 shifting coefficients are all negative for small T and then all

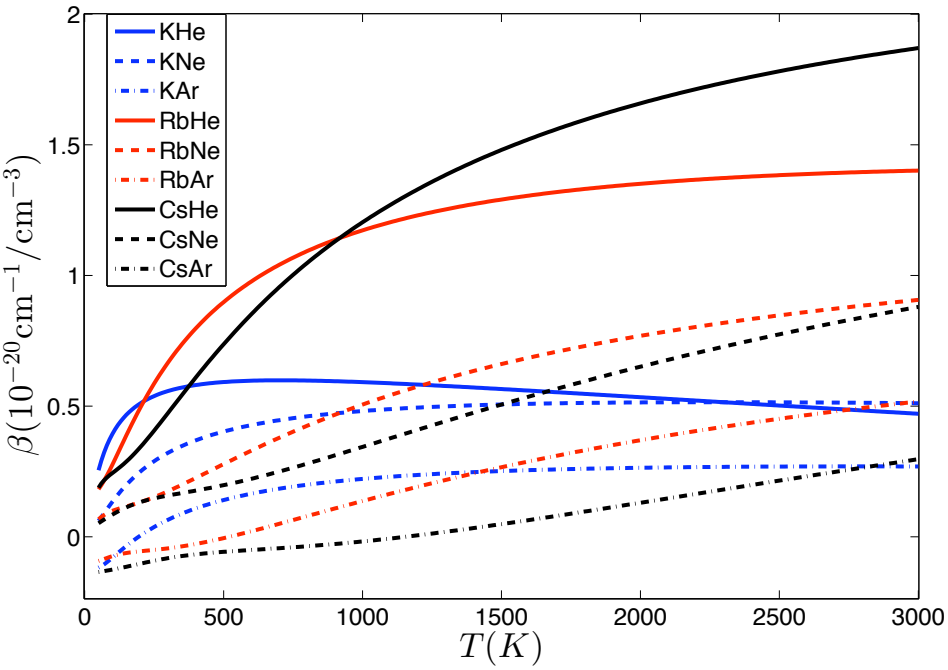

Figure 41. Predicted shifting coefficients for the D1 line of all $M + Ng$ combinations.

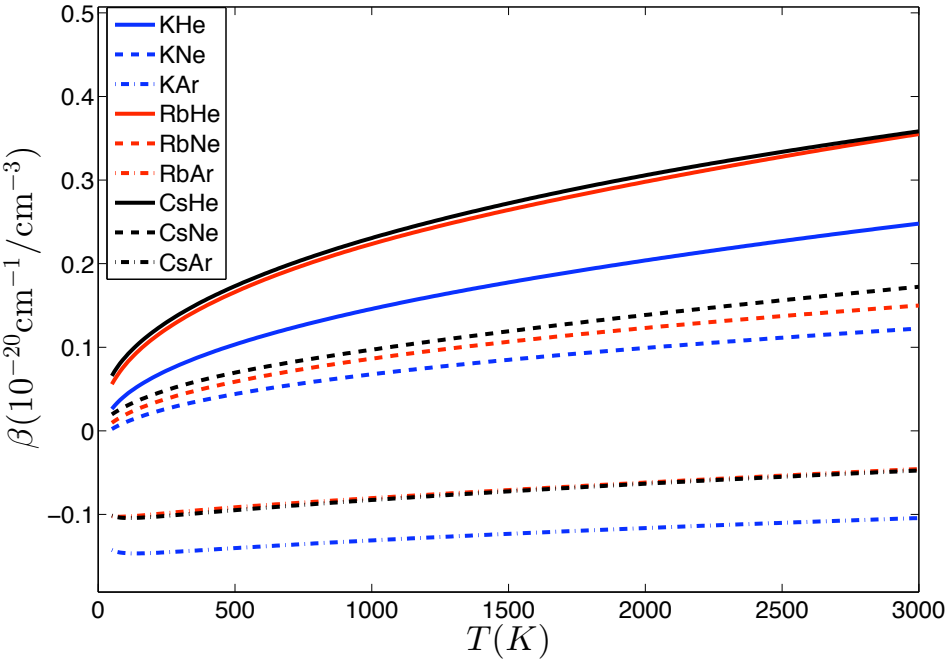

Figure 42. Predicted shifting coefficients for the D2 line of all $M + Ng$ combinations.

Table 12. Results of fitting the broadening coefficients to a functional from of cT^d where T is in Kelvin and the broadening coefficients are in $10^{-20}cm^{-1}/cm^{-3}$. These expressions are valid for temperatures ranging from $50 - 3000K$.

	D1			D2		
M+Ng	c	d	Residual	c	d	Residual
KHe	0.1669	0.2924	0.9873	0.1150	0.4025	1.0000
KNe	0.1802	0.2173	0.9925	0.05803	0.4116	1.0000
KAr	0.1383	0.2507	0.9954	0.04767	0.4246	1.0000
RbHe	0.4631	0.1871	0.9717	0.1262	0.3968	1.0000
RbNe	0.1574	0.2796	0.9594	0.05735	0.4104	1.0000
RbAr	0.07604	0.3674	0.9840	0.04188	0.4316	1.0000
CsHe	0.4114	0.2359	0.9437	0.1329	0.3997	0.9999
CsNe	0.08034	0.3907	0.9902	0.05813	0.4168	1.0000
CsAr	0.03828	0.467	0.9988	0.04299	0.4314	1.0000

become positive as T increases. It is interesting to note that the K + He D_1 shifting coefficient in Figure 41 exhibits a maximum at T≈ 750K and then decreases as the temperature increases, and both the K + Ne and K + Ar shifting coefficients increase with temperature until T≈ 2000k where they become constant. In Figure 42, the M + He and M + Ne D_2 shifting coefficients are also all positive over the entire temperature range while the M + Ar shifting coefficients are all negative over the entire temperature range.

The relationship between DPs and the shifting coefficient $\beta(T)$ as determined by AT theory is explored in Figure 43 where it is observed that the $A^2\Pi_{1/2}$ and $B^2\Sigma^+_{1/2}$ shifts are always positive over the range of T considered while the $A^2\Pi_{3/2}$ shifts are always negative. At lower temperatures the sign of the shifting coefficient correlates with the sign of the DP at $R = b_0$, where for $R > 5$Å, $\Delta V_{\Pi_{1/2}}$ and $\Delta V_{\Sigma 1/2}$ are both positive, while $\Delta V_{\Pi_{3/2}}$ is negative. At higher temperatures, larger values of $\bar{v}(T)$ will lower $\theta(v, b)$ and decrease the value of $b = b_0$. At $b_0 \approx 5$Å some fraction of the straight line trajectories in Equation (143) will begin to explore regions for which $\Delta V_{\Pi_{1/2}}$ is negative. This reduces the rate at which the D_1 shifting coefficient increases and, as seen in Figure 43, this occurs at a temperature of T≈ 1000K.

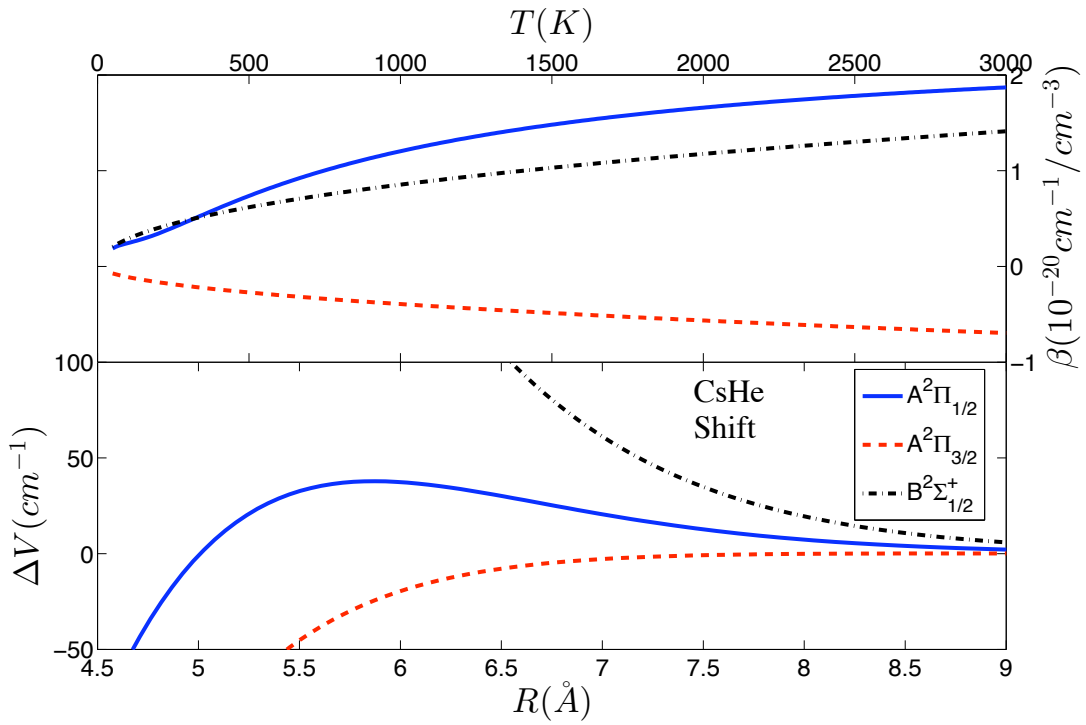

Figure 43. The Cs + He $\Delta V_{\Pi_{1/2}}$, $\Delta V_{\Pi_{3/2}}$, and $\Delta V_{\Sigma_{1/2}}$ DPs are plotted on the bottom and the corresponding shifting coefficients β(T) are plotted on the top. The $A^2\Pi_{3/2}$ and $B^2\Sigma^+_{1/2}$ shifting coefficients are plotted here separately. Their weighted average in Eq. (145) is used to compute the D2 shifting coefficient.

As the mass of the alkali-metal atom in the $M + Ng$ pair decreases, the maximum of the $\Delta V_{\Pi_{1/2}}$ peak in Figure 30 is observed to decrease. At a fixed temperature and speed, a lower peak height will correspond to a smaller value of b_0 as defined by $\theta(v, b) = \pm\pi$ using Equation (143). As a result, b_0 will be smallest for K + Ng followed by b_0 for Rb + Ng and then Cs + Ng. For a fixed temperature, the speed will increase as the reduced mass decreases and b_0 will therefor be smallest for K + He, followed by b_0 for K + Ne and then K + Ar. As a result, the straight line trajectories parameterized by $b \gtrsim b_0$ in Equation (142) will explore regions for which $\Delta V_{\Pi_{1/2}}$ is negative at lower temperatures for K + Ng compared to Cs + Ng and Rb + Ng. This causes the K + He D_1 shifting coefficient in Figure 41 to exhibit a maximum at T$\approx$ 750K and then decrease as the temperature increases, and causes both the K + Ne and K + Ar shifting coefficients to increase with temperature until T$\approx$ 2000k where they become constant. Similar behavior for Rb + Ng and Cs + Ng is expected at higher temperatures.

It is interesting to note that the M + Ar $B^2\Sigma^+_{1/2}$ DPs shown in the inset of Figure 32 all exhibit very shallow wells with depths that are on the order of 0.5 cm^{-1}. At temperatures below $T \approx 1500K$ the value of b_0 is sufficiently large so that a majority of trajectories used to compute β_{lr} sample this negative region of the DP. As a result, the $B^2\Sigma^+_{1/2}$ shifting coefficients shown in Figure 44 are negative for T$<$ 1500K, and illustrate the extreme sensitivity of the shifting coefficients to the long range features of the DPs for $R > b_0$. At higher temperatures T $>$ 1500K, the value of b_0 becomes sufficiently small so that more trajectories used to compute β_{lr} sample the positive region of the DP and $\beta(T)$ becomes positive. Similar behavior is observed for the M + Ar D_1 shifting coefficients in Figure 41 where the negative shifting coefficients at lower temperatures correspond to the shallow well in the M + Ar $\Delta V_{\Pi_{1/2}}$ DPs shown in the inset in Figure 30.

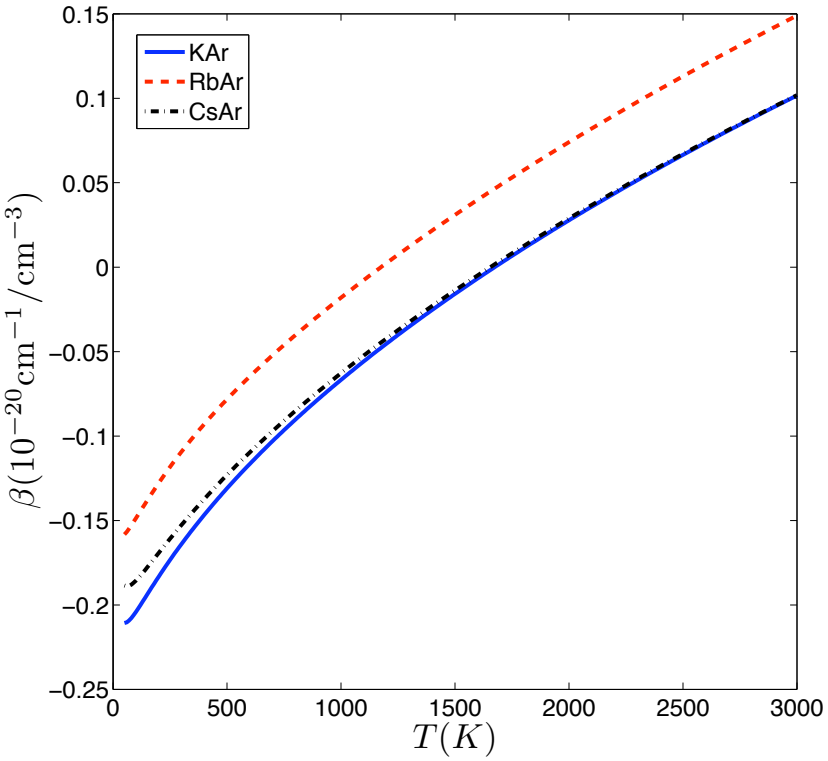

Figure 44. The shifting coefficient $\beta(T)$ computed using the M+Ar $\Delta V_{\Sigma_{1/2}}$ DPs. Negative values of $\beta(T)$ are caused by a very shallow well, approximately 0.5 cm^{-1} deep, in the $\Delta V_{\Sigma_{1/2}}$ DPs shown in the inset in Fig. 32 and illustrate the sensitivity of the shifting coefficients to the PECs.

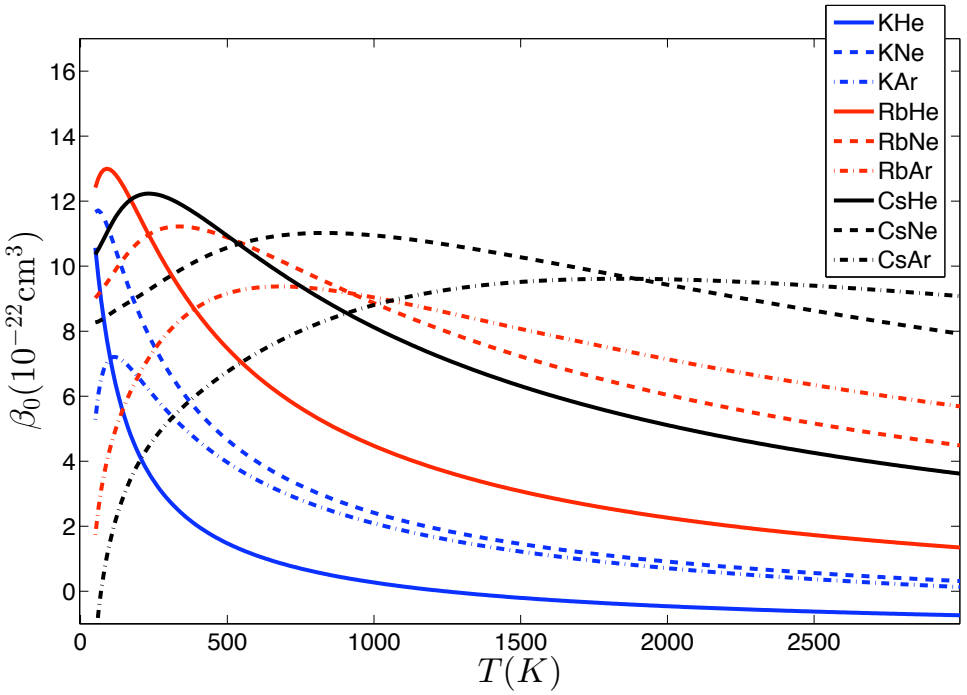

Figure 45. Predicted asymmetry coefficients for the D1 line of all $M+Ng$ combinations.

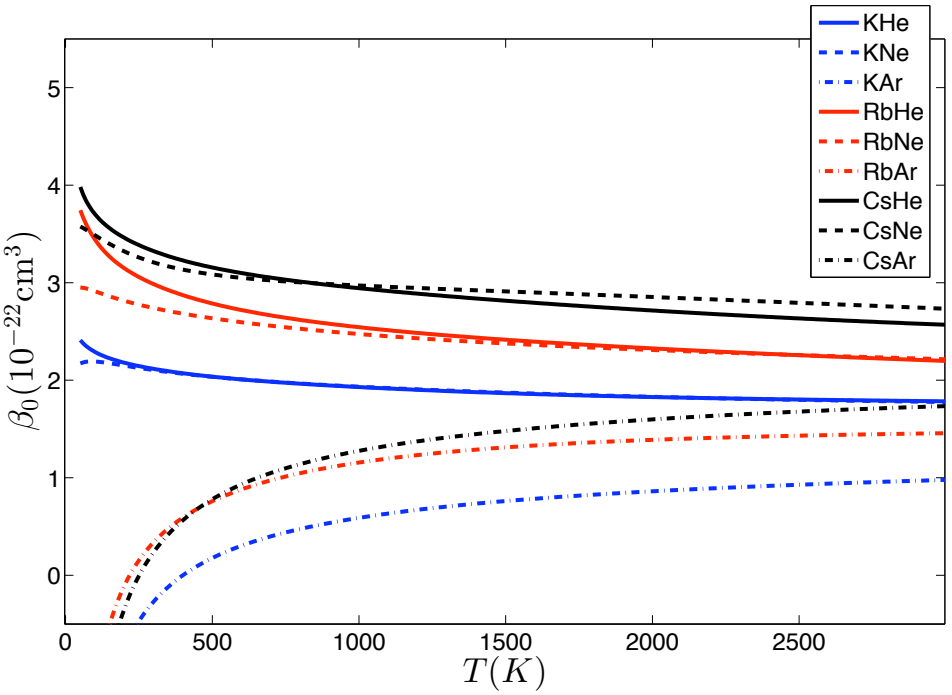

Figure 46. Predicted asymmetry coefficients for the D2 line of all $M+Ng$ combinations.

The temperature dependence of the asymmetry coefficients for the D_1 and D_2 line shapes of all $M + Ng$ combinations is shown in Figures 45 and 46, respectively. As illustrated in Figure 45, the K + Ng, Rb + Ng, and Cs + He D_1 asymmetry coefficients at low temperatures either rapidly rise or start at a peak value and then decay back to zero as the temperature increases with the K + He D_1 becoming slightly negative. The rate of decay correlates strongly with alkali-metal atom where the K + Ng asymmetry coefficients decay most rapidly followed by Rb + Ng and then Cs + Ng. For any given alkali-metal atom the asymmetry coefficients decay the most rapidly for helium, followed by neon, and then argon, with the exception of the K + Ar asymmetry coefficient which decays at nearly the same rate as the K + Ne asymmetry coefficient. The D_2 asymmetry coefficients in shown in Figure 46 exhibit the strongest dependence on temperature at lower values of T. As the temperature increases, all of the D_2 asymmetry coefficients become nearly constant with little dependence on temperature at higher values of T.

5.5 Comparison with other work

Broadening and shifting coefficients calculated using semiclassical AT theory are compared in Table 13 with a variety of experimental observations made at specific temperatures. The AT broadening and shifting coefficients are also compared in Table 13 with broadening and shifting coefficients computed using a fully quantum mechanical calculation [Loper, 2013, Loper and Weeks, in preparation] that employs the Baranger theory of line broadening [Baranger, 1958]. The PECs used for the quantum mechanical Baranger calculations listed in Table 13 are the same as those used for the semiclassical AT calculations. This enables the comparison of semiclassical AT results with fully quantum mechanical Baranger results without the ambiguity introduced by the use of different PECs. The percentage error of the broadening

coefficients computed using Baranger theory relative to the broadening coefficients computed using AT theory is in general larger for the D_1 line than for the D_2 line. The largest errors in the D_1 line are $\approx 30\%$ for K + Ne, Rb + He, Rb + Ne, and Cs + He. The D_2 lines exhibit errors of $\approx 10\%$ or less with the exception of the Rb + Ar D_2 line with and error of $\approx 20\%$. The percentage error of the D_1 and D_2 broadening coefficients computed using AT theory relative to experimental observation are $\approx 15\%$ with the exception of the M + Ar pairs and the K + Ne D_1 line. The K + Ne D_1 line exhibits a relative error of $\approx 30\%$, and all the M + Ar values are very nearly a factor of two too small, most likely because of errors in the long range region of the M + Ar PECs. There is very little agreement in Table 13 between shifting coefficients computed using AT theory, shifting coefficients computed using Baranger theory, and experimental shifting coefficients for both the D_1 and D_2 lines.

A comparison of several different theoretical results for the D_1 and D_2 broadening coefficients of K + He is shown in Figure 47 for a range of temperatures T$= 50 - 3000$K. Included in Figure 47 are broadening coefficients computed using AT theory, broadening coefficients computed using Baranger theory with the same PECs used for the AT calculations [Loper, 2013, Loper and Weeks, in preparation], broadening coefficients computed using Baranger theory with an alternative choice of PECs [Mullamphy et al., 2007], and broadening coefficients computed using the dipole autocorrelation formulation [Allard et al., 2007]. Fairly good agreement is observed for broadening coefficient of the D_2 line given the variety of theoretical models and various PECs used for the calculations. Agreement for the D_1 line remains fairly strong for the broadening coefficients computed using AT theory and the broadening coefficients computed using the dipole autocorrelation formulation [Allard et al., 2007], with the Mullamphy et al. [2007] results predicting a somewhat higher value for the D_1 broadening coefficients at higher temperatures.

Table 13. A comparison of broadening and shifting coefficients computed using semi-classical AT theory to experiment and other theory. The Theory B column gives the results of full quantum mechanical Baranger calculations Loper [2013], Loper and Weeks [in preparation] using the same potentials used for the AT results listed in the Theory AT column. Note that radial derivative coupling is ignored for the D1 coefficients listed in the Theory B column. Temperatures are in Kelvin and the coefficients in $10^{-20} cm^{-1}/cm^{-3}$. Note that for the K + Ng combinations the theory was calculated at $T = 410K$ while the experiment gave a range of $T = 400 - 420K$.

		Theory AT		Theory B		Exp		
M+Ng	Temp	α	β	α	β	α	β	Ref
KHe								
D1	410	0.97	0.58	0.91	-0.15	0.82	0.24	[1]
D2	410	1.29	0.09	1.35	0.01	1.09	0.13	[1]
KNe								
D1	410	0.68	0.37	0.49	-0.11	0.45	-0.22	[1]
D2	410	0.69	0.04	0.73	0.06	0.62	-0.33	[1]
KAr								
D1	410	0.64	0.11	0.52	-0.04	1.30	-1.23	[1]
D2	410	0.61	-0.14	0.68	-0.18	1.05	-0.81	[1]
RbHe								
D1	394	1.47	0.79	1.07	-0.82	1.29	0.64	[2]
D2	394	1.35	0.15	1.45	-0.16	1.36	0.05	[2]
RbNe								
D1	394	0.82	0.22	0.55	-0.24	0.67	-0.12	[2]
D2	394	0.67	0.05	0.71	0.00	0.64	-0.33	[2]
RbAr								
D1	394	0.64	-0.03	0.53	-0.30	1.23	-0.92	[2]
D2	394	0.55	-0.09	0.67	-0.29	1.20	-0.78	[2]
CsHe								
D1	323	1.56	0.49	1.13	0.06	1.35	0.47	[3]
D2	313	1.32	0.14	1.43	0.82	1.11	0.07	[4]
CsNe								
D1	313	0.70	0.16	0.59	0.03	0.59	-0.17	[3]
D2	313	0.64	0.05	0.71	0.37	0.53	-0.28	[4]
CsAr								
D1	313	0.57	-0.08	0.54	0.30	0.99	-0.70	[3]
D2	313	0.51	-0.10	0.50	0.28	0.89	-0.67	[4]

[1] Lwin and McCartan [1978]
[2] Rotondaro and Perram [1997]
[3] Pitz et al. [2009]
[4] Pitz et al. [2010]

Table 14. A comparison of Cs + Ng asymmetry coefficients computed using semiclassical AT theory with experiment Hager et al. [2014] at $T = 323K$. Coefficients have units of $10^{-20}cm^3$.

	CsHe		CsNe		CsAr	
	Theory	Exp	Theory	Exp	Theory	Exp
D1	12.0	6.2	9.8	6.8	5.4	-41
D2	3.3	2.7	3.2	-0.2	0.3	-27

A similar comparison of several different theoretical results for the D_1 and D_2 shifting coefficients of K + He is shown in Figure 48 for a range of temperatures T= 100 − 800K. Included in Figure 48 are shifting coefficients computed using AT theory, shifting coefficients computed using Baranger theory with the same PECs used for the AT calculations [Loper, 2013, Loper and Weeks, in preparation], and shifting coefficients computed using Baranger theory with an alternative choice of PECs [Mullamphy et al., 2007]. Unlike the broadening coefficients shown in Figure 47 there appears to be little agreement between the various calculations, even up to the sign of the shifting coefficient.

The general agreement between broadening coefficients exhibited in Table 13 and Figure 47 and general disagreement between shifting coefficients exhibited in Table 13 and Figure 48 most likely occurs because the broadening coefficients computed using AT theory are fairly insensitive to the PECs while the shifting coefficients computed using AT theory are very sensitive to the details of the long range PECs.

Asymmetry coefficients are compared with experiment in Table 14. With the exception of the Cs + He D_2 asymmetry coefficient there appears to be significant error in the calculated asymmetries as compared with experiment. In the absence of a simplified expression for β_0 analogous to Equations (141) and (142) for the broadening and shifting coefficients, it is difficult ascertain precisely why this is the case. One possibility is that the intercept of the imaginary part of $g(s, v)$ shares the same sensitivity to the long range PECs as exhibited by the slope of the imaginary

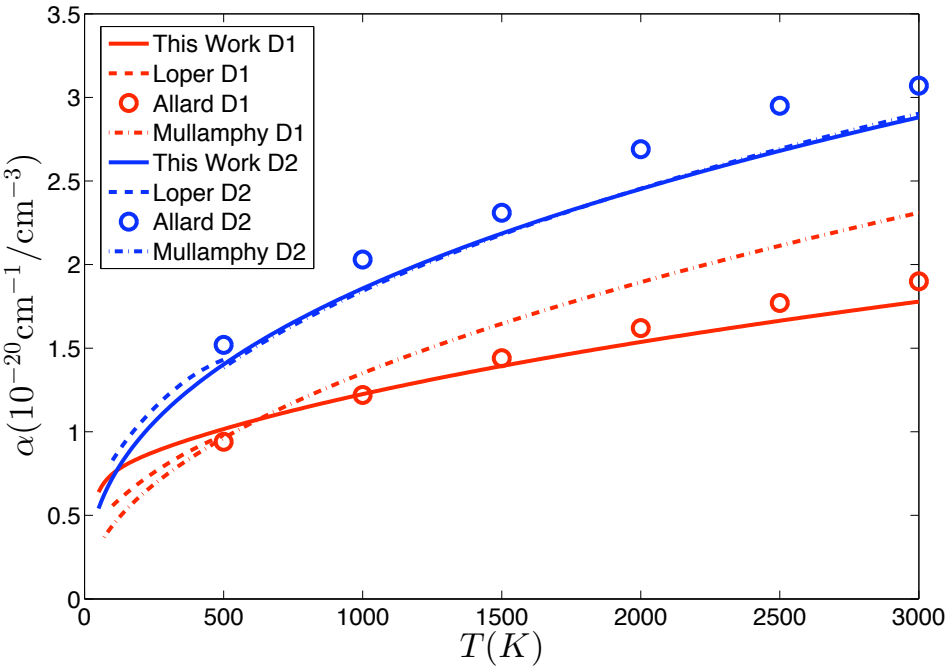

Figure 47. A comparison of broadening coefficients computed using the semiclassical AT theory with other theoretical calculations. Loper Loper [2013] and Loper and Weeks [in preparation] compute broadening coefficients using the quantum mechanical Baranger theory with the same PECs used for the AT calculations. Note that radial derivative coupling is ignored for the Loper D1 coefficients. Allard et al. [2007] compute $\alpha(T)$ using the dipole autocorrelation formulation, and Mullamphy et al. [2007] compute $\alpha(T)$ using quantum mechanical Barringer theory. Both Allard et al. [2007] and Mullamphy et al. [2007] employ different PECs than those used for the AT calculations.

part of $g(s, v)$.

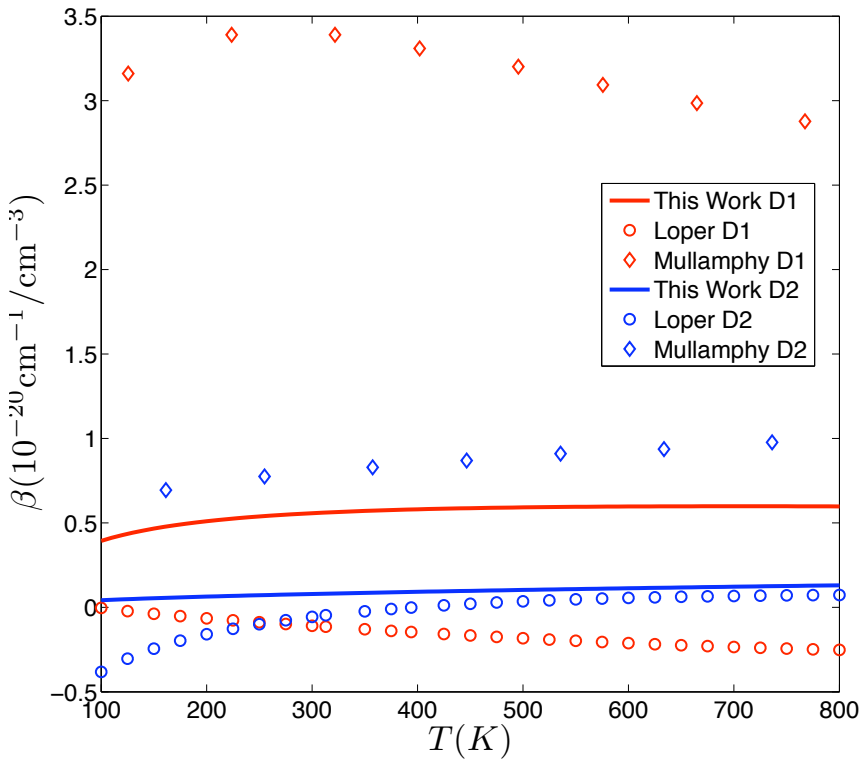

Figure 48. A comparison of Shifting coefficients computed using the semiclassical AT theory with other theoretical calculations. The Loper Loper [2013], Loper and Weeks [in preparation] and Mullamphy et al. [2007] calculations are described in Fig(47).

VI. Conclusions

I calculate ground and excited state PECs for nine different $M + Ng$ pairs. The curves are obtained via a state-averaged multi-configurational self-consistent field calculation followed by a spin-orbit multi-reference singles and doubles configuration interaction calculation. Davidson-Silver corrections are made to the potential energy curves and transition dipole moments are computed. I then use these PECs to compute broadening, shifting, and asymmetry coefficients using the semiclassical AT theory of spectral broadening. The same level of theory is used for all potential energy curve calculations which facilitates the identification of trends that occur as different alkali-metal atoms and noble-gas atoms are considered. These trends are confirmed through a variety of experimental observations including spectroscopic parameters, vibrational energy levels, and collisionally broadened D_1 and D_2 lines. In particular we are able to predict trends in the position of the collisionally induced D_2 satellite peak and, using our calculations together with experimental data, make a prediction for the absolute position of the Rb + He satellite peak.

My potential energy curves for alkali-metal atom and noble-gas atom pairs have been useful for predicting a wide variety of behaviors including non-adiabatic coupling [Belcher, 2011, Lewis, 2011], cross sections for fine structure transitions [Lewis, 2011], and collisionally induced spectral broadening [Loper, 2013]. The curves are used here to compute broadening, shifting and asymmetry coefficients using AT theory. The coefficients are compared with experimental observations at several different temperatures, with coefficients computed using the semiclassical dipole autocorrelation formulation of spectral broadening [Allard et al., 2007], and with two different calculations that use the quantum mechanical Baranger theory of spectral broadening [Mullamphy et al., 2007, Loper, 2013, Loper and Weeks, in preparation]. In general there is reasonable agreement on the broadening coefficients and very little

agreement on the shifting coefficients between the various theoretical calculations and experiment.

I observe that for some systems the difference between coefficients computed using an average over the Maxwell speed distribution and coefficients computed using an average speed can differ on the order of ten percent. I also observe that the broadening coefficients calculated using AT theory may be expressed as the sum of an effective hard sphere contribution and a long range contribution. The effective hard sphere contribution depends on the value of impact parameter for which the accumulated phase has become sufficiently large but is otherwise insensitive to the PECs. The long range contribution to the broadening coefficient depends on the long range form of the PECs with an integrand that decays to zero quadratically with the accumulated phase. The shifting coefficients may also be expressed as the sum of an effective hard sphere contribution and a long range contribution. However, the effective hard sphere contribution to the shifting coefficient is approximately zero. As a result, the shifting coefficient is determined almost entirely by the long range form of the PECs with an integrand that decays linearly to zero with the accumulated phase. This causes the shifting coefficients to be much more sensitive to the details of the long range PECs compared with the broadening coefficients. A small difference in the long range region of the PECs of less than a wave number over $10 - 20$Å can make a significant difference in the value of the shifting coefficient. I attribute the general agreement of broadening coefficients to the similarity of the hard sphere contribution across a variety of different PECs. Because of the long range contribution, the broadening coefficient is still sensitive to the long range form of the PECs. As such general agreement is possible using AT, but getting more than about three significant digits would be a great challenge. I attribute the general disagreement on the shifting coefficients to the much greater sensitivity of $\beta(T)$ to the long range form of the

PECs. This sensitivity of the broadening and shifting coefficient to the long range region of the PECs presents a significant challenge. This challenge is so great that even testing the Anderson-Talman theory's predictions of the line core will be impossible until highly accurate PECs are available.

It is important to note that several different PECs may yield nearly the same broadening and shifting coefficients. For example, the shifting and broadening coefficients computed using the DPs in Figures (30) and (32) at some particular temperature can be used to compute a set of alternative ΔV_{6-12} DPs [Hindmarsh and Farr, 1972, Rotondaro and Perram, 1997]. While agreement on broadening and shifting coefficients between two different sets of potentials may be achieved at a single temperature, they will in general disagree at different temeperatures. As a result, comparison between various theories and experiment should be made over a range of temperatures whenever possible.

Several possible improvements to this work are worth discussing. The largest source of error in these calculations is likely to be basis set incompleteness error, and improvements to the potential energy curves can be made through the consideration of a hierarchy of basis sets, both with and without counterpoise corrections, to explore the complete basis set limit. The counterpoise corrections have the added benefit of ameliorating the basis set superposition error. One could also fit an analytic function to the inner region of the *ab initio* PECs while simultaneously forcing the long range form of the function to be a power series in inverse powers of R, with coeficients determined by theory, as in Roy et al. [2009]. Another possibility is to use Anderson-Talman together with an empirical line shape to start with an *ab initio* PEC and then iteratively reverse engineer a difference potential which reproduces the line shape. This 'Anderson-Talman' difference potential could then be used to calculate other chemical properties to test its validity. Finally, a study of the line wing is possible,

and the inclusion of a time-dependent dipole transition moment in the line shape theory can improve the results [Allard et al., 1999].

Bibliography

Y. Ralchenko, A. E. Kramida, J. Reader, and NIST ASD Team, NIST Atomic Spectral Database (ver. 4.1.0), (http://physics.nist.gov/asd3) National Institute of Standards and Technology, Gaithersburg, MD (2011).

N. Allard and J. Kielkopf. The effect of neutral nonresonant collisions on atomic spectral lines. *Rev. Mod. Phys.*, 54:1103, 1982.

N. F. Allard. Alkali-rare-gas line profiles in a square-well potential approximation. I. satellites. *J. Phys. B: Atom. Molec. Phys.*, 11:1383, 1978.

N. F. Allard and F. Speigelman. Collisional line profiles of rubidium and cesium perturbed by helium and molecular hydrogen. *Astron. Astrophys.*, 452:351, 2006.

N. F. Allard, D. Koester, N. Feautrier, and A. Spielfiedel. Free-free quasi-molecular absorption and satellites in lyman-alpha due to collisions with H and H^+. *Astron. Astrophys. Suppl. Ser.*, 108:417–431, 1994.

N. F. Allard, A. Royer, J. F. Kielkopf, and N. Feautrier. Effect of the variation of electric-dipole moments on the shape of pressure-broadened atomic spectral lines. *Phys. Rev. A*, 60:1021–1033, 1999.

N. F. Allard, J. F. Kielkopf, and F. Allard. Impact broadening of alkali lines in brown dwarfs. *Eur. Phys. J. D*, 44:507–514, 2007.

P. Anderson. A method of synthesis of the statistical and impact theories of pressure broadening. *Phys. Rev.*, 86:809–809, 1952.

R. M. Balabin. Communications: Intramolecular basis set superposition error as a measure of basis set incompleteness: Can one reach the basis set limit without extrapolation? *J. Chem. Phys.*, 132:211103, 2010.

M. Baranger. General impact theory of pressure broadening. *Phys. Rev.*, 112:855–865, 1958.

R. J. Beach, W. F. Krupke, V. K. Kanz, and S. A. Payne. End-pumped continuous-wave alkali vapor lasers: experiment, model, and power scaling. *J. Opt. Soc. Am. B*, 21:2151, 2004.

W. Behmenburg, A. Makonnen, A. Kaiser, F. Rebentrost, V. Staemmler, M. Jungen, G. Peach, A. Devdariani, S. Tserkovnvi, A. Zagrebin, and E. Czuchaj. Optical transitions in excited alkali + rare-gas collision molecules and related interatomic potentials: Li* + He. *J. Phys. B: At. Mol. Opt. Phys.*, 29:3891–3910, 1996.

Lachlan T. Belcher. *Gradients and non-adiabatic derivative coupling terms for spin-orbit wavefunctions.* PhD thesis, Air Force Institute of Technology, 2011.

L Blank, G. S. Kedziora, and D. E. Weeks. Potential energy surfaces for alkali plus noble gas pairs - a systematic comparison. *Proc. of SPIE*, 7581:75810I1–8, 2010.

L Blank, G. S. Kedziora, and D. E. Weeks. $M + Ng$ potential energy curves including spin-orbit coupling for M = K, Rb, Cs and Ng = He, Ne, Ar. *J. Chem. Phys.*, 136:124315, 2012.

F. Bokelmann and D. Zimmermann. Determination of the kar interaction potential in the $X^2\Sigma$ and $A^2\Pi$ state from laser spectroscopic data. *J. Chem. Phys.*, 104:923, 1996.

S. F. Boys and F. Bernardi. The calculation of small molecular interactions by the differences of separate total energies. some procedures with reduced errors. *Mol. Phys.*, 19:553, 1970.

R. G. Breene. Line shape. *Rev. Mod. Phys.*, 29:94–143, 1957.

R. Bruhl and D. Zimmermann. High-resolution laser spectroscopy of LiAr: Spectroscopic parameters and interaction potentials of the $A^2\Pi$ and the $B^2\Sigma$ states. *J. Chem. Phys.*, 114:3035–3045, 2001.

R. Bruhl, J. Kapetanakis, and D. Zimmermann. Determination of the NaKr interaction potential in the $X^2\Sigma$ and $A^2\Pi$ state by laser spectroscopy. *J. Chem. Phys.*, 94:5865–5874, 1991.

U. Buck and H. Pauly. *Zeit. f. Phys.*, 208:390–417, 1968.

A. J. Burgasser, J. D. Kirkpatrick, J. Liebert, and A. Burrows. The spectra of T dwarfs. II. red optical data. *The Astrophysical Journal*, 594:510–524, 2003.

C. Gerald Carrington and Alan Gallagher. Blue satellite bands of Rb broadened by noble gases. *Phys. Rev. A*, 10:1464, 1974.

S. Ch'en and M. Takeo. Broadening and shift of spectral lines due to the presence of foreign gases. *Rev. Mod. Phys.*, 29:20–73, 1957.

Y. L. Chow and C. I. Johansson. Exciplexes of (dibenzoylmethanato)boron/benzenes: The control of exciplex electronic structure. *J. Phys. Chem.*, 99:17558, 1995.

C. Cohen-Tannoudji, B. Diu, and F. Laloe. *Quantum Mechanics*. Hermann and John Wiley and Sons. Inc., 2005.

E. R. Davidson and D. W. Silver. Size consistency in the dilute helium gas electronic structure. *Chem. Phys. Lett.*, 52:403, 1977.

D. L. Drummond and Alan Gallagher. Potentials and continuum spectra of Rbnoble gas molecules. *J. Chem. Phys.*, 60:3426, 1974.

M. Ehara and H. Nakatsuji. Collision induced absorption spectra and line broadening of CsRg system (Rg=Xe, Kr, Ar, Ne) studied by the symmetry adapted clusterconfiguration interaction (SACCl) method. *J. Chem. Phys.*, 102:6822, 1995.

J. Elward-Berry and M. J. Berry. Lithium [Li*(22 P 1/2,3/2)] fine structure transitions induced by collisions with noble gas atoms. *J. Chem. Phys.*, 72:4500, 1980.

K. Enomoto, K. Hirano, M. Kumakura, Y. Takahashi, and T. Yabuzaki. Emission spectra of Cs-He excimers in cold helium gas. *Phys. Rev. A*, 66:042505, 2002.

G. D. Fedorov, S. Koseki, M. W. Schmidt, and M. S. Gordon. Spin-orbit coupling in molecules: Chemistry beyond the adiabatic approximation. *Int. Reviews in Phyiscal Chemistry*, 22:551, 2003.

D. Feller. The role of databases in support of computational chemistry calculations. *J. Comput. Chem.*, 17:1571, 1996.

C. Figl, J. Grosser, O. Hoffmann, and F. Rebentrost. Repulsive KAr potentials from differential optical collisions. *J. Phys. B: At. Mol. Opt. Phys.*, 37:3369, 2004.

E. Goll, H. Werner, H. Stoll, T. Leininger, P. Gori-Giorgi, and A. Savin. A short-range gradient-corrected spin density functional in combination with long-range coupled-cluster methods: Application to alkali-metal rare-gas dimers. *Chem. Phys.*, 329: 276–282, 2006.

G. D. Hager, G. E. Lott, A. J. Archibald, L Blank, D. E. Weeks, and G. P. Perram. High pressure line shapes for Cs D_1 and D_2 lines and empirically informed interaction potentials. *J. Quant. Spectrosc. Radiat. Transfer*, 147:261, 2014.

R. E. M. Hedges, D. L. Drummond, and Alan Gallagher. Extreme-wing line broadening and Cs-inert-gas potentials. *Phys. Rev. A*, 6:1519, 1972.

T. Helgaker, P. Jorgensen, and J. Olsen. *Molecular Electronic-Structure Theory.* Wiley, 2000.

W. R. Hindmarsh and J. M. Farr. Collision broadening of spectral lines by neutral atoms. *Prog. Quantum Electron*, 2:141–214, 1972.

K. Hirano, K. Enomoto, M. Kumakura, Y. Takahashi, and T. Yabuzaki. Emission spectra of Rb*He_n exciplexes in a cold ^{4}He gas. *Phys. Rev. A*, 68:012722, 2003.

S. Ioannis, K. Kerkines, and A. Mavridis. Theoretical investigation of the X $^2\Sigma^+$, A $^2\Pi$, and B $^2\Sigma^+$ states of LiAr and LiKr. *J. Chem. Phys.*, 116:9305, 2002.

S. Iwata. Dispersion energy evaluated by using locally projected occupied and excited molecular orbitals for molecular interaction. *J. Chem. Phys.*, 135:094101, 2011.

P. Knowles, M. Schutz, and H. Werner. *Modern methods and Algorithms of Quantum Chemistry, Proceedings, Second Edition*, 3:97, 2000.

W. Krupke, R. Beach, V. Kanz, and S. Payne. Resonance transition 795-nm rubidium laser. *Optics Letters*, 28:2336, 2003.

C. J. Lee and M. D. Havey. Laser spectroscopy of the 3s $^2\Sigma^+ + \leftarrow$2p $^2\Pi$ transition in LiNe. *Phys. Rev. A*, 43:6066, 1991.

T. Leininger, A. Nicklass, W. Kuechle, H. Stoll, M. Dolg, and A. Bergner. The accuracy of the pseudopotential approximation: non-frozen-core effects for spectroscopic constants of alkali fluorides XF (X = K, Rb, Cs). *Chem. Phys. Lett.*, 255: 274, 1996.

Charlton D. Lewis. *Non-adiabatic atomic transitions: computational cross section calculations of alkali metal - nobel gas collisions*. PhD thesis, Air Force Institute of Technology, 2011.

I. S. Lim, P. Schwerdtfeger, B. Metz, and H. Stoll. All-electron and relativistic pseudopotential studies for the group 1 element polarizabilities from K to element 119. *J. Chem. Phys.*, 122:104103, 2005.

H. Lischka, R. Shepard, F. B. Brown, and I. Shavitt. New implementation of the graphical unitary group approach for multireference direct configuration interaction calculations. *Int. J. Quantum Chem.*, 20:91, 1981.

H. Lischka, R. Shepard, R. M. Pitzer, I. Shavitt, M. Dallow, Th Müller, P. G. Szalay, M. Seth, G. S. Kedziora, S. Yabushita, and Z. Zhang. High-level multireference methods in the quantum-chemistry program system COLUMBUS: Analytic MR-CISD and MR-AQCC gradients and MR-AQCC-LRT for excited states, GUGA spinorbit CI and parallel CI density. *Phys. Chem. Chem. Phys.*, 3:664, 2001.

H. Lischka, R. Shepard, I. Shavitt, R. M. Pitzer, M. Dallos, Th Müller, P. G. Szalay, F. B. Brown, R. Ahlrichs, H. J. Böhm, A. Chang, D. C. Comeau, R. Gdanitz, H. Dachsel, C. Ehrhardt, M. Ernzerhof, P. Höchtl, S. Irle, G. Kedziora, T. Kovar, V. Parasuk, M. J. M. Pepper, P. Scharf, H. Schiffer, M. Schindler, M. Schüler, M. Seth, E. A. Stahlberg, J. G. Zhao, S. Yabushita, Z. Zhang, M. Barbatti, S. Matsika, M. Schuurmann, D. R. Yarkony, S. R. Brozell, E. V. Beck, and J. P. Blaudeau. Columbus, an ab initio electronic structure program, release 5.9.1, 2006.

R. D. Loper and D. E. Weeks. in preparation.

Robert D. Loper. *Collisional broadening and Shift of D_1 and D_2 Spectral Lines in Atomic Alkali Vapor-Noble Gas Systems*. PhD thesis, Air Force Institute of Technology, 2013.

N. Lwin and D. G. McCartan. Collision broadening of the potassium resonance lines by noble gases. *J. Phys. B: Atom. Molec. Phys.*, 11:3841, 1978.

Jeremy M. Merritt, Jiande Han, Terry Chang, and Michael C. Heaven. *Proceedings of the SPIE*, 7196:71960H, 2009.

A. A. Michelson. *The Astrophysical Journal*, 2:251–263, 1885.

F. H. Mies. Molecular theory of atomic collisions: Fine-structure transitions. *Phys. Rev. A*, 7:942, 1973.

M. Mudrich, F. Stienkemeier, G. Droppelmann, P. Claas, and C. P. Schulz. Quantum interference spectroscopy of rubidium-helium exciplexes formed on helium nanodroplets. *Phys. Rev. Lett.*, 100:023401, 2008.

D. F. T. Mullamphy, G. Peach, V. Venturi, I. B. Whittingham, and S. J. Gibson. Collisional broadening of alkali doublets by helium perturbers. *J. Phys. B: At. Mol. Opt. Phys.*, 40:1141–1152, 2007.

M. Nowakowska, M. Smoluch, and P. Petelenz. Mixing of exciton-transfer and charge-transfer contributions to the wavefunction of the naphthalene-hexachlorobiphenyl exciplex. *Chem. Phys. Lett.*, 270:234, 1997.

R. H. Page, R. J. Beach, V. K. Kanz, and W. F. Krupke. Multimode-diode-pumped gas (alkali-vapor) laser. *Opt. Lett.*, 31:353, 2006.

J. Pascale. Use of l-dependent pseudopotentials in the study of alkali-metal-atomhe systems. the adiabatic molecular potentials. *Phys. Rev. A*, 28:632, 1983.

J. Pascale and J. Vandeplanque. Excited molecular terms of the alkalirare gas atom pairs. *J. Chem. Phys.*, 60:2278, 1974.

G. A. Pitz, D. E. Wertepny, and G. P. Perram. Pressure broadening and shift of the cesium D_1 transition by the noble gases and N_2, H_2, HD, D_2, CH_4, C_2H_6, CF_4, and ^{3}He. *Phys. Rev. A*, 80:062718, 2009.

G. A. Pitz, C. D. Fox, and G. P. Perram. Pressure broadening and shift of the cesium D_2 transition by the noble gases and N_2, H_2, HD, D_2, CH_4, C2H_6, CF_4, and He_3 with comparison to the D_1 transition. *Phys. Rev. A*, 82:042502, 2010.

J. D. Readle, C. J. Wagner, J. T. Verdeyen, T. M. Spinka, D. L. Carroll, and J. G. Eden. Pumping of atomic alkali lasers by photoexcitation of a resonance line blue satellite and alkali-rare gas excimer dissociation. *Appl. Phys. Lett.*, 94:251112, 2009.

M. B. El Hadj Rhouma, H. Berriche, Z. B. Lakhdar, and F. Spiegelman. Pumping of atomic alkali lasers by photoexcitation of a resonance line blue satellite and alkali-rare gas excimer dissociation. *J. Chem. Phys.*, 116:1839, 2002.

F. Rossi and J. Pascale. Pseudopotential molecular-structure calculations for alkali-metal-atomH_2 systems. *Phys. Rev. A*, 32:2657, 1985.

Rostas. *Alkali-Rare Gas Excimers in Spectral Line Shapes.* Walter de Gruyter, Berlin, 1981.

M. Rotondaro and G. Perram. Collisional broadening and shift of the rubidium D_1 and D_2 lines (5^2S12 5^2P12, 5^2P32) by rare gases, H_2, D_2, N_2, CH_4 and CF_4. *J. Quant. Spectrosc. Radiat. Transfer*, 57:497, 1997.

R. J. Le Roy, N. S. Dattani, J. A. Coxon, A. J. Ross, P. Crozet, and C. Linton. Accurate analytic potentials for $Li_2(X^1\Sigma_g^+)$ and $Li_2(A^1\Sigma_u^+)$ from 2 to 90 angstorm, and the radiative lifetime of Li($2p$). *J. Chem. Phys.*, 131:204309, 2009.

J. H. Sanders. *Progress in Quantum Electronics.* Pergamon Press, New York, 1973.

R. Santra and K. Kirby. Ab initio configuration-interaction investigation of optical transitions in K+He and K+H_2. *J. Chem. Phys.*, 123:214309, 2005.

M. W. Schmidt, K. K. Baldridge, J. A. Boatz, S. T. Elbert, M. S. Gordon, J. H. Jensen, S. Koseki, N. Matsunaga, K. A. Nguyen, S. Su, T. L. Windus, M. Dupuis, and J. A. Montgomery. General atomic and molecular electronic structure system. *J. Comput. Chem.*, 14:1347, 1993.

K. L. Schuchardt, B. T. Didier, T. Elsethagen, L. Sun, V. Gurumoorthi, J. Chase, J. Li, and T. L. Windus. Basis set exchange: a community database for computational sciences. *J. Chem. Inf. Model.*, 47:1045, 2007.

S. Seager and D. D. Sasselov. Theoretical transmission spectra during extrasolar giant planet transits. *ApJ*, 537:916–921, 2000.

R. Shepard, I. Shavitt, R. M. Pitzer, D. C. Comeau, M. Pepper, H. Lischka, P. G. Szalay, R. Ahlrichs, F. B. Brown, and J. Zhao. *Int. J. Quantum Chem., Quantum Chem. Symp.*, 22:149, 1988.

S. Shirai, S. Iwata, T. Tani, and S. Inagaki. Ab initio studies of aromatic excimers using multiconfiguration quasi-degenerate perturbation theory. *J. Phys. Chem. A*, 115:7687, 2011.

A. J. Stone. *The Theory of Intermolecular Forces.* Clarendon Press, Oxford, 1996.

A. Szabo and S. Ostlund. *Modern Quantum Chemistry.* Macmillan Publishing Co., Inc., 1989.

J. Szudy and W. Baylis. Unified Franck-Condon treatment of pressure broadening of spectral lines. *J. Quant. Spectrosc. Radiat. Transf.*, 15:641, 1975.

J. Szudy and W. Baylis. Profiles of line wings and rainbow satellites associated with optical and radiative collisions. *Phys. Rep.*, 266:127, 1996.

G. Theodorakopoulos and I. D. Petsalakis. Potential energy curves and radiative lifetimes of rydberg states of NaHe. *J. Phys. B: At. Mol. Opt. Phys.*, 26:4367–4380, 1993.

C. Van Trigt. On the theory of pressure broadening. *Physica*, 32:571–575, 1966.

F. Weigend and R. Ahlrichs. Balanced basis sets of split valence, triple zeta valence and quadruple zeta valence quality for H to Rn: Design and assessment of accuracy. *Phys. Chem. Chem. Phys.*, 7:3297, 2005.

S. Yabushita, Z. Zhang, and R. M. Pitzer. Spinorbit configuration interaction using the graphical unitary group approach and relativistic core potential and spinorbit operators. *J. Phys. Chem. A*, 103:5791, 1999.

M. Zbiri and C. Daul. Investigating the M*He exciplexes, M=Li,Na,K,Rb,Cs,Fr: Density functional approach. *J. Chem. Phys.*, 121:11625, 2004.

B. V. Zhdanov, T. Ehrenreich, and R. J. Knize. Highly efficient optically pumped cesium vapor laser. *Opt. Commun.*, 260:696, 2006.

B. V. Zhdanov, J. Sell, and R. J. Knize. Cs 894.3nm laser pumped by photoassociation of CsKr pairs: excitation of the Cs D_2 blue and red satellites. *Electron. Lett.*, 44: 582, 2008.

C. Zhu, J. F. Babb, and A. Dalgarno. Theoretical study of pressure broadening of lithium resonance lines by helium atoms. *Phys. Rev. A*, 71:052710, 2005.

C. Zhu, J. F. Babb, and A. Dalgarno. Theoretical study of sodium and potassium resonance lines pressure broadened by helium atoms. *Phys. Rev. A*, 73:012506, 2006.

REPORT DOCUMENTATION PAGE

Form Approved
OMB No. 0704–0188

1. REPORT DATE (DD–MM–YYYY)	2. REPORT TYPE	3. DATES COVERED *(From — To)*
12-09-2014	Doctoral Dissertation	October 2006 – August 2014

4. TITLE AND SUBTITLE
Potential Energy Curves and Associated Line Shape of Alkali-Metal and Noble-Gas Interactions

5a. CONTRACT NUMBER

5b. GRANT NUMBER

5c. PROGRAM ELEMENT NUMBER

6. AUTHOR(S)
Larry Aaron Blank

5d. PROJECT NUMBER

5e. TASK NUMBER

5f. WORK UNIT NUMBER

7. PERFORMING ORGANIZATION NAME(S) AND ADDRESS(ES)
Air Force Institute of Technology
Graduate School of Engineering and Management (AFIT/EN)
2950 Hobson Way
WPAFB, OH 45433-7765

8. PERFORMING ORGANIZATION REPORT NUMBER
AFIT-ENP-DS-14-D-51

9. SPONSORING / MONITORING AGENCY NAME(S) AND ADDRESS(ES)
Harro Ackerman, High-Energy Laser Joint Technology Office
801 University Blvd SE
Ste 209
Albuquerque, NM 87106
505-248-8208, Harro.Ackerman@jto.hpc.mil

10. SPONSOR/MONITOR'S ACRONYM(S)
HEL JTO

11. SPONSOR/MONITOR'S REPORT NUMBER(S)

12. DISTRIBUTION / AVAILABILITY STATEMENT
DISTRIBUTION STATEMENT A: APPROVED FOR PUBLIC RELEASE; DISTRIBUTION UNLIMITED

13. SUPPLEMENTARY NOTES This work is declared as a work of the U.S. Government and is not subject to copyright protection in the United States.

14. ABSTRACT Recent interest in optically-pumped alkali laser systems has prompted this study into the binary interaction potentials between species of alkali-metal and rare-gas atoms and the effects of the collision of these species on the alkali-metal atom absorption spectrum. Special attention is placed on the relationship of the interaction potentials and the resulting line shape. Potential energy curves and associated dipole matrix elements are computed for M + Ng at the spin-orbit multi-reference configuration interaction level, where M = K, Rb, Cs and Ng = He, Ne, Ar. Dissociation energies and equilibrium positions for all minima are identified and corresponding vibrational energy levels are computed. Difference potentials are used together with the quasistatic approximation to estimate the position of satellite peaks of collisionally broadened D2 lines. The comparison of potential energy curves for different alkali-metal atom and noble-gas atom combinations is facilitated by using the same level of theory for all nine M + Ng pairs. The Anderson-Talman theory of spectral line broadening is used together with potential energy curves calculated at the spin-orbit multi-reference configuration interaction level to compute broadening, shifting, and asymmetry coefficients of the D1 and D2 lines. The calculated coefficients are compared to experiment for a variety of temperatures. In all cases general agreement is observed for the broadening coefficients, while significant disagreement is observed for the shifting coefficients. I also compare my K + He broadening and shifting results with fully quantum mechanical calculations that employ the Baranger theory of collisional line broadening, and then compare the results with other semiclassical calculations. As with the comparison to experiment, closer agreement is observed for the broadening coefficients while the shifting coefficients exhibit significant disagreement. I use the natural variation between the difference potentials of the nine M + N g pairs to explore the relationship between potential and line shape as determined by Anderson-Talman theory and develop a picture for the mechanism that underlies the general agreement between theoretical and experimental results on the broadening coefficient and the general disagreement on shifting coefficients.

15. SUBJECT TERMS
Alkali Metal – Noble Gas Potential Energy Curves, Collisional Line Broadening, Optically Pumped Alkali Laser

16. SECURITY CLASSIFICATION OF:			17. LIMITATION OF ABSTRACT	18. NUMBER OF PAGES	19a. NAME OF RESPONSIBLE PERSON
a. REPORT	b. ABSTRACT	c. THIS PAGE			Dr. David E. Weeks, AFIT/ENP
U	U	U	UU	177	19b. TELEPHONE NUMBER (Include Area Code) (937) 255-3636 x4561 David.Weeks@afit.edu